Application of Remote Sensing Techniques for the Seismo-tectonic Study of Nahanni Earthquake Area

by

Bo Li

This Thesis is Submitted to the Faculty of Graduate Studies in Partial Fullfillment of the Requirements for a Degree of

MASTER OF SCIENCE
in Geophysics

Geophysics, Department of Geological Sciences
University of Manitoba, Winnipeg, Manitoba
August, 1993

National Library
of Canada

Acquisitions and
Bibliographic Services Branch

395 Wellington Street
Ottawa, Ontario
K1A 0N4

Bibliothèque nationale
du Canada

Direction des acquisitions et
des services bibliographiques

395, rue Wellington
Ottawa (Ontario)
K1A 0N4

Your file *Votre référence*

Our file *Notre référence*

The author has granted an irrevocable non-exclusive licence allowing the National Library of Canada to reproduce, loan, distribute or sell copies of his/her thesis by any means and in any form or format, making this thesis available to interested persons.

L'auteur a accordé une licence irrévocable et non exclusive permettant à la Bibliothèque nationale du Canada de reproduire, prêter, distribuer ou vendre des copies de sa thèse de quelque manière et sous quelque forme que ce soit pour mettre des exemplaires de cette thèse à la disposition des personnes intéressées.

The author retains ownership of the copyright in his/her thesis. Neither the thesis nor substantial extracts from it may be printed or otherwise reproduced without his/her permission.

L'auteur conserve la propriété du droit d'auteur qui protège sa thèse. Ni la thèse ni des extraits substantiels de celle-ci ne doivent être imprimés ou autrement reproduits sans son autorisation.

ISBN 0-315-85942-3

Canada

Name _____

Dissertation Abstracts International is arranged by broad, general subject categories. Please select the one subject which most nearly describes the content of your dissertation. Enter the corresponding four-digit code in the spaces provided.

Geophysics
SUBJECT TERM

0373
SUBJECT CODE

U·M·I

Subject Categories

THE HUMANITIES AND SOCIAL SCIENCES

COMMUNICATIONS AND THE ARTS
Architecture 0729
Art History 0377
Cinema 0900
Dance 0378
Fine Arts 0357
Information Science 0723
Journalism 0391
Library Science 0399
Mass Communications 0708
Music 0413
Speech Communication 0459
Theater 0465

EDUCATION
General 0515
Administration 0514
Adult and Continuing 0516
Agricultural 0517
Art 0273
Bilingual and Multicultural 0282
Business 0688
Community College 0275
Curriculum and Instruction 0727
Early Childhood 0518
Elementary 0524
Finance 0277
Guidance and Counseling 0519
Health 0680
Higher 0745
History of 0520
Home Economics 0278
Industrial 0521
Language and Literature 0279
Mathematics 0280
Music 0522
Philosophy of 0998
Physical 0523
Psychology 0525
Reading 0535
Religious 0527
Sciences 0714
Secondary 0533
Social Sciences 0534
Sociology of 0340
Special 0529
Teacher Training 0530
Technology 0710
Tests and Measurements 0288
Vocational 0747

LANGUAGE, LITERATURE AND LINGUISTICS
Language
- General 0679
- Ancient 0289
- Linguistics 0290
- Modern 0291

Literature
- General 0401
- Classical 0294
- Comparative 0295
- Medieval 0297
- Modern 0298
- African 0316
- American 0591
- Asian 0305
- Canadian (English) 0352
- Canadian (French) 0355
- English 0593
- Germanic 0311
- Latin American 0312
- Middle Eastern 0315
- Romance 0313
- Slavic and East European 0314

PHILOSOPHY, RELIGION AND THEOLOGY
Philosophy 0422
Religion
- General 0318
- Biblical Studies 0321
- Clergy 0319
- History of 0320
- Philosophy of 0322

Theology 0469

SOCIAL SCIENCES
American Studies 0323
Anthropology
- Archaeology 0324
- Cultural 0326
- Physical 0327

Business Administration
- General 0310
- Accounting 0272
- Banking 0770
- Management 0454
- Marketing 0338

Canadian Studies 0385
Economics
- General 0501
- Agricultural 0503
- Commerce-Business 0505
- Finance 0508
- History 0509
- Labor 0510
- Theory 0511

Folklore 0358
Geography 0366
Gerontology 0351
History
- General 0578
- Ancient 0579
- Medieval 0581
- Modern 0582
- Black 0328
- African 0331
- Asia, Australia and Oceania 0332
- Canadian 0334
- European 0335
- Latin American 0336
- Middle Eastern 0333
- United States 0337

History of Science 0585
Law 0398
Political Science
- General 0615
- International Law and Relations 0616
- Public Administration 0617

Recreation 0814
Social Work 0452
Sociology
- General 0626
- Criminology and Penology ... 0627
- Demography 0938
- Ethnic and Racial Studies 0631
- Individual and Family Studies 0628
- Industrial and Labor Relations 0629
- Public and Social Welfare 0630
- Social Structure and Development 0700
- Theory and Methods 0344

Transportation 0709
Urban and Regional Planning 0999
Women's Studies 0453

THE SCIENCES AND ENGINEERING

BIOLOGICAL SCIENCES
Agriculture
- General 0473
- Agronomy 0285
- Animal Culture and Nutrition 0475
- Animal Pathology 0476
- Food Science and Technology 0359
- Forestry and Wildlife 0478
- Plant Culture 0479
- Plant Pathology 0480
- Plant Physiology 0817
- Range Management 0777
- Wood Technology 0746

Biology
- General 0306
- Anatomy 0287
- Biostatistics 0308
- Botany 0309
- Cell 0379
- Ecology 0329
- Entomology 0353
- Genetics 0369
- Limnology 0793
- Microbiology 0410
- Molecular 0307
- Neuroscience 0317
- Oceanography 0416
- Physiology 0433
- Radiation 0821
- Veterinary Science 0778
- Zoology 0472

Biophysics
- General 0786
- Medical 0760

EARTH SCIENCES
Biogeochemistry 0425
Geochemistry 0996
Geodesy 0370
Geology 0372
Geophysics 0373
Hydrology 0388
Mineralogy 0411
Paleobotany 0345
Paleoecology 0426
Paleontology 0418
Paleozoology 0985
Palynology 0427
Physical Geography 0368
Physical Oceanography 0415

HEALTH AND ENVIRONMENTAL SCIENCES
Environmental Sciences 0768
Health Sciences
- General 0566
- Audiology 0300
- Chemotherapy 0992
- Dentistry 0567
- Education 0350
- Hospital Management 0769
- Human Development 0758
- Immunology 0982
- Medicine and Surgery 0564
- Mental Health 0347
- Nursing 0569
- Nutrition 0570
- Obstetrics and Gynecology .. 0380
- Occupational Health and Therapy 0354
- Ophthalmology 0381
- Pathology 0571
- Pharmacology 0419
- Pharmacy 0572
- Physical Therapy 0382
- Public Health 0573
- Radiology 0574
- Recreation 0575
- Speech Pathology 0460
- Toxicology 0383

Home Economics 0386

PHYSICAL SCIENCES
Pure Sciences
Chemistry
- General 0485
- Agricultural 0749
- Analytical 0486
- Biochemistry 0487
- Inorganic 0488
- Nuclear 0738
- Organic 0490
- Pharmaceutical 0491
- Physical 0494
- Polymer 0495
- Radiation 0754

Mathematics 0405
Physics
- General 0605
- Acoustics 0986
- Astronomy and Astrophysics 0606
- Atmospheric Science 0608
- Atomic 0748
- Electronics and Electricity 0607
- Elementary Particles and High Energy 0798
- Fluid and Plasma 0759
- Molecular 0609
- Nuclear 0610
- Optics 0752
- Radiation 0756
- Solid State 0611

Statistics 0463

Applied Sciences
Applied Mechanics 0346
Computer Science 0984
Engineering
- General 0537
- Aerospace 0538
- Agricultural 0539
- Automotive 0540
- Biomedical 0541
- Chemical 0542
- Civil 0543
- Electronics and Electrical 0544
- Heat and Thermodynamics ... 0348
- Hydraulic 0545
- Industrial 0546
- Marine 0547
- Materials Science 0794
- Mechanical 0548
- Metallurgy 0743
- Mining 0551
- Nuclear 0552
- Packaging 0549
- Petroleum 0765
- Sanitary and Municipal 0554
- System Science 0790

Geotechnology 0428
Operations Research 0796
Plastics Technology 0795
Textile Technology 0994

PSYCHOLOGY
General 0621
Behavioral 0384
Clinical 0622
Developmental 0620
Experimental 0623
Industrial 0624
Personality 0625
Physiological 0989
Psychobiology 0349
Psychometrics 0632
Social 0451

Nom _____

Dissertation Abstracts International est organisé en catégories de sujets. Veuillez s.v.p. choisir le sujet qui décrit le mieux votre thèse et inscrivez le code numérique approprié dans l'espace réservé ci-dessous.

SUJET

CODE DE SUJET

U·M·I

Catégories par sujets

HUMANITÉS ET SCIENCES SOCIALES

COMMUNICATIONS ET LES ARTS

Architecture 0729
Beaux-arts 0357
Bibliothéconomie 0399
Cinéma 0900
Communication verbale 0459
Communications 0708
Danse 0378
Histoire de l'art 0377
Journalisme 0391
Musique 0413
Sciences de l'information 0723
Théâtre 0465

ÉDUCATION

Généralités 515
Administration 0514
Art 0273
Collèges communautaires 0275
Commerce 0688
Économie domestique 0278
Éducation permanente 0516
Éducation préscolaire 0518
Éducation sanitaire 0680
Enseignement agricole 0517
Enseignement bilingue et multiculturel 0282
Enseignement industriel 0521
Enseignement primaire. 0524
Enseignement professionnel 0747
Enseignement religieux 0527
Enseignement secondaire 0533
Enseignement spécial 0529
Enseignement supérieur 0745
Évaluation 0288
Finances 0277
Formation des enseignants 0530
Histoire de l'éducation 0520
Langues et littérature 0279
Lecture 0535
Mathématiques 0280
Musique 0522
Orientation et consultation 0519
Philosophie de l'éducation 0998
Physique 0523
Programmes d'études et enseignement 0727
Psychologie 0525
Sciences 0714
Sciences sociales 0534
Sociologie de l'éducation 0340
Technologie 0710

LANGUE, LITTÉRATURE ET LINGUISTIQUE

Langues
- Généralités 0679
- Anciennes 0289
- Linguistique 0290
- Modernes 0291

Littérature
- Généralités 0401
- Anciennes 0294
- Comparée 0295
- Médiévale 0297
- Moderne 0298
- Africaine 0316
- Américaine 0591
- Anglaise 0593
- Asiatique 0305
- Canadienne (Anglaise) 0352
- Canadienne (Française) 0355
- Germanique 0311
- Latino-américaine 0312
- Moyen-orientale 0315
- Romane 0313
- Slave et est-européenne 0314

PHILOSOPHIE, RELIGION ET THÉOLOGIE

Philosophie 0422
Religion
- Généralités 0318
- Clergé 0319
- Études bibliques 0321
- Histoire des religions 0320
- Philosophie de la religion 0322

Théologie 0469

SCIENCES SOCIALES

Anthropologie
- Archéologie 0324
- Culturelle 0326
- Physique 0327

Droit 0398
Économie
- Généralités 0501
- Commerce-Affaires 0505
- Économie agricole 0503
- Économie du travail 0510
- Finances 0508
- Histoire 0509
- Théorie 0511

Études américaines 0323
Études canadiennes 0385
Études féministes 0453
Folklore 0358
Géographie 0366
Gérontologie 0351
Gestion des affaires
- Généralités 0310
- Administration 0454
- Banques 0770
- Comptabilité 0272
- Marketing 0338

Histoire
- Histoire générale 0578
- Ancienne 0579
- Médiévale 0581
- Moderne 0582
- Histoire des noirs 0328
- Africaine 0331
- Canadienne 0334
- États-Unis 0337
- Européenne 0335
- Moyen-orientale 0333
- Latino-américaine 0336
- Asie, Australie et Océanie 0332

Histoire des sciences 0585
Loisirs 0814
Planification urbaine et régionale 0999
Science politique
- Généralités 0615
- Administration publique 0617
- Droit et relations internationales 0616

Sociologie
- Généralités 0626
- Aide et bien-àtre social 0630
- Criminologie et établissements pénitentiaires 0627
- Démographie 0938
- Études de l' individu et de la famille 0628
- Études des relations interethniques et des relations raciales 0631
- Structure et développement social 0700
- Théorie et méthodes. 0344
- Travail et relations industrielles 0629

Transports 0709
Travail social 0452

SCIENCES ET INGÉNIERIE

SCIENCES BIOLOGIQUES

Agriculture
- Généralités 0473
- Agronomie. 0285
- Alimentation et technologie alimentaire 0359
- Culture 0479
- Élevage et alimentation 0475
- Exploitation des pâturages 0777
- Pathologie animale 0476
- Pathologie végétale 0480
- Physiologie végétale 0817
- Sylviculture et faune 0478
- Technologie du bois 0746

Biologie
- Généralités 0306
- Anatomie 0287
- Biologie (Statistiques) 0308
- Biologie moléculaire 0307
- Botanique 0309
- Cellule 0379
- Écologie 0329
- Entomologie 0353
- Génétique 0369
- Limnologie 0793
- Microbiologie 0410
- Neurologie 0317
- Océanographie 0416
- Physiologie 0433
- Radiation 0821
- Science vétérinaire 0778
- Zoologie 0472

Biophysique
- Généralités 0786
- Medicale 0760

SCIENCES DE LA TERRE

Biogéochimie 0425
Géochimie 0996
Géodésie 0370
Géographie physique 0368
Géologie 0372
Géophysique 0373
Hydrologie 0388
Minéralogie 0411
Océanographie physique 0415
Paléobotanique 0345
Paléoécologie 0426
Paléontologie 0418
Paléozoologie 0985
Palynologie 0427

SCIENCES DE LA SANTÉ ET DE L'ENVIRONNEMENT

Économie domestique 0386
Sciences de l'environnement 0768
Sciences de la santé
- Généralités 0566
- Administration des hôpitaux 0769
- Alimentation et nutrition 0570
- Audiologie 0300
- Chimiothérapie 0992
- Dentisterie 0567
- Développement humain 0758
- Enseignement 0350
- Immunologie 0982
- Loisirs 0575
- Médecine du travail et thérapie 0354
- Médecine et chirurgie 0564
- Obstétrique et gynécologie 0380
- Ophtalmologie 0381
- Orthophonie 0460
- Pathologie 0571
- Pharmacie 0572
- Pharmacologie 0419
- Physiothérapie 0382
- Radiologie 0574
- Santé mentale 0347
- Santé publique 0573
- Soins infirmiers 0569
- Toxicologie 0383

SCIENCES PHYSIQUES

Sciences Pures

Chimie
- Généralités 0485
- Biochimie 487
- Chimie agricole 0749
- Chimie analytique 0486
- Chimie minérale 0488
- Chimie nucléaire 0738
- Chimie organique 0490
- Chimie pharmaceutique 0491
- Physique 0494
- PolymÇres 0495
- Radiation 0754

Mathématiques 0405
Physique
- Généralités 0605
- Acoustique 0986
- Astronomie et astrophysique 0606
- Électronique et électricité 0607
- Fluides et plasma 0759
- Météorologie 0608
- Optique 0752
- Particules (Physique nucléaire) 0798
- Physique atomique 0748
- Physique de l'état solide 0611
- Physique moléculaire 0609
- Physique nucléaire 0610
- Radiation 0756

Statistiques 0463

Sciences Appliqués Et Technologie

Informatique 0984
Ingénierie
- Généralités 0537
- Agricole 0539
- Automobile 0540
- Biomédicale 0541
- Chaleur et ther modynamique 0348
- Conditionnement (Emballage) 0549
- Génie aérospatial 0538
- Génie chimique 0542
- Génie civil 0543
- Génie électronique et électrique 0544
- Génie industriel 0546
- Génie mécanique 0548
- Génie nucléaire 0552
- Ingénierie des systèmes 0790
- Mécanique navale 0547
- Métallurgie 0743
- Science des matériaux 0794
- Technique du pétrole 0765
- Technique minière 0551
- Techniques sanitaires et municipales 0554
- Technologie hydraulique 0545

Mécanique appliquée 0346
Géotechnologie 0428
Matières plastiques (Technologie) 0795
Recherche opérationnelle 0796
Textiles et tissus (Technologie) 0794

PSYCHOLOGIE

Généralités 0621
Personnalité 0625
Psychobiologie 0349
Psychologie clinique 0622
Psychologie du comportement 0384
Psychologie du développement 0620
Psychologie expérimentale 0623
Psychologie industrielle 0624
Psychologie physiologique 0989
Psychologie sociale 0451
Psychométrie 0632

APPLICATION OF REMOTE SENSING TECHNIQUES FOR THE SEISMO-TECTONIC STUDY OF NAHANNI EARTHQUAKE AREA

BY

BO LI

A Thesis submitted to the Faculty of Graduate Studies of the University of Manitoba in partial fulfillment of the requirements of the degree of

MASTER OF SCIENCE

© 1993

Permission has been granted to the LIBRARY OF THE UNIVERSITY OF MANITOBA to lend or sell copies of this thesis, to the NATIONAL LIBRARY OF CANADA to microfilm this thesis and to lend or sell copies of the film, and LIBRARY MICROFILMS to publish an abstract of this thesis.

The author reserves other publication rights, and neither the thesis nor extensive extracts from it may be printed or other-wise reproduced without the author's written permission.

Contents

Abstract vi

Acknowledgements viii

List of Figures ix

List of Tables xviii

List of Symbols xx

List of Acronyms xxii

1 Introduction 1

2 Study of Earthquakes Using Remote Sensing Techniques 8

2.1 Earthquake Mechanism 8

2.2 Remote Sensing in Earthquake Study 10

2.2.1 The Elastic Rebound Theory 10

2.2.2 Remote Sensing for Structural Geological Investigation 12

2.2.3 Remote Sensing in Earthquake Investigation 14

3 Geological Setting and Earthquake Activities in the Nahanni Study Area 18

3.1 Physiography 18

3.2 Regional Geological Setting 20

3.3 Regional Tectonic Structure 22

3.4 Stratigraphy 25

3.5 Earthquake Activities in Nahanni Area 27

3.5.1 Previous Earthquake Activities 27

3.5.2 The Thrust and/or Strike-Slip Faulting Mechanism . . 30

3.5.3 Recent Earthquakes 30

3.5.4 The Quiescent Zones 32

4 Seismic Data Processing and Earthquake Mechanism Analysis 36

4.1 Introduction 36

4.2 Epicenter Data 37

4.3 Seismograms of Major Earthquakes 38

4.3.1 Global Seismographic Data Network 38

4.3.2 GDSN Data Flow 40

4.4 Teleseismic Data Analysis 42

4.4.1 Introduction 43

4.4.2 Radiation Pattern at Foci 44

4.4.3 First Motion Recognition 46

4.5 Construction of the Focal Solution 51

4.6 Discussion of the Source Parameters 54

5 Remote Sensing Data and Corrections **64**

5.1 Introduction 64

5.2 Geological Remote Sensing 65

5.3 Electromagnetic Spectrum and Geology 66

5.4 Remote Sensing Techniques for Mapping Structural Geological Features 68

5.5 Landsat Data 69

5.6 SPOT Data 74

5.7 Synthetic Aperture Radar (SAR) Data 78

5.8 Geometric Correction and Registration of Remote Sensing Data 83

5.8.1 Geometric Distortion of Landsat and SPOT Images . . 84

5.8.2 General Procedure for Geometric Correction 86

5.8.3 Control Point Determination 86

5.8.4 Geometric Distortion Modelling 87

5.8.5 Pixel Value Interpolation 90

5.8.6 Geometric Correction 93

6 Digital Processing of Remote Sensing Image Data 96

6.1 Introduction 96

6.2 Elements of Digital Image Processing 97

6.3 Image Enhancement 99

6.3.1 Statistics of Digital Image Processing 101

6.3.2 Point Operation 104

6.3.3 Local Operation 112

6.3.4 Multiband-image Operation 117

6.4 Automatic Linear Feature Detection and Mapping 124

6.4.1 Definition and Significance of Linear Feature 125

6.4.2 Preprocessing prior to Automatic Linear Feature Detection and Mapping 127

6.4.3 Hough Transform and Its Application in Linear Feature Detection 130

6.4.4 Localized HT and Its Implementation 134

7 Results and Discussion **141**

7.1 General Description 141

7.2 Structural Geological Interpretation 145

7.3 Remote Sensing Image Integration and Automatic Linear Feature Mapping 149

7.4 Discussion 157

8 Conclusion **162**

Appendix **165**

Bibliography **211**

Abstract

There were three major earthquakes, with magnitudes greater than 6, that occurred in 1985 and 1988 in the neighborhood of the south branch of the North Nahanni River, Northwest Territories. In this thesis, a detailed investigation of the local earthquake tectonic activities is carried out using remote sensing images, earthquake data from the Global Seismographic Data Network, and other relevant information.

An integrated data processing approach is applied to the analysis, including the integration of different remote sensing data sets and the correlation of digital images with focal parameters and epicenter data.

Multispectral satellite images from the Landsat MSS and SPOT, and airborne C-Band SAR image are geometrically corrected, and enhanced for linear feature interpretation. The Hough Transform is implemented and tested for the automatic mapping of linear features from remote sensing images. Digital seismograms from GDSN are utilized to obtain focal parameters of the main shocks and aftershocks for the Nahanni earthquakes. The mapped lin-

ear features and focal parameters are correlated then to study the structural geological mechanisms and faulting processes associated with the three main events.

Both the remote sensing images and the earthquake data indicate that the west-dipping thrust faulting is active in the earthquake processes, particularly where it meets the new E-W striking faults. Several linear patterns detected on the C-SAR image and east-west linear features mapped by the Hough Transform provide additional information about the tectonic setting and local geological structures related to the earthquakes in the study area.

In the investigation of earthquakes in Nahanni area, as demonstrated in this thesis, remote sensing and digital data integration techniques provide a very effective research method. The results of the investigation suggest that comprehensive structural geological analysis can be accomplished by identifying surface structural geological features based on various remote sensing data sets. Combination of earthquake seismogram data analysis and remote sensing techniques provides a powerful and robust approach for natural hazard study in remote and logistically difficult areas.

Acknowledgements

I would like to thank my supervisor Dr. W. M. Moon, for proposing the topic of this study, his supervision, and continuous encouragement during the course of this work.

The digital earthquake data analyzed in this study were kindly provided by the Geological Survey of Canada and the U.S. Geological Survey.

The airborne C-SAR data were collected and provided for this study through the Radar Data Development Program (RDDP) of the Canada Center for Remote Sensing.

Special thanks go to my fellow student Ms. X. Miao for her help and suggestions in the earthquake seismic data processing.

List of Figures

1.1 Flowchart outlining the study of Nahanni earthquakes using remote sensing techniques and the digital earthquake seismic data integration method. 7

2.1 Subdisciplines of studying earthquake mechanism. 9

3.1 Location of the study area. 19

3.2 Topography and seismicity of the Nahanni study area. Arrows indicate principal stress directions from oil-well breakouts by Adams (1985). Stippled area is land over 1500 m in elevation. (From Wetmiller et al., 1988) 21

3.3 Geological setting of the Nahanni earthquake area. Patterns representing stratigraphic units are as shown in Figure 3.4. Main physiographic subdivisions, principal faults, and the sites of landslides which were triggered by the earthquakes are indicated. Epicenters of the main shock are shown. (From Wetmiller et al., 1988) 23

3.4 Simplified stratigraphic section for the Nahanni earthquake epicentral area. Age of rock units are given by D for Devonian, O for Ordovician, and S for Silurian; u and m are upper and middle, respectively. (From Wetmiller et al., 1988) 26

3.5 Epicenters of Nahanni earthquakes and seismicity of the northeastern Cordillera. Seismicity data are taken from the Canadian Earthquake Epicenter File maintained by the Geological Survey of Canada. Locations of large earthquakes in 1940 and 1955 are indicated. P-nodal solution shown is from Leblanc and Wetmiller (1974). (From Wetmiller et al., 1988) 29

3.6 Epicenters of Nahanni earthquakes (M 3.0 and greater) from October 5, 1985 to March 11,1986, and from March 12, 1986 to March 25, 1988. The M 5.0 and larger earthquakes are numbered in chronological order up to the M 6.0 earthquake that occurred on March 25, 1988. Numbers 1 and 3 are the October 5 and December 23 main shocks, respectively. (From Horner et al., 1990) 31

3.7 The seismicity in the first 24 hours after the October and December main shocks of 1985. Comparison of aftershock activity in the first 24 hours following each main shock. Event numbers are the same as Figure 3.6. A, B, and C show the relative locations of main shock subevents from Choy and Boatwright (1988). The rectangles approximate the extent of quiescent zone around each of the main shock epicenters. 33

3.8 Comparison of aftershock activity over a 78-day period from day 1 after each main shock. Event numbers are the same as in Figure 3.6. The rectangles are the same as in Figure 3.7. . . . 34

4.1 The GDSN stations comprised of SRO, modified high-gain, long-period ASRO, and DWWSSN data systems. 41

4.2 A schematic data flow path of the GDSN data. 42

4.3 Double-couple point source model; Two pairs of forces. The torques about the z-axis are of equal magnitude and are opposite to each other. 45

4.4 Radiation pattern of P wave from a double-couple source. (From Kasahara, 1981) 46

4.5 Plot of ray paths for turning rays computed using WKBJ algorithm (Earth Model 1066B.) 48

4.6 Spherical coordinate geometry used for calculation of epicentral distance. 49

4.7 First motion picked from a GDSN seismogram. 52

4.8 Schematic diagram of focal solution construction. 53

4.9 The focal solution for Events 1 and 2. (See Table 4.3 for event numbering) 60

4.10 The focal solution for Events 3 and 4. 61

4.11 The focal solution for Event 5. 62

4.12 Section views of hypocenter distribution. A-A′ crosses the regional geological strike (N160°E), B-B′ goes along with the regional geological strike. 63

5.1 The EM spectrum used by remote sensing systems. The upper Figure shows expanded diagrams of the visible and infrared regions and the lower Figure shows the microwave region showing atmospheric windows. (From Sabins, 1987) 67

5.2 Spatial coverage of the data sets over the study area. 70

5.3 Chronological launch and retirement history of the Landsat satellite remote sensing system. (From Jensen, 1986) 71

5.4 Landsat-4 / Landsat-5 satellite platform with associated sensor and telecommunication systems. (From Jensen, 1986) 72

5.5 Bus and payload of the SPOT satellite. 75

5.6 Geometry of an airborne Sideways-Looking Radar (SLAR) and schematic plotting of the return signal. 79

5.7 The airborne SAR scan geometry. 82

5.8 Geometric depiction of error source due to platform attitude. . 85

5.9 The spatial relationship between a distorted image and the reference image. (a). The distorted image. (b). The reference image or the base map. 88

5.10 A bilinear interpolation scheme for geometric correction. . . . 92

5.11 The MSS (Bands 7, 5 and 4) composite image before the geometric correction. 95

6.1 An illustration of row, column, pixel and pixel value of image data. 97

6.2 A schematic diagram of ARIES image processing system. . . . 98

6.3 The histogram of SPOT image of Bands 1, 2 and 3 in the study area. 103

6.4 (a). The histogram of the input image; (b). The transform function of clipping procedure; (c). The histogram of the output image from clipping procedure. 106

6.5 Schematic diagram of piecewise linear scaling. 107

6.6 Graphic depiction of logarithmic transform. 109

6.7 (a). Histogram of the original SPOT Band 1 data; (b). Histogram of the SPOT Band 1 data after the logarithmic transform. 110

6.8 Histogram of the SPOT Band 3 data before (top) and after (bottom) the histogram equalization. 113

6.9 Graphic presentation of Principal Component Analysis: (a). A joint distribution of a 2-band image with mean(μ_1, μ_2); (b). A new coordinate system is created by shifting the origin to(μ_1, μ_2); (c). The shifted axes are orthogonally rotated about (μ_1, μ_2) by η degree so that the variation of data projection on axis PC_1 is maximum while on PC_2 is minimum. 121

6.10 The first two principal components of Landsat MSS image: (a). The first principal component provides the most information in an average sense. There is a high degree of image variations in both mountainous and plain regions. Note that too many detailed small scale features make the significant ones not clear in the mountainous region. The "averaging effect" gives the image a fuzzy appearance. (b). The second principal component shows a more clear picture for the main geological structures in the area. Several groups of NW and NE trending features can be easily seen in the mountainous region. River channels and ranges are highlighted by high contrast. But the overall variation of the image has been reduced. 123

6.11 Illustration of the Hough Transform process: (a). Point image space (x,y); (b). Parameter space (m,c); (c). Accumulator space corresponding to (b). 132

6.12 The illustration of the modified Hough Transform concept: (a). Defining a straight line using length ρ and orientation θ; (b). A straight line in the parameter space (ρ,θ). 133

7.1 Landsat MSS image: Bands 7, 5 and 4 color composite for the study area. 142

7.2 Color composite of SPOT images: Bands 1,2 and 3 for the study area. The arrow indicates the site of a rock avalanche triggered by the main shock of October, 1985. 144

7.3 PCA (Second component) linear feature image of the Landsat MSS data for the study area. 145

7.4 Interpreted linear features of the Landsat MSS image data in the study area. 147

7.5 CCRS's airborne C-Band SAR image of the study area. 148

7.6 Integrated image of SPOT image (Bands 3 and 1), CCRS's C-SAR airborne data and local earthquake epicenter distribution information for the study area. 150

7.7 Integrated image of computer picked linear features, edges and PCA second component image of the Landsat MSS data for the study area. 152

7.8 Detailed integrated image of computer picked linear features, edges and PCA second component image of the Landsat MSS data of the epicentral area. 154

7.9 Linear features extended from the SPOT image for the epicentral area by using the Hough Transform. 155

7.10 Integrated image of linear features and the Band 1 of the SPOT image data for the epicentral area. 156

List of Tables

2.1 The optimum scales of the remote sensing platforms for geological investigations. 13

4.1 Geographic information of the earthquake epicenter data in the study area. 37

4.2 Seismic Data types recorded at the GDSN and RSTN stations. 40

4.3 The GDSN Network Day Tape Log for the five earthquake events in the study area. 44

4.4 The contents of Network Tape Log (CD-ROM Data) for the GDSN stations. 57

4.5 Lithosphere model of the Earth Model 1066B. 58

4.6 The P wave travel time table computed using the WKBJ algorithm (Chapman, 1978) with Earth Model 1066B. 59

4.7 The fault parameters of focal solution for the main shock Events 1 and 2, and aftershock Events 3,4 and 5 in the study area. . . 62

5.1 Spatial and pixel parameters of Landsat-5 MSS image data. . 73

5.2 Landsat-5 MSS image data acquisition parameters. 73

5.3 The SPOT HRV sensor system characteristics and IFOV. . . 76

5.4 The SPOT image data acquisition parameters. 77

5.5 CCRS's C-Band SAR data acquisition parameters. 82

5.6 The control point coordinates and residuals for geometric correction of the Landsat MSS image data. 94

6.1 Mean, standard deviation and correlation statistics of SPOT image (Bands 1,2 and 3) data used in the Nahanni study area. 102

6.2 Convolution kernels for the first and second gradient detectors. 116

6.3 The variance and covariance matrices for the Landsat MSS image (Bands 7,6,5 and 4) and the SPOT image (Bands 1,2 and 3). 122

6.4 The eigenvalues, eigenvectors and variance contributions of PCA transform for the Landsat MSS image (Bands 7,6,5 and 4) and the SPOT image (Bands 1,2 and 3). 124

List of Symbols

α	Depression angle of SAR imaging system
β	Width of a radar beam in degree
Δ	Epicentral distance in degree
θ_i	Longitude of station i
ϕ_i	Latitude of station i
τ_r	Time interval between each radar signal pulse
$\mathbf{\Sigma}$	Variance and covariance matrix in the principal component analysis
$f(u,v)$	Spatial transform function in geometric correction
$g(u,v)$	Spatial transform function in geometric correction
i	Emergence angle of a teleseismic ray path
E_x	Error of row position in geometric correction
E_y	Error of column position in geometric correction

$G(x,y)_l$	lth band in the processed multiband image array
$I(x,y)_l$	lth band in the original multiband image array
$K(s,t)$	Kernel of a convolution integral
$Prob(I \leq w)$	Probability distribution of a gray level in an image
R_a	Azimuth resolution of a radar imaging system
R_r	Ground-range resolution of a radar imaging system
$\vec{i}$	Unit vector in the row (x) direction
$\vec{j}$	Unit vector in the column (y) direction
$\mathcal{F}(\cdot)$	2-D Fourier transform
$\mathbf{T}$	Transform matrix in the principal component analysis (PCA)
$\mathbf{V}_\mathrm{i}$	Eigenvector in the Principal Component Analysis
$HT(\rho,\theta)$	Hough Transform

List of Acronyms

ASRO	Abbreviated Seismic Research Observatory
CCD	Charge-Coupled-Detector
CCRS	Canadian Center for Remote Sensing
CCT	Computer Compatible Tapes
DWWSSN	Modified World Wide Standardized Seismic Network
EREP	Earth Resources Experiment Package
GDSN	Global Seismographic Data Network
GSC	Geological Survey of Canada
HH	Horizontal-Horizontal polarization mode
HRV	High Resolution Visible optical sensors
IFOV	Instant Field Of View
LPZ	Long Period Vertical component of a seismogram

MSS	Multi-Spectral Scanner
PCA	Principal Component Analysis
RDDP	Radar Data Development Program
RSTN	Regional Seismic Test Network
SAR	Synthetic Aperture Radar
SLAR	Side Look Airborne Radar
SPOT	Systeme Pour l'Observation de la Terre
SRO	Seismic Research Observatories
TDRSS	Tracking and Data Relay Satellite System
USGS	U.S. Geological Survey
UTM	Universal Transverse Mercator Projection
WWSSN	World Wide Standardized Seismic Network

Chapter 1

Introduction

There were three unusually large earthquakes, with magnitudes greater than 6, that occurred in the neighborhood of the south branch of the North Nahanni River, Northwest Territories in 1985 and 1988. The magnitudes of these earthquakes were unprecedented for this area. These main shocks were followed by extensive aftershock sequences. The tectonic block in which these earthquakes occurred forms a part of the Foreland Fold Belt and is believed to be created along the northeastern Cordillera during the Columbia or Laramide Orogeny (Wetmiller et al., 1988).

The epicentral area encompassing the earthquakes is uninhabited and logistically difficult to access. Relatively fewer geological and geophysical studies have been carried out in this area. For this reason, an attempt is made in this thesis to develop a remote sensing technique for extracting tectonic features of the area. The detected tectonic information is then correlated with other

earthquake source parameters obtained from global seismic networks to investigate the characteristics and tectonic mechanisms of the recent earthquake activities in the study area.

Remote sensing technology has been one of the most rapidly developing fields in recent years. The satellite based remote sensing and the digital computer based image analysis systems have together brought the remote sensing discipline into a new age. Now remote sensing has become a widely used tool in various fields of science and engineering disciplines.

Even in the early days of remote sensing, geological interpretation of remotely sensed images was one of the main applications, especially for structural geological studies. In this thesis, the investigation of earthquakes in the Nahanni area, Northwest Territories has been undertaken using remote sensing techniques in combination with earthquake seismic data. The following aspects are emphasized:

- The use of different remote sensing source data,
- Computer aided interpretation of remote sensing data, and
- The combination of remote sensing and earthquake seismic data for regional earthquake and tectonic investigation.

To obtain comprehensive structural geology information for the research

area, remote sensing data sets with different spatial resolutions and spectral characteristics were gathered. With a resolution of 82 $\times$ 57 (m), the Landsat MSS data set covers the whole research area and has provided a good global view of the regional structural geology setting, whereas the SPOT and airborne C-SAR data sets offer higher resolution images covering the epicentral area. In general, C-SAR images present excellent structural geological features. Moreover, multiple band remote sensing images of the Landsat MSS and SPOT provide lithologic information and other surface spectrum attributes which may be related to the local tectonic activities.

Although the advantages of remote sensing technique are obvious, the use of multiple remote sensing data alone is not sufficient to make conclusive tectonic investigations. The combination of remote sensing data with other geophysical data sources is a more effective and promising approach. In this research, non-remotely sensed data sets include the earthquake epicenter data, and seismograms of the major earthquake events from the study area. The focal plane solutions are obtained for selected phases of the seismograms of the major earthquakes. The resulting earthquake parameters are then combined with structural geological features detected from remote sensing images to investigate the possible earthquake mechanisms.

In conventional geological remote sensing research, the most easily identi-

fiable and common structural geological features or tectonic features are linear and circular structures. Extraction of these structural geological features therefore has become an important task for geological remote sensing investigation. Traditionally, linear feature mapping is done visually by an interpreter, and the output map is not ready for integration with other data sets or further digital analysis. Beside the problem of subjectivity, lack of systematization in manual linear feature mapping has been unavoidable. Therefore, another objective of this research is to develop an acceptable computer algorithm to detect and map linear features from remote sensing image data automatically. An algorithm for the Hough Transform is developed and tested for this purpose.

As the application to structural geology is one of the earliest developed fields in geological remote sensing, work already undertaken by other researchers, especially concerning the study of earthquakes using remote sensing techniques, and the basic principles are discussed in Chapter 2.

Earthquakes are closely related to local surface and structural geology. Due to its remote location, most geological information available for the Nahanni area is preliminary and fairly sketchy. In Chapter 3, the description of the general geological setting, structural geology and stratigraphy are provided mostly based on previous other researchers' works. This thesis focuses on earthquakes in the Nahanni area, Northwest Territories, and therefore they

are described using previous earthquakes, main shocks and aftershocks as examples.

In a research project that combines remote sensing and earthquake seismic information, seismic data processing and interpretation of results also play important roles. In Chapter 4, earthquake seismic data from local seismic stations and from the global digital seismic network are described. Analysis of the seismic data and the solution of earthquake focal parameters based on selected seismograms is also discussed. The earthquake source parameters are closely related to geological structures in the study area and can be used as a guide to the linear feature analysis in the remote sensing image processing later on.

The remote sensing data sets, sensors and their characteristics, geometric corrections and registration of images with different spatial resolutions are included and discussed in Chapter 5. In Chapter 6, image processing techniques including image enhancement, linear feature detection and mapping are described. Detailed discussion is given to automatic linear feature mapping from remote sensing images by using the Hough Transform.

In Chapter 7, the final results from both earthquake seismic data analyses and remote sensing image processing are combined for an integrated study

of the earthquakes in the Nahanni area. The conclusion is given in Chapter 8. The computer program source codes especially written for the Hough Transform in this research are included in the Appendix.

Figure 1.1 is a flowchart showing the main components of the study in this thesis.

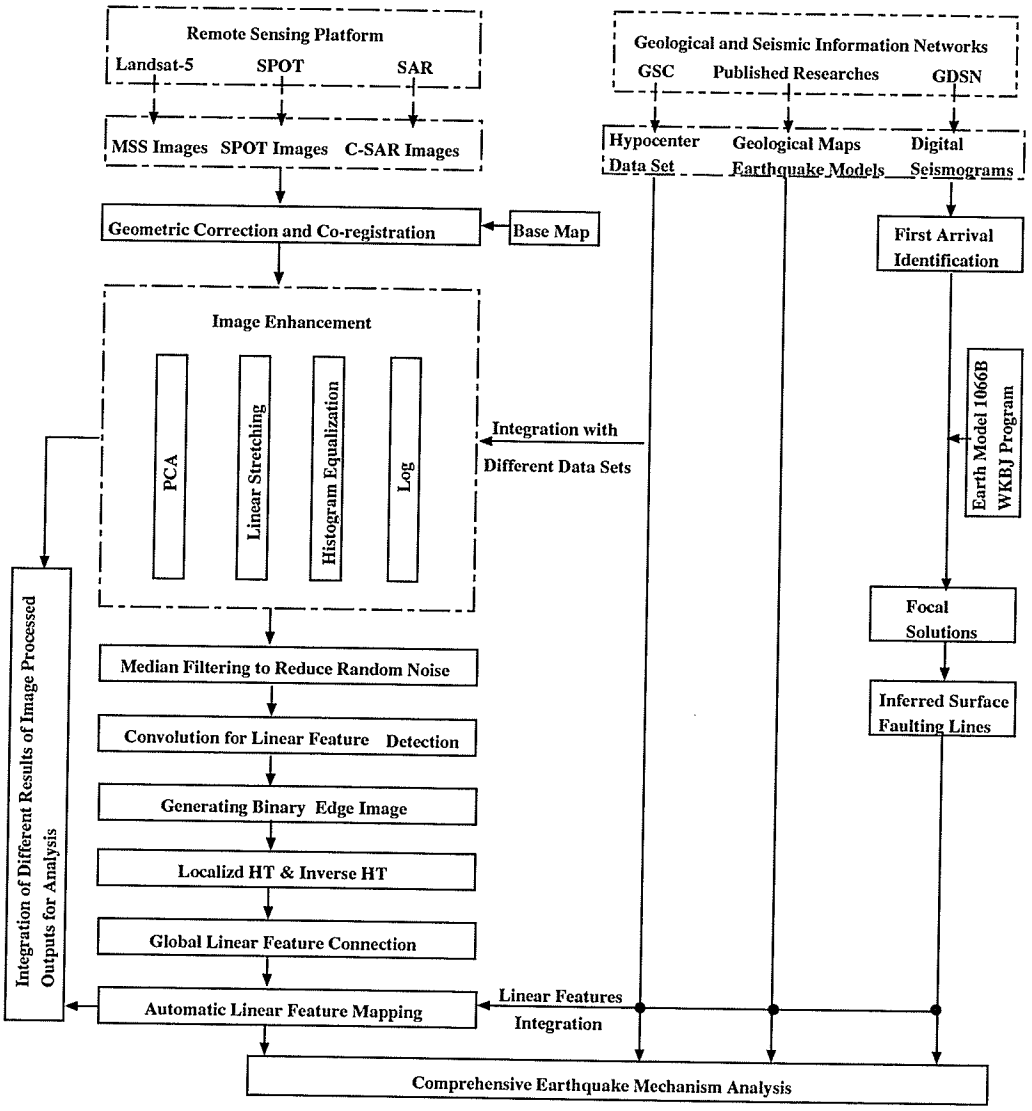

Figure 1.1: Flowchart outlining the study of Nahanni earthquakes using remote sensing techniques and the digital earthquake seismic data integration method.

Chapter 2

Study of Earthquakes Using Remote Sensing Techniques

2.1 Earthquake Mechanism

Earthquakes as one of the most unpredictable and damaging natural disasters today, has historically drawn considerable attention from researchers. The immutable desire to better understand the nature of earthquakes has sustained great advances in earthquake seismology in this century. Figure 2.1 shows the framework of earthquake research in terms of three major fields.

The first concern is the use of seismic waves as probes for exploration of the earth's interior. The third field shown in Figure 2.1 is the application of seismological knowledge to human activities. In this research, the main concern is the second one, the nature of earthquakes , the most fundamental problem

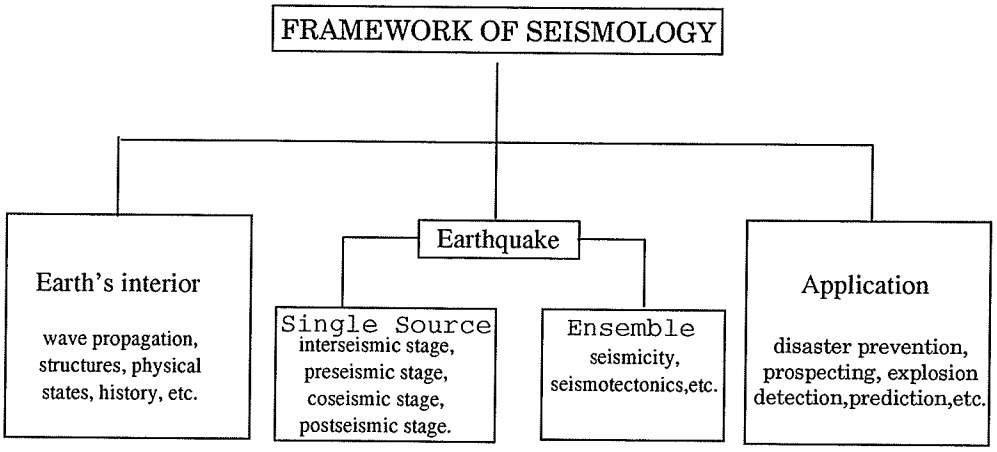

Figure 2.1: Subdisciplines of studying earthquake mechanism.

in earthquake study. This field can be subdivided into two branches. The first branch deals with the general features of an earthquake, i.e. an individual earthquake source is analyzed to give a general and comprehensive picture of an earthquake phenomenon. In the second branch, on the other hand, the activity of earthquakes as a group is major interest. The earthquakes that have been occurring in the study area appear to follow a systematic manner, therefore, the mutual relation between earthquakes, and the dependence of earthquake occurrence on tectonic circumstances are emphasized and investigated.

2.2 Remote Sensing in Earthquake Study

So far remote sensing sensors have little capability of penetrating into the ground surface except that SAR can have a few meters of penetration in certain hyper-arid deserts (McCauley et al., 1982). Use of remote sensing techniques in earthquake study is mainly for investigation of the surface or near surface evidences which may be related to earthquake mechanisms. Earthquakes are in general caused by the abrupt release of strain energy that has built up in the earth's crust. Usually the strain build-up is a very slow process accompanied by various geological phenomena like deformation, folding and fracturing. When earthquakes occur, they often leave significant traces of destruction. In many areas, earthquakes occur repeatedly in a geological time frame. Such historical earthquakes often maintain their records on the surface and provide important information for the future possible events. It is the advantage of remote sensing technique to investigate all these evidences of seismic activity in a large scale and wide range.

2.2.1 The Elastic Rebound Theory

It is convenient to consider the system in which earthquake takes place as a field called an earthquake field (Kasahara, 1981). The earthquake field is

the recipient of energy supplied by a source, and accumulates potential energy until it reaches a critical state.

The elastic rebound theory first proposed by Reid (1911) described the process followed by an earthquake in an earthquake field. This theory has been proved to be valid for most of earthquakes, especially for the shallow ones. The elastic rebound theory states, in layman's terms, that:

1. The fracture of the rock, which causes a tectonic earthquake, is the result of elastic strain, greater than the strength of the rock can withstand, produced by relative displacement of neighboring portions of earth's crust.
2. These relative displacements are not produced suddenly at the time of the fracturing, but attain their maximum gradually during a relatively long period of time.

According to the above theory, today's earthquake activities are the results of the long time process of elastic strain accumulation. The theoretical research and experimental work also show that various structural deformation and geotectonic phenomenon are associated with the accumulating process. By studying earthquakes in California, Allen (1975) summarized the following general relationship between faulting and shallow earthquakes:

- Virtually all large earthquakes (magnitudes greater than 6.0 on the Richter Scale) have resulted from ruptures prior to the events along faults that had been recognized by field geologists.

- All of these faults have a history of earlier displacements in Quaternary and possibly Holocene times.

- All the earthquakes have been shallow, not exceeding about 20 km in depth. Most earthquakes larger than magnitude of 6.0 in California have been accompanied by surface faulting, as have many of the smaller events.

These observations suggest that modern remote sensing techniques offer an excellent opportunity for studying shallow earthquake activities and related faulting processes.

2.2.2 Remote Sensing for Structural Geological Investigation

Many observed geological features related to earthquakes range from several tens of meters to several tens of kilometers in linear dimension. For detection and mapping of surface geological structures with such a scale range, remote sensing techniques offer undoubtly one of the most efficient research tools. Furthermore, currently available remote sensing data sets have not only covered

visible band but also have been extended to spectral band information from near infrared to centimeter wavelengths. In this multiple band environment, even very subtle phenomena caused by surface geological change, for example, variation in vegetation or soil moisture, can be detected. Consequently, many shallow structural geological changes themselves could be revealed.

Table 2.1 gives the optimum scales and corresponding remote sensing platforms for mapping geological deformation and geotectonic phenomena.

Optimum Scales and Corresponding Platforms for Structural Geological and Tectonic Investigation

Structural Scale	Natural Scale & Size of Features	Types of Phenomena	Types of Maps	Platforms & Medium of Observation
Gigascopic	1:50 million >1000 km	Continental or oceanic plates, seismic plates.	Global, world-wide and continental geologic, tectonic and seismic maps.	SAR and other airborne scanning images (visible, IR and radar); Seismic networks (long waves); Landsat and SPOT image (visible and IR)
Megascopic	1:1 million 10 km~1000 km	Mountain belts, basin, island arcs, rift valleys, plutons, megalineaments, craters.	Large global, continental, national, state geologic and tectonic maps.	
Macroscopic	1:1000 10 m~ 10 km	Folds, faults, lineaments, craters, volcanoes, dikes, fractures.	Regional geological and structural maps.	
Mesoscopic	1:1 1 cm~10 m	Folds, faults, cleavages, joints, bedding, geologic contacts.	Detailed geologic and structural maps.	

Table 2.1: The optimum scales of the remote sensing platforms for geological investigations.

The remote sensing data sets available for this research include the Landsat MSS, SPOT and airborne C-SAR data, with which geological structures from

megascopic to mesoscopic level can be mapped.

2.2.3 Remote Sensing in Earthquake Investigation

Although application of remote sensing techniques in geological interpretation has a long history tracing back to the 1920's (Hoppin et al., 1978), research activities on earthquake processes using remote sensing techniques have been less active than other fields. This may be partially due to the fact that more subsurface structural information is needed in this field than other research area, and partially due to limited capability of present remote sensing techniques for subsurface penetration.

Applications of remote sensing techniques in earthquake research had been overwhelmingly dominated by vertical aerial photographs (Williams, 1983). In the past two decades, however, with increasing spatial resolution of satellite based remote sensing systems, various satellite images have become useful for practical geological problems (Glass and Slemmons, 1978). The first color composite image produced from Landsat-1 data was over of the Monterey Bay area, California. The geological structural interpretation was made by Lowman (1976). His result provided a vivid view of the San Andreas Fracture system and a better understanding of tectonic setting associated with seismic activities. Several investigators used Earth Resources Experiment Package (EREP) photographs from Skylab spacecraft to map linear features and to

investigate the relationships between these features and the faults with historical earthquake activities. For example, Olson (1975) pointed out that the most significant finding of his work was detection of the fracture traces and related lineaments crossing the Clark Hill Reservoir on the Savannah River, north of Augusta, Georgia. He noted that epicenters of the earthquakes that occurred in 1974 could be plotted systematically and studied. By using the same image source, Abdel-Gawad and Tubbesing (1975) produced maps delineating specific areas of seismic risks based on geomorphic evidences of recent faulting. Quade and Trexler (1975) mapped lineaments in the Mina region of Nevada and then compared the map with a plot of earthquake epicenters for the period between 1971 and 1973. They found close correlation between the epicenter locations and the east-northeast trending faults west and southwest of Mina.

But not all epicenters are related to faults or lineaments. In study of the earthquakes in Alaska using the Landsat MSS image, Gedney and Van Wormer (1974) noted that:

- Epicenters in the southern part of the area bear little relationship to faults and lineaments. These seismic events were not caused by near surface faulting but were deep-seated earthquakes related to the subduction zone.

- A few earthquakes are associated with the Denali fault, particularly

near Mt. Mckinley. There is an alignment of epicenters along the Lake Clark fault. Most of Landsat lineaments are sites of one or more epicenters and probably should be classified as active faults.

A more systematic investigation of earthquake activities by using remote sensing images was conducted by O'Leary and Simpson (1977). The remote sensing data they utilized included Landsat and SLAR (Side Look Airborne Radar) images, and Skylab photographs. Based on these remote sensing data, an attempt was made to develop a regional tectonic model and to evaluate the seismic hazards of the Mississippi embayment. It is worth to mention that seismic and aeromagnetic data sets were also used besides remote sensing data in their study, therefore an integrated analysis approach was involved. Their result showed that the geomorphic characteristics and the distribution of lineaments reflected the geological structures and tectonics of the area. Well-defined trends of epicenters conformed to a pronounced lineament pattern along the Mississippi River. The tectonic pattern of the study area is generally revealed in the landscape, of which the lineaments seem to be a particularly important part.

One of the recent studies (Shuman, 1989) suggests that there exists a causal association between lineament orientations recognized from satellite images and the direction of maximum compressive stress which leads to a thrust stress regime near the Moodus, Connecticut seismic area. In above studies,

researchers have noted that independent auxiliary information is critical to obtaining meaningful results, in addition to the traditional remote sensing data. Therefore seismic and aeromagnetic data (O'Leary and Simpson, 1977) and geochemical data (Shuman, 1989) were used for this purpose.

Chapter 3

Geological Setting and Earthquake Activities in the Nahanni Study Area

3.1 Physiography

The study area is located in the southwestern Northwest Territories with longitudes and latitudes ranging from 120°W to 128°W, and from 60°N to 64°N (Figure 3.1). The eastern part of the area consists of the Great Slave Plain which lies between the mountain ranges west of longitude 123° and the uplands of the Precambrian Shield. Elevations vary from 150 m to 300 m in most part of the Plain. The entire plain has been glaciated from the east and its surface is characterized by numerous lakes. The thickness of glacial till varies considerably. Pleistocene and Holocene deposits cover the bedrock except along rivers and on escarpments (de Wet et al., 1973).

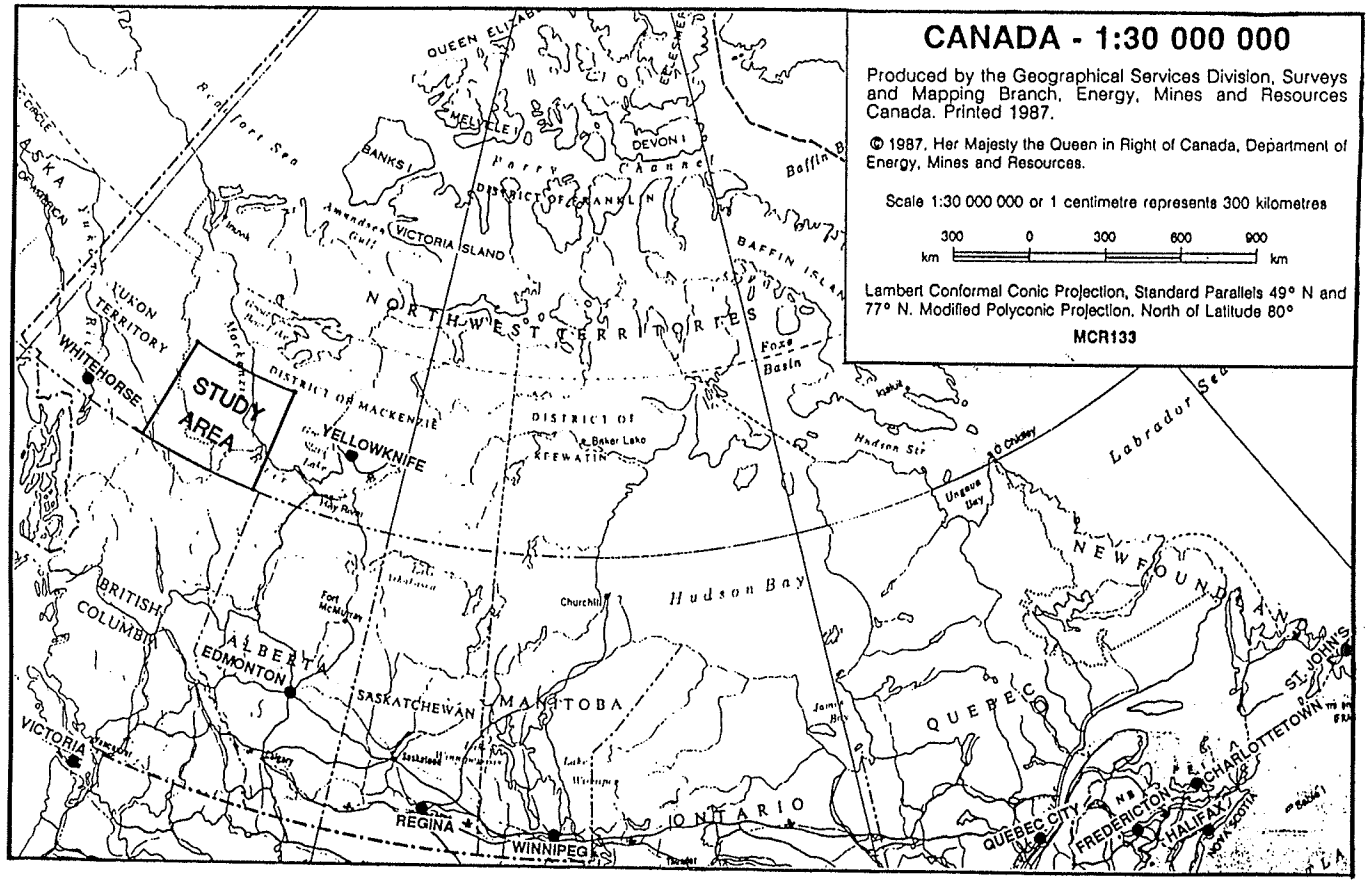

Figure 3.1: Location of the study area.

The mountainous western part of the area consists of northerly to northwesterly trending ranges and broad valleys, forming a distinctly separate morphological as well as structural province. The Franklin Mountains, comprising the easterly chain of ranges, rise abruptly from the adjacent plains and uplands. At the mountain front, upper Precambrian to upper Paleozoic rocks form high cliffs with ridges that reach an elevation of about 1500 m. In the northern part of the area these front ranges are separated from the Mackenzie Mountains by the rolling Mackenzie Plain, which includes the valley of the Mackenzie north of Camsell Band, where the river turns sharply northward.

3.2 Regional Geological Setting

The study area includes parts of several major tectonic and stratigraphic provinces. The eastern part, lying in the Interior Platform, is underlain mainly by sediments of Devonian and Cretaceous age; and the western portion is in the Cordilleran belt, where the accumulation of Phanerozoic sediments has been most persistent (Figure 3.2). The thickness of Phanerozoic sediments in the map area increases in a westward direction. In the Mackenzie Mountains the Cambrian formation increases in thickness and is essentially a carbonate succession which changes into a sequence of shale further westward. In the mountains, Middle Devonian beds of Eifelian age rest unconformably on the lower Devonian. They directly overlie the Silurian in Franklin Mountains.

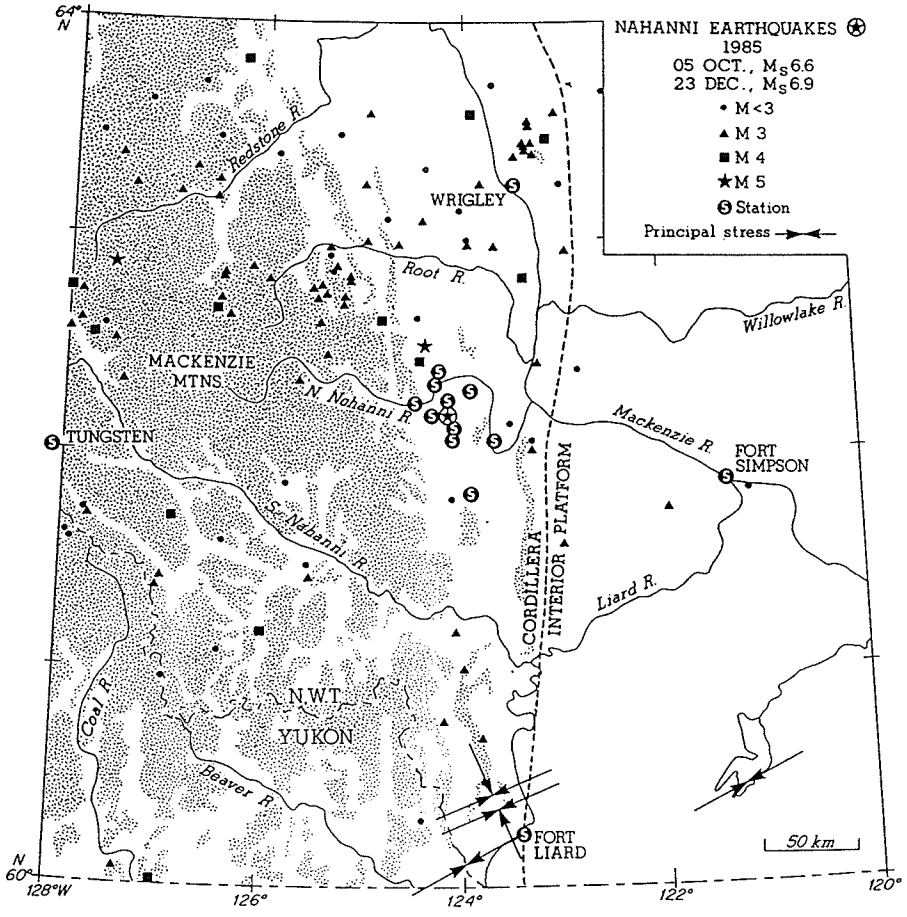

Figure 3.2: Topography and seismicity of the Nahanni study area. Arrows indicate principal stress directions from oil-well breakouts by Adams (1985). Stippled area is land over 1500 m in elevation. (From Wetmiller et al., 1988)

Eastward, in the plains, Middle Devonian beds rest on Precambrian (de Wet et al., 1973).

3.3 Regional Tectonic Structure

Parts of two major tectonic provinces are included in study area; the sedimentary platform and the fold belt. The structural characteristics of the platform has been largely determined by the configuration of the underlying Precambrian rocks, and the folded and faulted mountains are part of the late Cretaceous to early Tertiary (Laramide) orogenic belt, where evidences of the ancient tectonic history are more obscure.

The epicentral zone is located in the Mackenzie Fold Belt, part of the larger Foreland Fold Belt, of the northeastern Cordillera. The Mackenzie Fold Belt is subdivided into four major tectonic units (from east to west):

- The Interior Platform;
- The Franklin Mountains;
- The Mackenzie Plain;
- The Mackenzie Mountains.

The tectonic platform is made of flat-lying Proterozoic and Paleozoic sedimentary rocks unaffected by Laramide Orogeny. Magnetic and subsurface

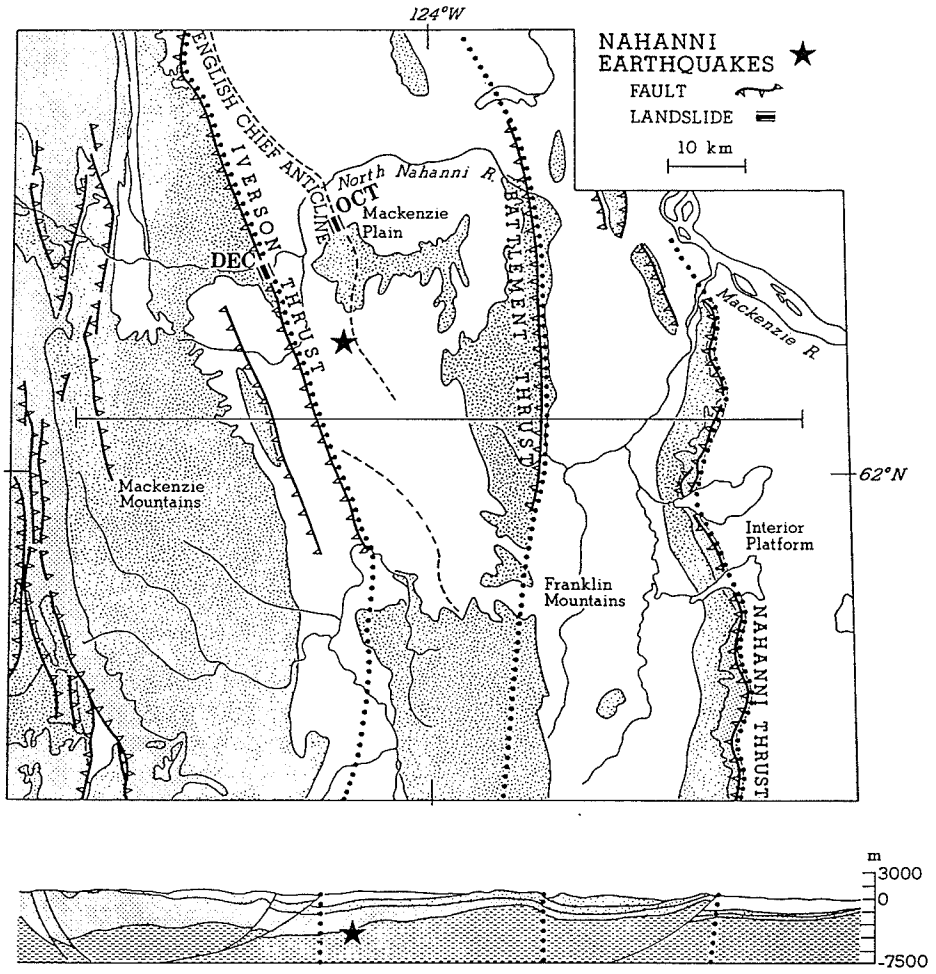

Figure 3.3: Geological setting of the Nahanni earthquake area. Patterns representing stratigraphic units are as shown in Figure 3.4. Main physiographic subdivisions, principal faults, and the sites of landslides which were triggered by the earthquakes are indicated. Epicenters of the main shock are shown. (From Wetmiller et al., 1988)

geological data show that it is underlain by Precambrian rocks of the Canadian Shield that have considerable topographic relief and are cut by many pre-Laramide faults trending northeast (Figure 3.3).

The Franklin Mountains are formed by a narrow chain of large en-echelon, west-dipping thrust faults, with large vertical displacements. An oil company gravity survey suggests that the Franklin Mountains may represent a deeper crustal feature possibly in the craton (Canadian Oil and Gas Lands Administration, 1969). The Mackenzie Plain represents a relatively quiescent belt between the Mackenzie and Franklin Mountains. It is bounded by Battlement and Iverson thrust faults in the east and west. Upper Devonian shales and sandstones with local remnants of Cretaceous beds underlie the area. The Plain features some broad gentle folds, the English Chief Anticline being the most prominent, and is bounded on the west by the Iverson thrust fault.

The Mackenzie Mountains are characterized by broad concentric folds accompanyed by long thrust faults (Figure 3.3). Many anticlines are relatively sharp and are separated by broad synclines, which indicates that a consistent detachment zone may underlie the deformed portion of the section. The anticlines are commonly asymmetrical. Another characteristic of the Mackenzie Mountains is the sinuous arrangement of folds and thrust folds (Figure 3.3). The fold axes as well as the main faults most commonly trend in a northerly direction, but they have been deflected to north-northeast along several shear

zones. Dextral lateral movements between broad slices of the fold belt are evident not only from the general tectonic pattern, but also from offsets in locally mapped structures (Cook et al., 1971).

3.4 Stratigraphy

A stratigraphic section for the upper crust in the Mackenzie Plain is shown in Figure 3.4.

The Precambrian rocks consist of a crystalline basement overlain by a thick sequence of high-velocity Proterozoic sedimentary rocks. Depth to the basement is best determined from an oil company seismic profile carried out across the region in 1970 (Canadian Oil and Gas Lands Administration, 1969). This profile shows reflectors to at least 2.8 s two-way travel time. Using 6.2 km/s as a normal average crustal velocity, this time interval implies a minimum sedimentary thickness of almost 9 km.

Information on the Proterozoic units extrapolated from outside the area suggests a thickness of almost 5 km in the Mackenzie Plain. The Proterozoic sequence consists of shale interbedded with sandstone and dolomite. The Paleozoic rocks consist primarily of dolomites and limestones of Cambrian to mid-Devonian age. Two oil wells drilled down to the base of the mid-Devonian formations show a thickness of at least 2.3 km for these units, with perhaps an

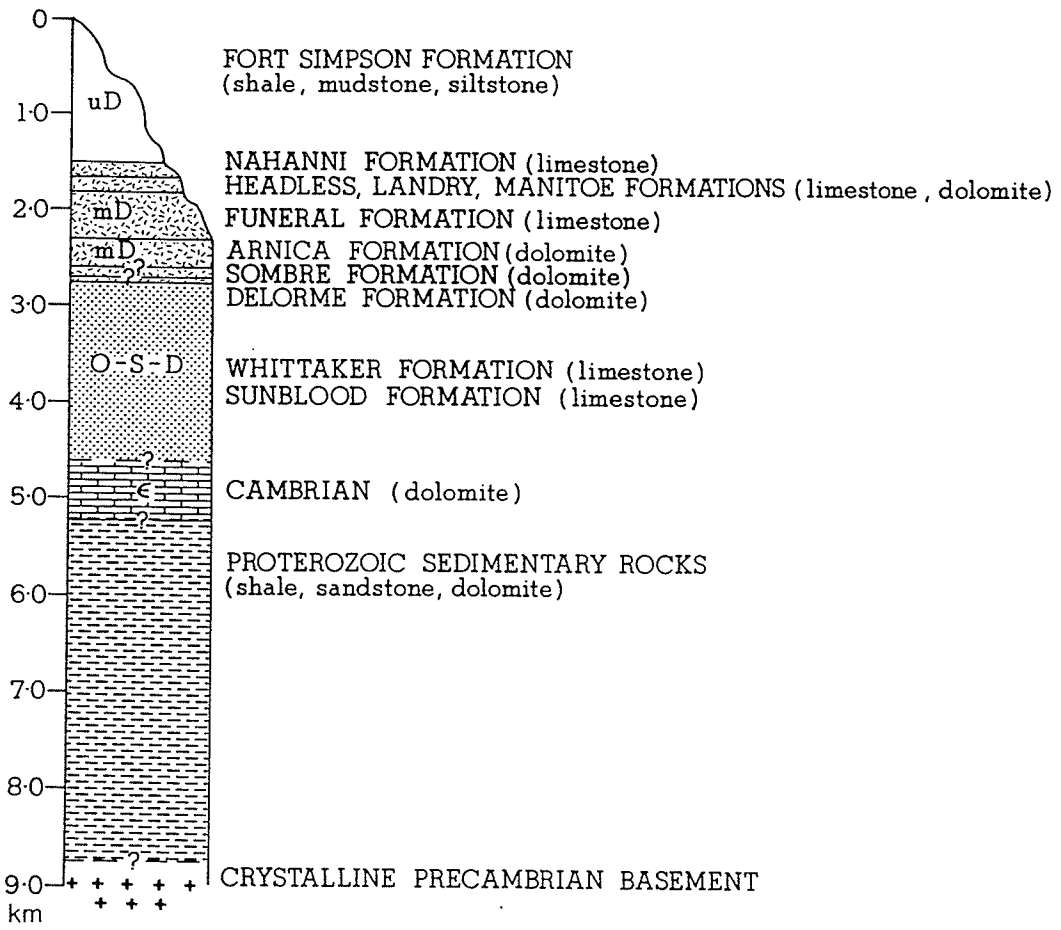

Figure 3.4: Simplified stratigraphic section for the Nahanni earthquake epicentral area. Age of rock units are given by D for Devonian, O for Ordovician, and S for Silurian; u and m are upper and middle, respectively. (From Wetmiller et al., 1988)

additional kilometer for the earlier Paleozoic unit. In some areas of the region, the carbonate rocks are covered by a weathered sequence of upper-Devonian shales and mudstones named the Fort Simpson Formation. These vary in thickness from 0 up to 1.5 km. Thus, total thickness of the sedimentary rocks in the epicentral area appears to be about 10 km or less.

3.5 Earthquake Activities in Nahanni Area

In October and December of 1985, and in March of 1988, three earthquakes of unprecedented magnitude for the region occurred in an uninhabited area near the North Nahanni River, Northwest Territories. These main shocks were followed by extensive aftershock sequences. The magnitudes for the three main shocks were 6.6, 6.9 and 6.0 respectively. Felt areas included the province of British Columbia, Alberta, and Saskatchewan. Interest in each of the events was spurred on one hand by the large felt area and on the other hand by the unique opportunity they presented to study the characteristics and effects of large magnitude intraplate earthquakes in the northeastern Cordillera.

3.5.1 Previous Earthquake Activities

Historically, there was no earthquake of magnitude larger than 5 that occurred in this area. Most large magnitude earthquakes occurred along the

Pacific coastline and beyond.

However, earthquake activities with the magnitude of 6 and below have been very frequent in the northeastern Cordillera.

Figure 3.5 shows the documented earthquake activities in the earthquake data base compiled by the Geological Survey of Canada (GSC) (Wetmilller et al., 1988). A distinct linear band of epicenters extends south from the Beaufort Sea along the eastern boundary of the Cordillera to about 65° N. At this latitude, the epicentral pattern becomes more diffuse, but lesser active events continue to the southeast in to the region where the recent Nahanni earthquakes occurred. There, the activities show no strong linear trends, except that they are confined to the Cordilleran region. The area of the Canadian shield immediately to the east is relatively aseismic. Because the high magnitude detection threshold, large location uncertainty, and low rate of activity, active fault systems are difficult to identify in the historical seismicity records.

Three earthquakes with magnitudes 6 or larger are known to have occurred in the northeastern Canadian Cordillera, a pair of events in 1940s and a single event in 1955 while one other with magnitude 6 event in 1918 is known to have occurred in the southeastern Canadian Cordillera (Rogers and Ellis, 1979). However, no information other than a crude epicenter and magnitude is available for any of the older events.

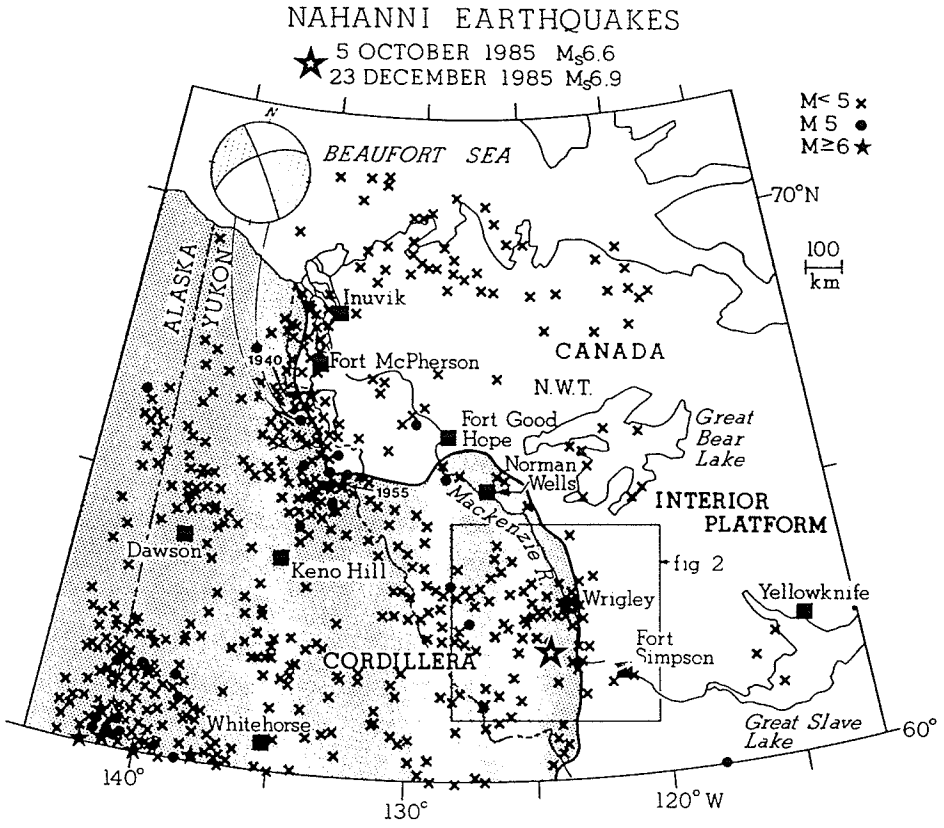

Figure 3.5: Epicenters of Nahanni earthquakes and seismicity of the northeastern Cordillera. Seismicity data are taken from the Canadian Earthquake Epicenter File maintained by the Geological Survey of Canada. Locations of large earthquakes in 1940 and 1955 are indicated. P-nodal solution shown is from Leblanc and Wetmiller (1974). (From Wetmiller et al., 1988)

3.5.2 The Thrust and/or Strike-Slip Faulting Mechanism

Contemporary stress suggests that the crustal rocks in the region are subjected to horizontal compressive stress in the northeast-southwest direction similar to that found in most of North America (Adams, 1985). This kind of stress regime favors thrust and/or strike-slip faulting process.

Leblanc and Wetmiller (1974) determined a right-lateral, strike-slip mechanism for a magnitude 4.8 earthquake in the northern part of the area near Fort McPherson (Figure 3.5), and suggested a correlation between the earthquake activities and the dominant set of north-trending faults in their study area. North-trending thrust faults and folds of late Cretaceous-early Tertiary "Laramide" age, associated with Columbian Orogeny, are prevalent throughout the Foreland Belt of the northeastern Cordillera (Wheeler and Gabrielse, 1972) and represent one of the last major tectonic events in the region. Herron et al.(1974) suggested that this tectonic activity was part of a Cenozoic plate boundary thrust zone created in the later stage of the development of the northeastern Cordillera.

3.5.3 Recent Earthquakes

Each of the three main shocks (two in 1985 and one in 1988) was followed

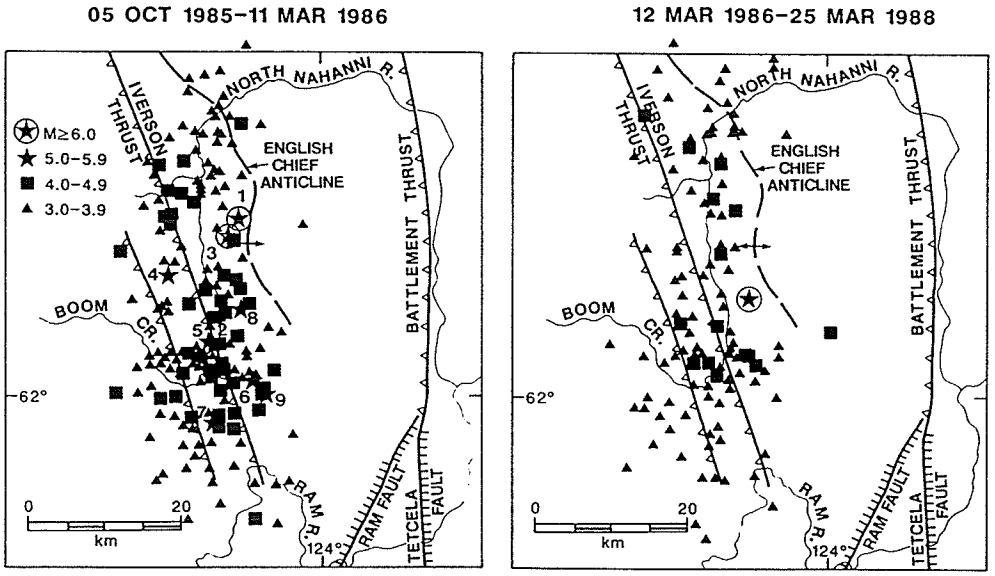

Figure 3.6: Epicenters of Nahanni earthquakes (M 3.0 and greater) from October 5, 1985 to March 11,1986, and from March 12, 1986 to March 25, 1988. The M 5.0 and larger earthquakes are numbered in chronological order up to the M 6.0 earthquake that occurred on March 25, 1988. Numbers 1 and 3 are the October 5 and December 23 main shocks, respectively. (From Horner et al., 1990)

by an aftershock sequence immediately. The epicenters of the 323 located aftershocks that occurred between October 5, 1985 and March 25, 1988 are shown in Figure 3.6 along with the main shock epicenters.

As shown in Figure 3.6, the overall epicentral distribution area extended over a rectangular area measuring approximately 60 km by 20 km, elongated in a north-south direction. The two main shocks in 1985 occurred in the east-

central part of the aftershock zone, while the main shock of 1988 occurred approximately 10 km south.

Figure 3.7 shows the aftershock activity in the first 24 hours immediately following each main shock in 1985. Superimposed are the major tectonic features in the area (Wetmiller et al., 1988). The two distributions are similar and cover a region measuring approximately 50 km in north-south and 15 km in east-west directions. Most aftershocks are located about 10 to 25 km south of the main shock epicenters. Very few events are located in the northern half of the zone. One clear difference in the aftershock distribution was a clear extension of the western edge of the zone. Aftershocks recorded December 23 extend about 5 km further to the west than on October 5.

3.5.4 The Quiescent Zones

There is a seismically quiet zone around each of the main shock epicenters. The rectangles in Figure 3.7 represent aseismic areas of 225 km^2 for the October event and of 195 km^2 for the December event, based on the seismicity observed in the first 24 hours. Choy and Boatwright (1988) showed that the October main shock is comprised of two subevents 3.6 seconds apart. The second subevent is 5.7 km south of the first (Figure 3.7). The December main shock consists of three subevents. The second is 0.8 second after the first and 3.6 km to NNW; the third is 3.5 second later and 4.9 km south of the first.

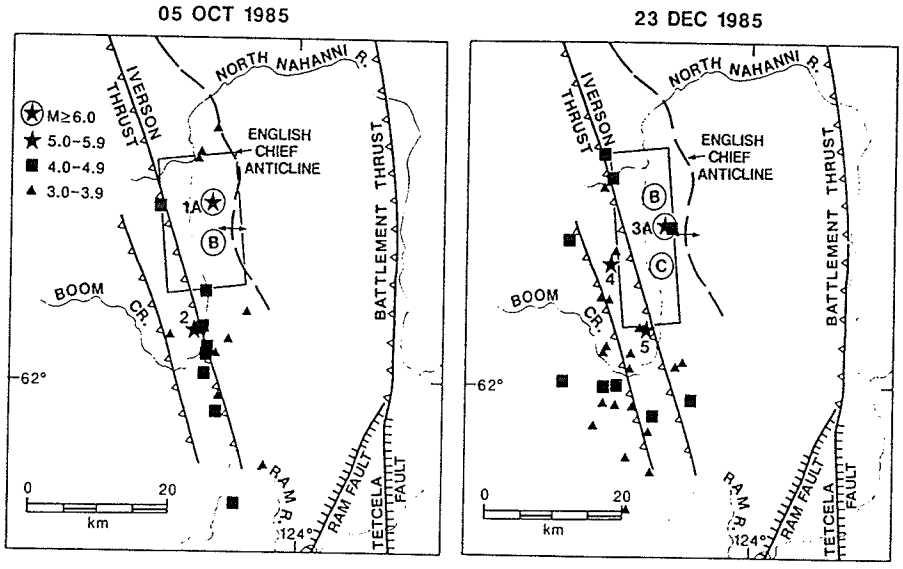

Figure 3.7: The seismicity in the first 24 hours after the October and December main shocks of 1985. Comparison of aftershock activity in the first 24 hours following each main shock. Event numbers are the same as Figure 3.6. A, B, and C show the relative locations of main shock subevents from Choy and Boatwright (1988). The rectangles approximate the extent of quiescent zone around each of the main shock epicenters.

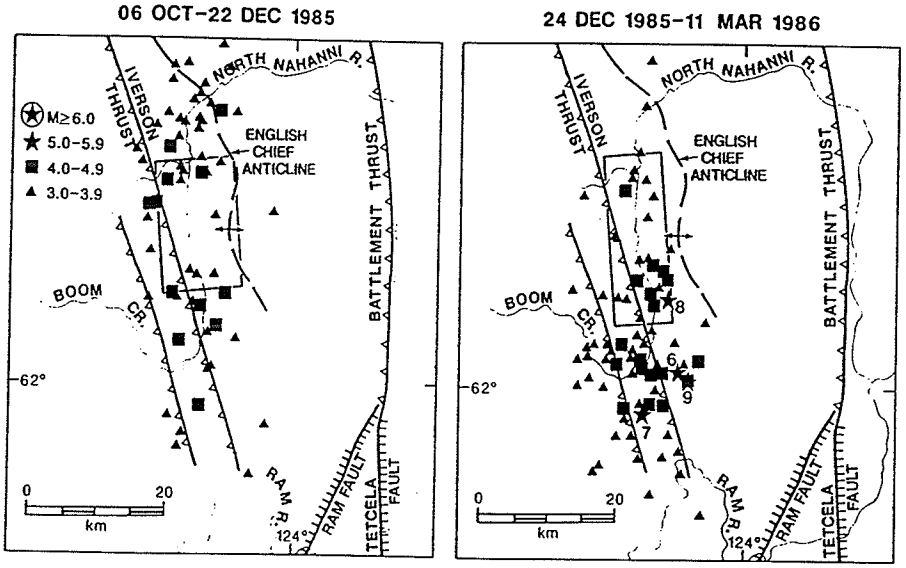

Figure 3.8: Comparison of aftershock activity over a 78-day period from day 1 after each main shock. Event numbers are the same as in Figure 3.6. The rectangles are the same as in Figure 3.7.

The distribution of the subevents corresponds very well with the seismically quiet regions observed in the aftershock distribution (Figure 3.7).

Aftershock activities from October 6 to December 22 1985, and from December 24, 1985 to March 11, 1986 are shown in Figure 3.8.

The two sequences, which were similar during the first 24 hours have become noticeably different in this time period. The October-December aftershocks extend about 10 km further north. Activity becomes more evenly distributed north and south of the main shock. Significantly, the quiescent zone around the main shock continued to be stable. By contrast, the pattern

exhibited by the December-March sequence is much more asymmetric; intense aftershock activity occurred predominantly to the south of the main shock. The quiescent zone appeared to fill in from the south. Horner et al.(1990) suggested that the changes in the quiescent zone of the December event may be due to secondary faulting off the main rupture plane.

Chapter 4

Seismic Data Processing and Earthquake Mechanism Analysis

4.1 Introduction

The seismic data sets used in this research were obtained from two agencies:

- Epicentral information from the Geological Survey of Canada (GSC), (on floppy disks) and
- Broad band digital seismograms in CD-ROMs from the National Earthquake Information Center (NEIC) of U.S. Geological Survey.

Some of these data are integrated with remote sensing data directly to interpret and locate regional surface geological structures related to the earth-

quakes, some of them are utilized to estimate earthquake focal plane solutions and to obtain important parameters for the rupture planes at the hypocenters.

4.2 Epicenter Data

The epicenter data from October 1, 1985 until September 1, 1988 were obtained from the Geophysics Division, the Geological Survey of Canada. The data set includes the origin time, magnitude and epicentral coordinates of each event. Some of this information is given in Table 4.1.

Earthquake Epicenter Data from GSC

Time Period	Min. Lat.	Max. Lat.	Min. Lon.	Max. Lon.	Min. Mag.	No. of Events
Oct. 1, 85 to Jan. 31, 86	61°	64°	-125°	-123°	3.0	399
Feb. 1, 86 to Sept. 1, 88	61°	63°	-125°	-123°	3.0	220

Table 4.1: Geographic information of the earthquake epicenter data in the study area.

These epicenter locations are plotted on the geocoded remote sensing images to facilitate geological interpretation after proper scaling and coordinate registration.

The actual number of event is more than 600, many of which cluster or overlay each other at the given image scale when they are integrated with a

satellite image (see Chapter 7).

4.3 Seismograms of Major Earthquakes

There are in general two sources from which we can obtain seismograms. The Geological Survey of Canada (Geophysics Division) in Ottawa archives the Canadian Standard Seismic Network data, most of which are in paper records. The global seismic data from the GDSN are available from the U.S. Geological Survey.

4.3.1 Global Seismographic Data Network

In order to obtain earthquake focal plane solution, digital seismograms are selected and processed. The data sets used are recorded by the Global Seismographic Data Network (GDSN) (Engdahl et al., 1982) and distributed by the U.S. Geological Survey (USGS). The long period vertical component records are chosen to detect the first motion of the selected events, since they are both more reliable and more indicative than those from short period records.

The Global Seismographic Data Network was established in the early 1970's. There were 10 High Gain Long Period (HGLP) seismographic system installed then (Peterson et al., 1976). Compared with World Wide Standardized Seismic Network (WWSSN) (Peterson and Orsini, 1976), the event

detection threshold for HGLP has been reduced more than one order of magnitude. Another type of seismographic system utilized in GDSN is Seismic Research Observatories (SRO) (Peterson et al., 1976), which were developed for the specific purpose of producing high resolution data in the 20 to 40 s

period band. Operated at a depth of about 100 m, the SRO seismometer is isolated from most wind-generated surface noise in the period band of interest. The system records three components in the long period mode and only the vertical component in short period. The long period digital data are recorded continuously, while the short period digital data are recorded only when the signal is detected. Some of HGLP have been improved by including short period analog and digital records. These stations are called Abbreviated Seismic Research Observatory (ASRO) stations because that their data format is the same as that of SRO stations (Engdahl et al., 1982). Since 1980, digital record instruments have been installed at about 15 existing WWSSN stations, the modified station network is called DWWSSN stations, which record three components for long period, intermediate period and short period signals. Besides the various type of seismographic station mentioned above, Regional Seismic Test Network (RSTN) (Engdahl et al., 1982) is also used as a data source for this study.

Figure 4.1 is a location map of the seismography stations in GDSN. Table 4.2 shows the types of seismic data being recorded at the GDSN and RSTN

networks.

Types of Seismic Data from GDSN and RSTN Networks

Data Type	Recorded Components	Recording Mode	Sampling Rate (Samples/s)	Data Word
ASRO SP	Z	Triggered	20	16-bit gain ranged
ASRO LP	Z,N,E	Continuous	1	16-bit gain ranged
DWWSSN SP	Z	Triggered	20	16-bit integer
DWWSSN IP	Z,N,E	Triggered	10	16-bit integer
DWWSSN LP	Z,N,E	Continuous	1	16-bit integer
RSTN SP	Z,N,E	Continuous	40	16-bit gain ranged
RSTN MP	Z,N,E	Continuous	4	16-bit gain ranged
RSTN LP	Z,N,E	Continuous	1	16-bit gain ranged
SRO SP	Z	Triggered	20	16-bit gain ranged
SRO LP	Z,N,E	Continuous	1	16-bit gain ranged

Table 4.2: Seismic Data types recorded at the GDSN and RSTN stations.

4.3.2 GDSN Data Flow

GDSN data flow from the stations to the users is shown in Figure 4.2. The station tapes contain from 1 to 2 weeks of data. They are reviewed and edited by Albuquerque Seismological Laboratory (ASL) of USGS, then are placed in a disk file. Network-day tape provides a 1-day block of network digital data completed with all essential information including station parameters and calibration data. For the reason of convenient exchange and access, GDSN

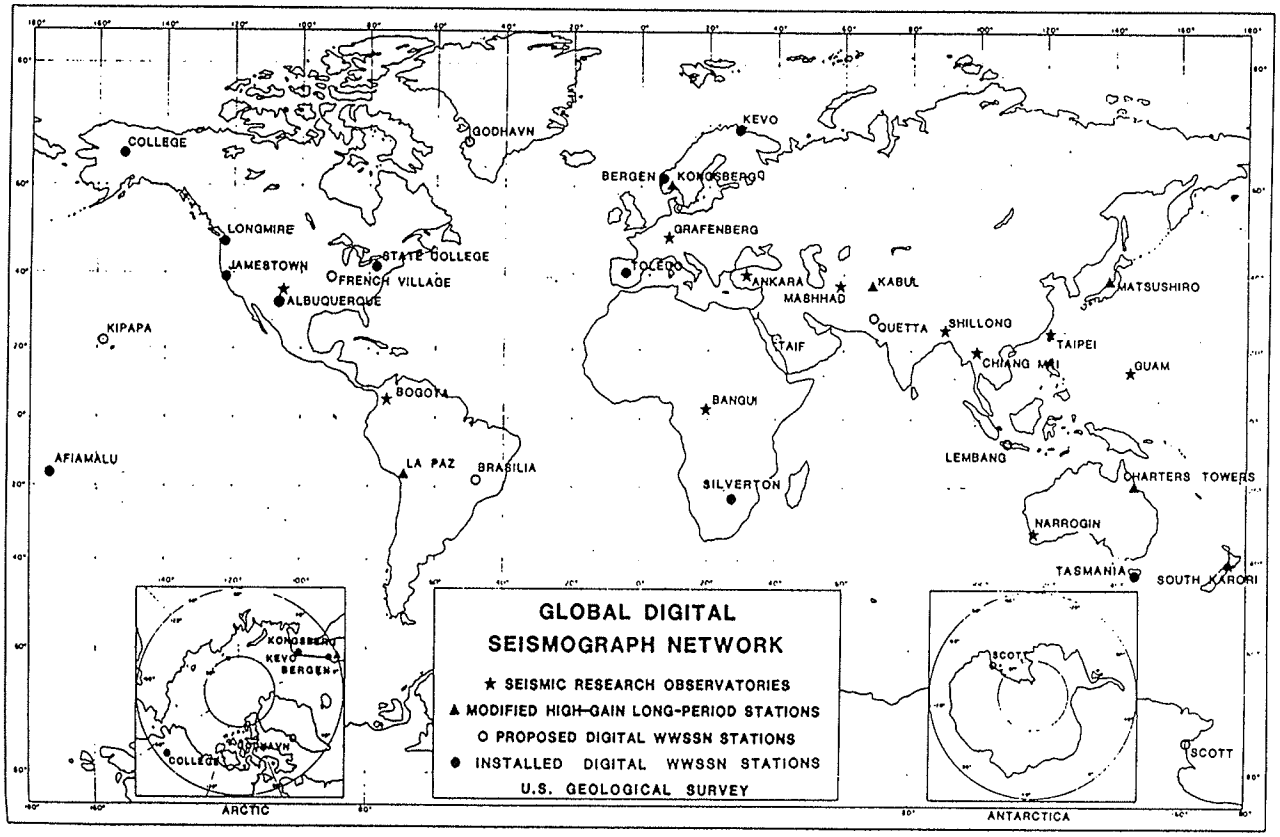

Figure 4.1: The GDSN stations comprised of SRO, modified high-gain, long-period ASRO, and DWWSSN data systems.

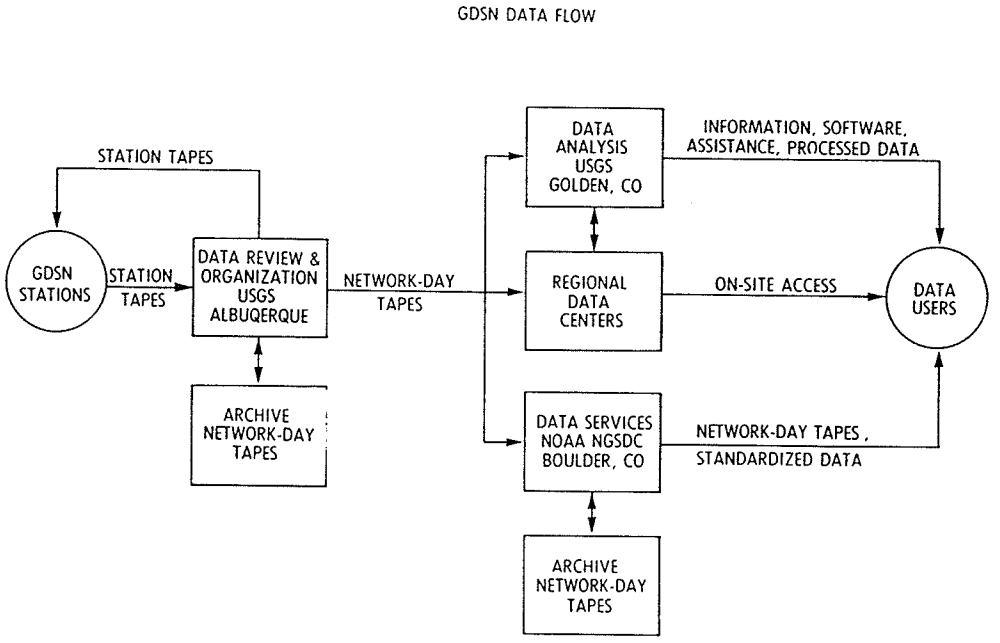

Figure 4.2: A schematic data flow path of the GDSN data.

data are now available in CD-ROMs.

The GDSN data used in this research was provided by the NEIC of USGS, contained in several CD-ROMs. The software needed to retrieve data from the CD-ROM disk was also provided by USGS.

4.4 Teleseismic Data Analysis

Digital data processing of teleseismic events can include filtering, scaling,

deconvolution, cepstrum analysis and other tasks. This thesis study does not focus on these traditional data processing steps. The teleseismic data analysis in this thesis is more focused on the focal plane solution and on the subsequent analysis of the results.

4.4.1 Introduction

The main objective of teleseismogram data analysis is to determine the polarity of the first motions of each seismogram and to obtain focal solutions for the earthquakes. These solutions are then used to support possible fault planes in the study area and other related geological structures that can be correlated to the observed features in remote sensing images. Five recorded events with magnitudes larger than 5 are selected and named as Event 1, Event 2 ..., Event 5 following the origin time sequence, of which Event 1 and 2 are main shocks, and the rest are aftershocks. Table 4.3 lists related information on the five chosen events.

GDSN data have a wide dynamic range and high recording precision, and they are suitable for source parameter estimation study (Choy and Boatwright, 1981). The primary concern in this research, however, is the focal parameters. For this purpose, the long period vertical component of the seismograms from the stations which are within 105° angular distance from the epicenters are analyzed. First P wave motions from these seismograms are used, since they

Event Information

Event No.	Date	Time	Lat.	Lon.	Depth (km)	M_b	M_s
1	1985 10 05	15:24: 2.25	62.257	-124.312	10.0	6.5	6.6
2	1985 12 23	05:16: 3.91	62.207	-124.302	10.0	6.4	6.9
3	1985 12 23	05:48: 47.44	62.177	-124.269	10.0	5.5	?
4	1985 12 23	19:37 54.80	62.062	-124.301	10.0	5.5	5.0
5	1985 12 25	15:42: 42.44	62.075	-124.153	10.0	5.7	5.0

Table 4.3: The GDSN Network Day Tape Log for the five earthquake events in the study area.

are both more reliable and more indicative. Other reflected phases, such as $_pP$ and PP, may also be used after proper correction for propagation effects (e.g. reversal of polarity by reflection at a free surface), but they were judged to be too risky with the chosen data sets. Table 4.4 lists the information of GDSN stations where the chosen seismograms were recorded for the present focal plane solutions.

4.4.2 Radiation Pattern at Foci

The polarity of the initial P-wave pulse from an earthquake will take either of two opposite sense, compressional (push) or dilatation (pull) according to whether the particle motion is away from or towards the epicenter with respect to the force couple model chosen. The systematic distribution of the initial first

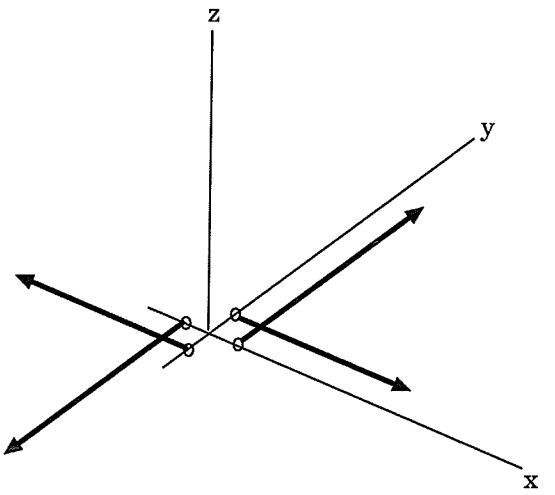

Figure 4.3: Double-couple point source model; Two pairs of forces. The torques about the z-axis are of equal magnitude and are opposite to each other.

motion polarity in azimuth has an essential bearing on the focal mechanism, i.e. the mechanism of seismic wave radiation from the focus. Now, it is generally accepted that a double-couple type (Figure 4.3) as a reasonable point-source model of earthquakes (Kasahara, 1981).

The displacement field of double-couple point source types can be described by the following equations:

$$\begin{aligned} u &= -\frac{1}{4\pi\rho}[2\frac{\partial^3}{\partial x^2\partial y}(\phi-\psi)+\frac{\partial}{\partial y}\nabla^2\psi] \\ v &= -\frac{1}{4\pi\rho}[2\frac{\partial^3}{\partial x\partial y^2}(\phi-\psi)+\frac{\partial}{\partial x}\nabla^2\psi] \\ w &= -\frac{1}{4\pi\rho}[2\frac{\partial^3}{\partial x\partial y\partial z}(\phi-\psi)] \end{aligned} \tag{4.1}$$

where u, v, and w are the displacement components in the x, y and z direc-

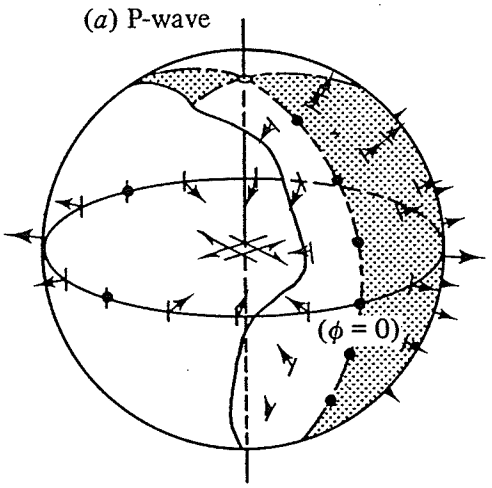

Figure 4.4: Radiation pattern of P wave from a double-couple source. (From Kasahara, 1981)

tions respectively, and ρ is the density, ϕ and ψ represent spherical waves. A schematic sketch of P wave radiation displacement field derived from Eq(4.1) is shown in Figure 4.4. In a three dimensional view, the radiation pattern of P wave is characterized by a pair of orthogonal nodal planes which separate compressions from dilatations (Kasahara, 1981).

4.4.3 First Motion Recognition

The basic requirement of a focal solution is to identify and pick the first motion of the direct P wave and determine its polarity. Such a task could be very challenging and even impossible when noise level exceeds a certain limit

or there is abnormal station bias. When several wave phases arrive close to each other, experiences are essential to distinguish them. In this research, a FORTRAN program WKBJ (Chapman, 1978) and the Earth Model 1066B are utilized to help identification of the first motion arrivals.

The near surface portion of the Earth Model 1066B is given in Table 4.5, in which a horizontally homogeneous earth is assumed and the density of the earth and seismic velocity only vary with the depth. By choosing a spherical coordinate system and properly setting parameters, a group of turning wave can be simulated (Figure 4.5) for direct P-phase modelling.

The most important output for this study from the WKBJ program is the travel time table, which lists the traveling time of P phase vs epicentral distance. A sampling list of the travel time table is given in Table 4.6.

Linear interpolation is applied when the travel time table is used to look up a travel time between an epicenter and a specific station. To use the obtained travel time table, the epicentral distance between a station and the epicenter must be known. The Figure 4.6 shows how to calculate the epicentral distance between an epicenter (θ_1, ϕ_1) located in north hemisphere and any station (θ_2, ϕ_2) world wide by using spherical trigonometry.

In this configuration, A, B and C represent angles and a, b and c represent

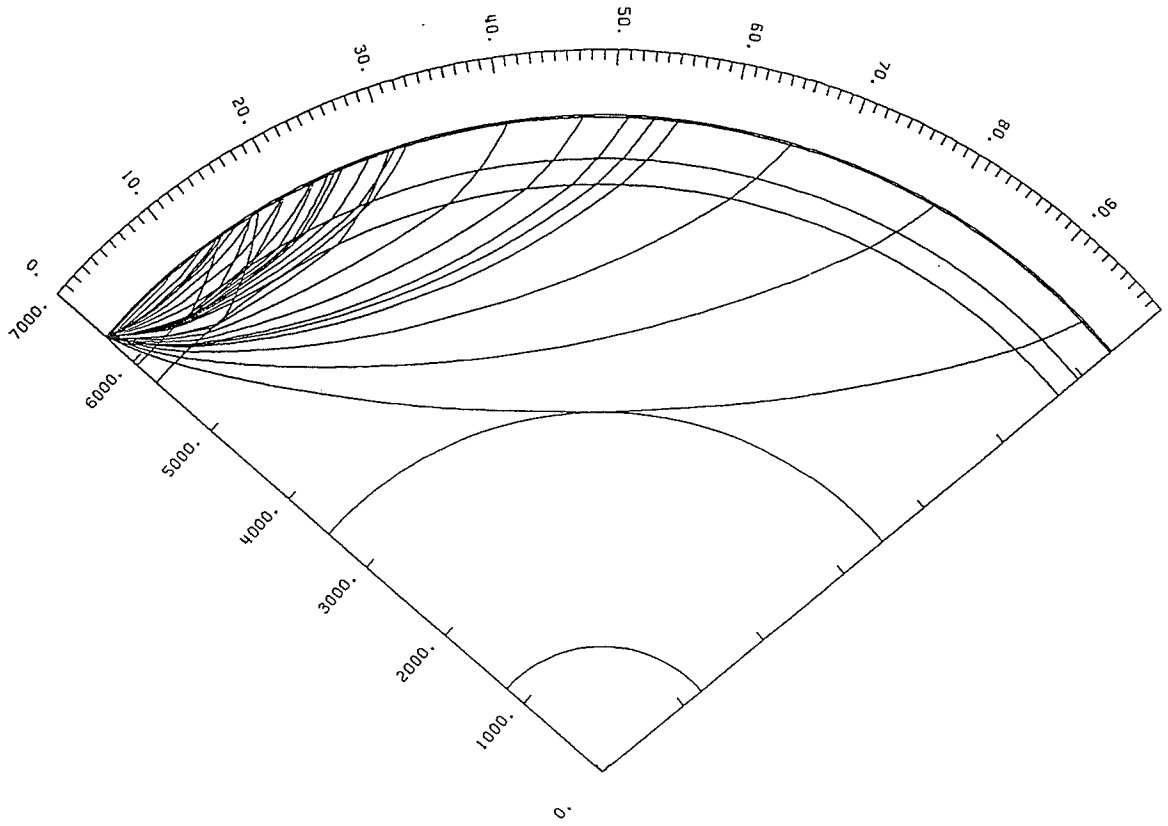

Figure 4.5: Plot of ray paths for turning rays computed using WKBJ algorithm (Earth Model 1066B.)

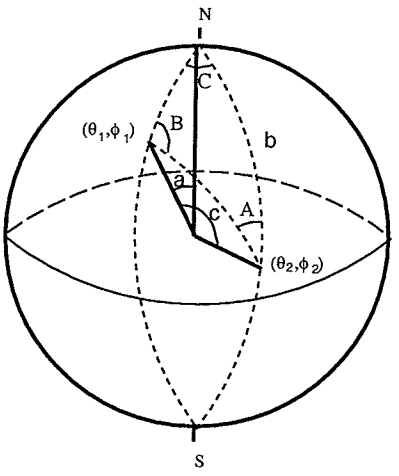

Figure 4.6: Spherical coordinate geometry used for calculation of epicentral distance.

sides measured by the angles subtended at center of the sphere. We have the following relation:

$$\cos c = \cos a \cos b + \sin a \sin b \cos C \quad . \tag{4.2}$$

Substitute a, b and C with the corresponding longitudes θ_1, θ_2 and latitudes ϕ_1 and ϕ_2, the above equation becomes

$$\cos c = \sin \phi_1 \sin \phi_2 + \cos \phi_1 \cos \phi_2 \cos(\theta_2 - \theta_1) \tag{4.3}$$

or,

$$c = \cos^{-1}[\sin \phi_1 \sin \phi_2 + \cos \phi_1 \cos \phi_2 \cos(\theta_2 - \theta_1)] \quad . \tag{4.4}$$

When the station is located in the south hemisphere, Eq(4.4) is replaced by :

$$c = \cos^{-1}[-\sin\phi_1 \sin\phi_2 + \cos\phi_1 \cos\phi_2 \cos(\theta_2 - \theta_1)] \quad . \tag{4.5}$$

Similarly, the azimuth of the station, B is calculated using Eq(4.6) or Eq(4.7) for a station located in the south hemisphere:

$$B = \cos^{-1}(\frac{\sin\phi_2 - \sin\phi_1 \cos c}{\cos\phi_1 \sin c}) \tag{4.6}$$

$$B = \cos^{-1}(\frac{-\sin\phi_2 - \sin\phi_1 \cos c}{\cos\phi_1 \sin c}) \quad . \tag{4.7}$$

When equations Eq(4.6) and Eq(4.7) are used to calculate the epicentral distance, the following convention is observed. The longitude varies from 0$\sim$ 180° within the East Hemisphere while it varies from -180° $\sim$ 0° in the West Hemisphere; the latitude varies from 0$\sim$ 90° in the North Hemisphere while it varies from 0° $\sim$ $-90°$ in the South Hemisphere. The first motion of P mode on a seismogram is usually located by identifying its specific waveform and checked by the following formula:

$$T_f = T_t - T_e + T_r \tag{4.8}$$

where,

- T_f: the time of P mode first motion on a seismogram;
- T_t: the P travel time between the epicenter and the station, which can be obtained from P travel time table (Table 4.6) or directly from a synthetic seismogram program;

- T_e: the event time obtained from the GDSN Day Tape Log;
- T_r: the beginning of the recording time of a specific event obtained from the Station Log.

At many stations, the first motion picked up manually and the T_f estimated using Eq(4.8) matched very well (Figure 4.7, Station LON and TATO). But at some stations, seismograms have been so seriously distorted that it is impossible to identify any meaningful signal(Figure 4.7, Station RSNT).

For data sets used in this study, the seismograms for Event 1 and 2 have good quality apparently due to their large earthquake magnitudes(Table 4.3). But for the rest of the events the data quality deteriorates considerably.

4.5 Construction of the Focal Solution

A graphical technique is applied to construct the focal plane solutions using the world wide seismogram data from GDSN. The principle of this technique is briefly described bellow:

Let us surround the focus with a unit sphere, which is called the focal sphere (Figure 4.8). A seismic ray reaching a station S leaves the sphere with an emergence angle i, which is a function of the epicentral distance Δ. We assign S′ to the point on the sphere where the seismic ray pierces. The

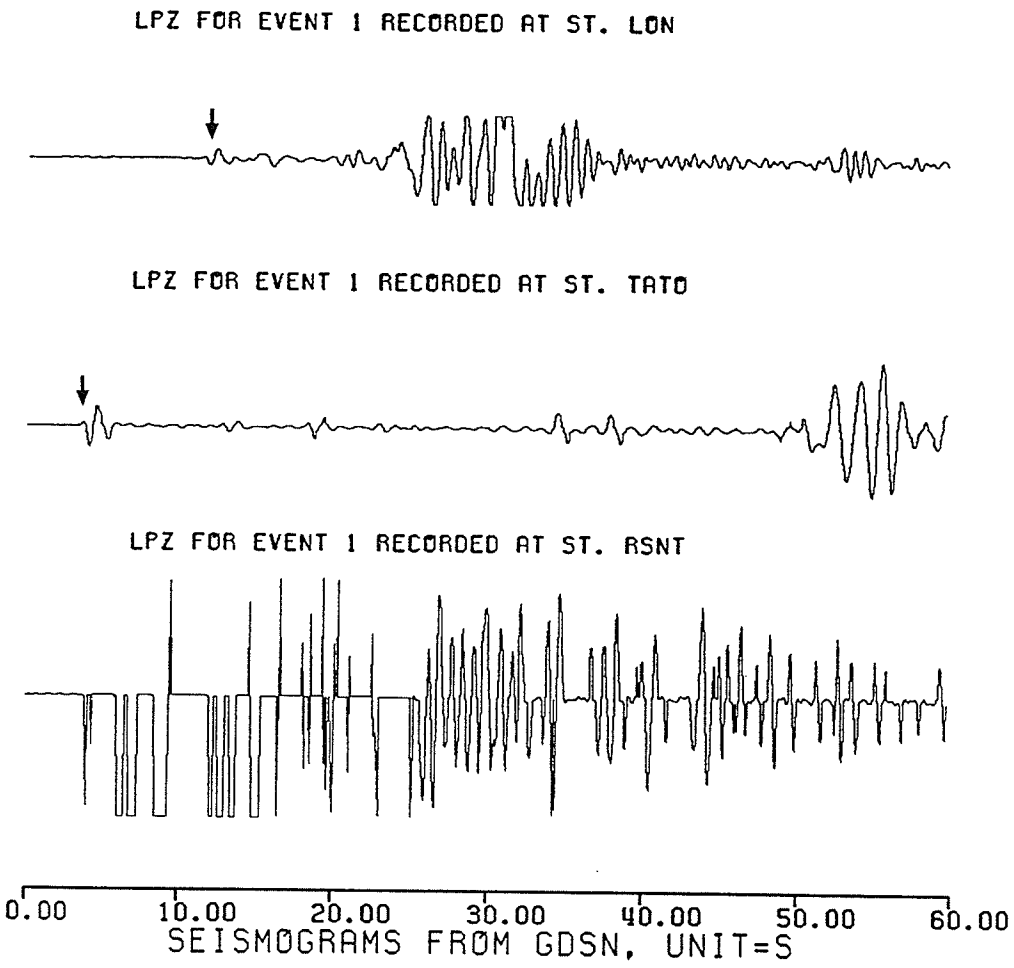

Figure 4.7: First motion picked from a GDSN seismogram.

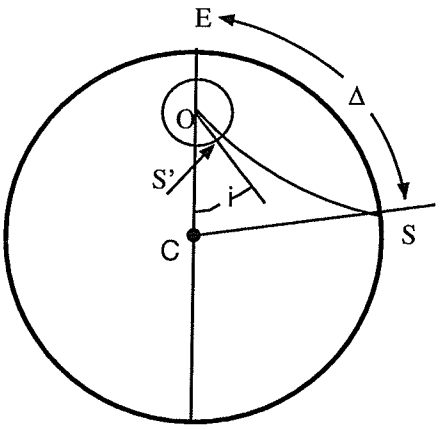

Figure 4.8: Schematic diagram of focal solution construction.

polarity of the initial P-phase as observed at S, which can be determined from a station seismogram, then represents S′ as the data at S. When one repeats this process for all the station data available for a seismic event, one obtains a comprehensive seismic wave radiation pattern on the unit sphere. Under the assumption that the initial characteristics of a seismic ray should remain unchanged during its propagation, evidences on the focal sphere should faithfully represent the original polarity of source wave radiation (Kasahara, 1981). Based on the source mechanism described and shown in Eq(4.1) and Figure 4.4, the P-wave radiation pattern on the focal sphere will then be separated by a pair orthogonal planes into four regions of alternate signs, compressional and dilatational. This graphic process is usually accomplished by using stereographic projection with Wulff net.

In the graphic illustration, the azimuth of each station relative to the

epicenter is calculated using Eq(4.6) or Eq(4.7) and the angle of emergence i is obtained from an existing table.

The results show that focal plane solutions are all in some similar pattern (Figure 4.9-4.11); the nodal plane A is defined quite well while the nodal plane B involves a lot of uncertainty in every fault plane solution. One of the main reasons for this uncertainty comes from the uneven distribution of the stations available for this study.

4.6 Discussion of the Source Parameters

The source parameters obtained from the focal solutions (Figure 4.9-4.11) provide important structural geological information concerning the earthquake mechanism. Some of these parameters for each event studied are listed in Table 4.7.

Except for Event 3, all the focal solutions suggest a thrust faulting involving the fault plane rupturing. Among them, the two nodal plane in Event 1 are somewhat symmetrical while for Event 2, 4 and 5, the nodal plane B has shallower dip angle than that of the nodal plane A. The focal plane solution for Event 3 is very different from others. Both nodal planes of Event 3 are almost vertical and the dilatational and compressional movement configuration shows a strike-slip faulting.

For most events, the strikes of the nodal planes are close, but it is difficult to find the actual focal plane by only using the principal axis of the foreshock/aftershock distribution cluster. In this case, the regional structural geology, the regional stress orientation and the epicentral distribution of the aftershock should be utilized to determine the actual focal planes.

Figure 3.3 shows that this region is predominated by west dipping thrusting faults in the general north or northwest direction. The stress measurements from oil well breakouts indicate that the principal stress is near horizontal and compressive along N60E trend (Wetmiller et al., 1988), while the the trend of the P axis for Event 1, 2 and 5 are more in east-west direction along 91° $\sim$ 96°, and the trend for Event 4 is almost identical with the direction of the principal stress. Also the hypocentral information of the aftershocks is very indicative. Figure 4.12 shows that the distribution of aftershock zone for the October and December main shocks.

Viewed in cross-section A-A′ in Figure 4.12 (a), across the regional geological strike (N160°E), the hypocenter cluster shows an indistinct dip to the west, with the lower edge of the hypocenter dipping approximately 20° $\sim$ 40° to the west. Most seismic activities lie east of the Iverson fault. The combination of the above information favors a west dipping thrust fault plane, and therefore the plane A appears to bear the attitude of the actual rupture plane except for Event 3. The focal solution for Event 3 involves a larger degree of

uncertainty. One of the reason is that Event 3 has relatively small magnitude (Table 4.3), thus the data set has a lower signal to noise ratio. The initial P-pulse motion is obscure at several stations. No actual focal plane can be determined for this event based on the information obtained so far.

Station Information

Name (Code)	Instru. Type	Lat./Lon.	Elevation	Epicentral Distance	Epicentral Azimuth
Albuquerque, New Mexico (ANMO)	SRO	34.9462 N 106.4566 W	1740 m	29.48°	149.306 E
Ankara, Turkey (ANTO)	SRO	39.868 N 32.7935 E	883 m	76.27°	107.909 E
Guam, Marianas Islands (GUMO)	SRO	13.5878 N 144.8662 E	14 m	78.39°	82.72 W
Chaing Mai, Thland (CHTO)	SRO	18.7900 N 98.9769 E	316 m	92.09°	40.5 W
Grafenberg, Germany (GRFO)	SRO	49.6919 N 11.2217 E	500 m	62.65°	38.68 E
Taipei, Taiwan (TATO)	SRO	24.9754 N 121.4880 E	53 m	78.45°	57.55 W
Shillong, India (SHIO)	SRO	25.5666 N 91.8833 E	1600 m	87.85°	32.21 W
Glan Alinond, Quebec (GAC)	SRO	45.7031 N 75.4783 W	62 m	32.05°	97.91 E
Zongo Valley, Bolivia (ZOBO)	SRO	16.2700 S 68.1250 W	4450 m	89.69°	127.11 E
Matsushiro, Japan (MAJO)	ASRO	36.5416 N 138.2088 E	422 m	61.45°	65.07 W
Kongsberg, Norway (KONO)	ASRO	59.6490 N 9.5982 E	216 m	53.12°	27.07 E
State College, Pennsylvania (SCP)	DWWSSN	40.7949 N 77.8650 W	352 m	34.79°	105.96 E
College Outpost, Alaska (COL)	DWWSSN	64.8999 N 147.7931 W	320 m	10.73°	65.21 W
Longmire, Washington (LON)	DWWSSN	46.7500 N 121.8100 W	854 m	15.52°	173.61 E
Jamestown, California (JAS1)	DWWSSN	37.9267 N 120.4199 W	425 m	24.39°	172.57 E
Honolulu, Hawaii (Hon)	DWWSSN	21.3216 N 158.0082 W	2 m	46.92°	134.95 W
Kevo, Finland (KEV)	DWWSSN	69.7553 N 27.0066 E	80 m	46.49°	13.24 E
Godhaven, Greenland (GDH)	DWWSSN	69.2500 N 53.5331 W	23 m	28.16°	45.15 E
Brazilia, Brazil (BDF)	DWWSSN	15.6636 S 47.90 W	1500 m	97.456°	109.216 E
Toledo, Spain (TOL)	DWWSSN	39.8814 N 4.0484 W	480 m	67.23°	45.96 E
Cumberland Plateau, Tennessee (RSCP)	RSTN	35.5999 N 85.5688 W	481 m	35.83°	120.02 E
Yellow Knife, N.W. T. (RSNT)	RSTN	62.4797 N 114.5916 W	90 m	4.51°	82.243 E
Adirondack, New York (RSNY)	RSTN	44.5483 N 74.5299 W	351 m	33.36°	98.37 E
Red Lake, Ontario (RSON)	RSTN	50.8589 N 93.7021 W	302 m	20.04°	110.32 E
Noress Array Site A0 (NRA)	NKSA	60.7353 N 11.5414 E	302 m	52.54°	25.41 E

Table 4.4: The contents of Network Tape Log (CD-ROM Data) for the GDSN stations.

The Earth Model 1066B

Interface No.	Depth (km)	P Velocity (s/km)	P Slowness (km/s)	S Velocity (km/s)	S Slowness (s/km)	Density (mg/m^3)
1	0.0	6.2	0.16129	3.4	0.294118	2.802
	10.51	6.2	0.161025	3.4	0.293633	2.802
	21.03	6.2	0.160759	3.4	0.293148	2.802
2	21.03	7.742	0.128740	4.759	0.209436	3.293
	46.06	7.808	0.127151	4.725	0.210115	3.309
	71.29	7.881	0.125475	4.624	0.213856	3.321
	96.53	7.947	0.123941	4.514	0.218202	3.323
	121.85	8.021	0.122311	4.416	0.222159	3.338
	147.39	8.098	0.120663	4.355	0.224370	3.351
	172.93	8.176	0.119034	4.344	0.224038	3.364
	198.66	8.245	0.117562	4.343	0.223186	3.387
	224.40	8.315	0.116102	4.382	0.220308	3.409
	250.25	8.392	0.114571	4.453	0.215918	3.434
	276.30	8.470	0.113053	4.532	0.211288	3.461
	302.36	8.544	0.111616	4.599	0.207360	3.488
	328.53	8.616	0.110230	4.657	0.203938	3.512
	354.90	8.688	0.108865	4.710	0.200811	3.535
	381.29	8.761	0.107512	4.748	0.198380	3.562
	407.88	8.832	0.106203	4.765	0.196849	3.593
	434.48	8.893	0.105035	4.796	0.194762	3.605
3	434.48	9.515	0.098168	5.052	0.184892	3.746
	468.19	9.581	0.096978	5.112	0.181758	3.779
	501.96	9.639	0.095884	5.161	0.179081	3.821
	536.03	9.703	0.094744	5.203	0.176688	3.865
	570.27	9.762	0.093667	5.259	0.173869	3.906
	604.71	9.805	0.092753	5.306	0.171400	3.958
	639.22	9.859	0.091747	5.363	0.168662	4.003
	674.03	9.900	0.090869	5.415	0.166133	4.049
	709.03	9.945	0.089962	5.475	0.163412	4.100

Table 4.5: Lithosphere model of the Earth Model 1066B.

P Wave Travel Time

(A part of the Time Table, from WKBJ Program)

Epicentral Distance (°)	P Travel Time (s)	P Slowness (s/km)	τ
1.4229	24.4350	0.12870	4.0731
2.2456	36.2040	0.12859	4.0956
2.8568	44.9404	0.12847	4.1307
3.3929	52.5940	0.12833	4.1787
3.8882	59.6573	0.12818	4.2405
4.3570	66.3358	0.12801	4.3170
4.8068	72.7338	0.12783	4.4097
5.2417	78.9107	0.12764	4.5178
5.6641	84.9001	0.12743	4.6420
6.0758	90.7295	0.12721	4.7843
6.3729	94.9284	0.12699	4.9420
6.7066	99.6362	0.12675	5.1145
7.0462	104.4167	0.12650	5.3043
7.3840	109.1656	0.12624	5.5106
7.7175	113.8402	0.12598	5.7309
8.0455	118.4313	0.12571	5.9687
8.4363	123.8870	0.12543	6.2201
8.8751	130.0004	0.12515	6.4914
9.2549	135.2796	0.12487	6.7782

Table 4.6: The P wave travel time table computed using the WKBJ algorithm (Chapman, 1978) with Earth Model 1066B.

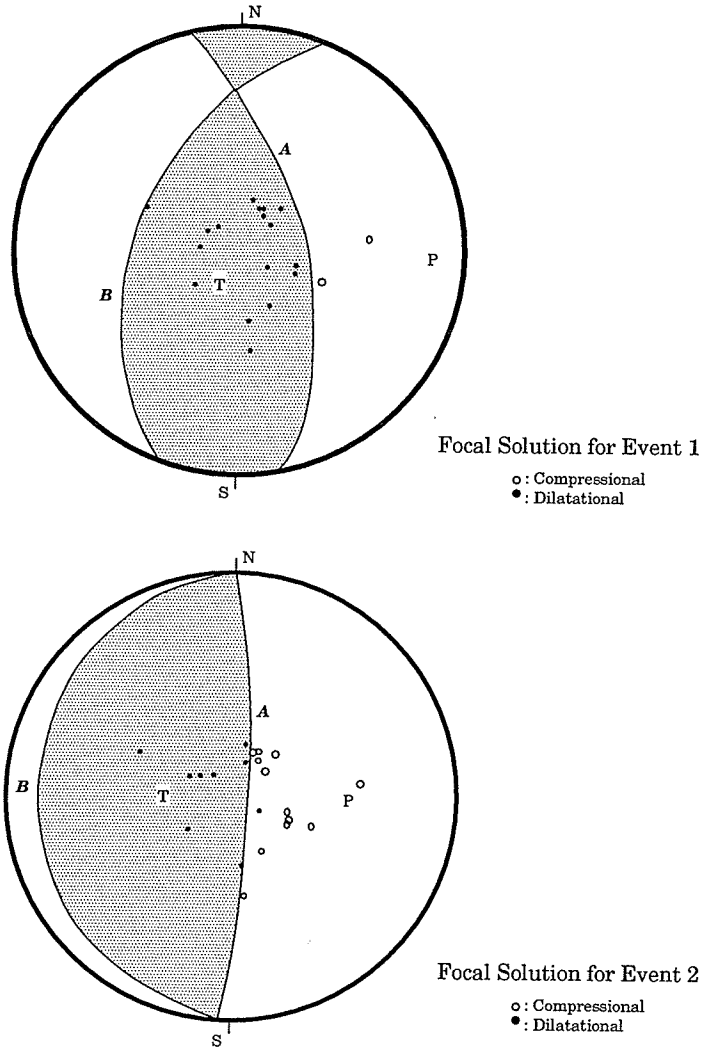

Figure 4.9: The focal solution for Events 1 and 2. (See Table 4.3 for event numbering)

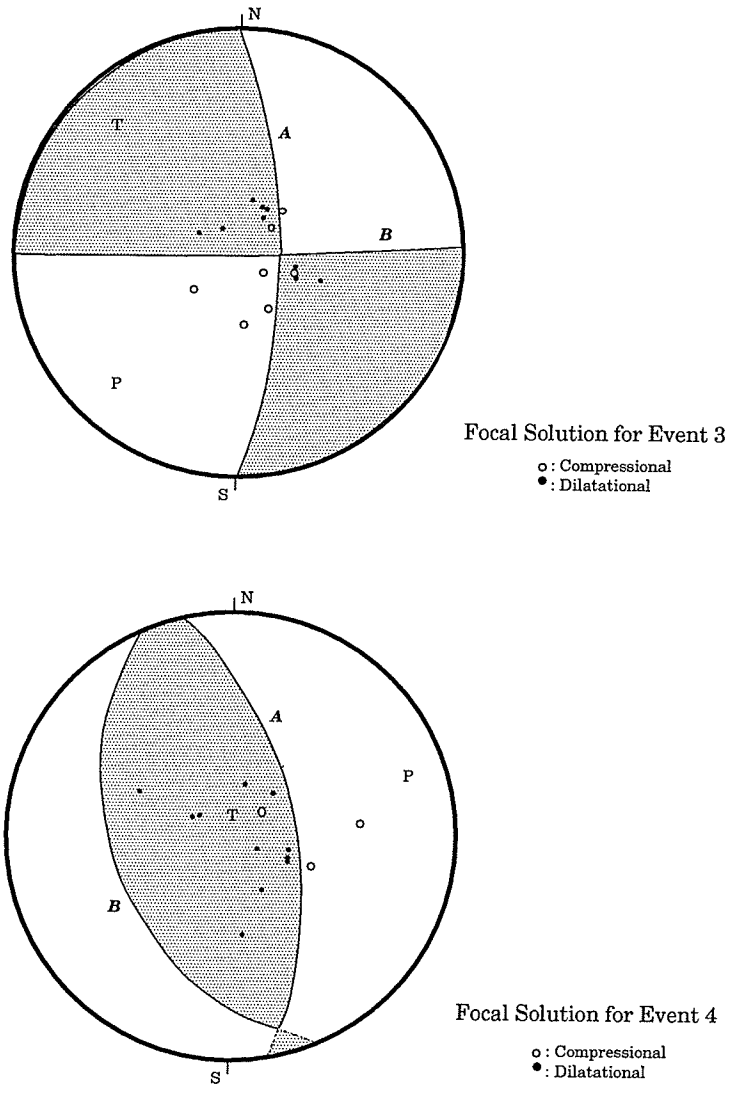

Figure 4.10: The focal solution for Events 3 and 4.

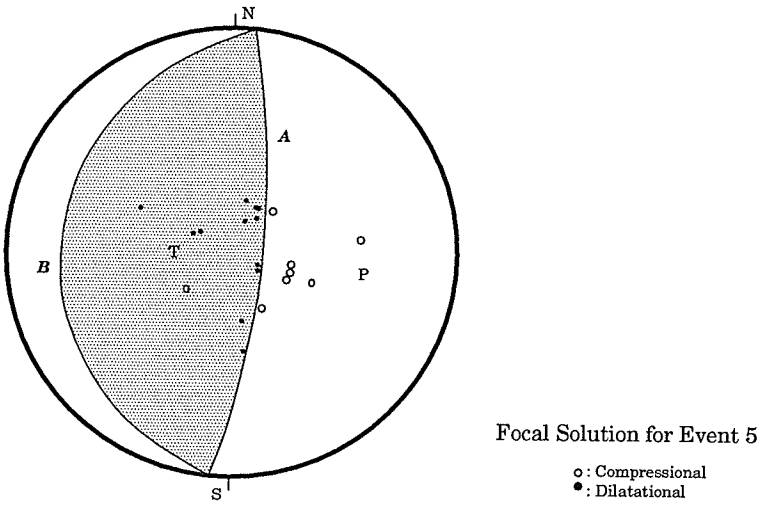

Figure 4.11: The focal solution for Event 5.

Focal Parameters of the Nahanni Earthquakes

Event No.	Plane A		Plane B		T Aix		P Aix	
	Strike	Dip	Strike	Dip	Trend	Plunge	Trend	Plunge
1	N13°W	56°W	N21°E	40°E	205°	71°	91°	82°
2	N1.5°E	80°W	N1.5°E	10°E	271°	55°	91°	35°
3	0°	69°W	N89°E	90°N	316°	15°	223°	14°
4	N12°W	57°W	N24°W	35°E	276°	78°	59°	10°
5	N5°E	74°W	N5°E	16°E	275°	61°	96°	29°

Table 4.7: The fault parameters of focal solution for the main shock Events 1 and 2, and aftershock Events 3,4 and 5 in the study area.

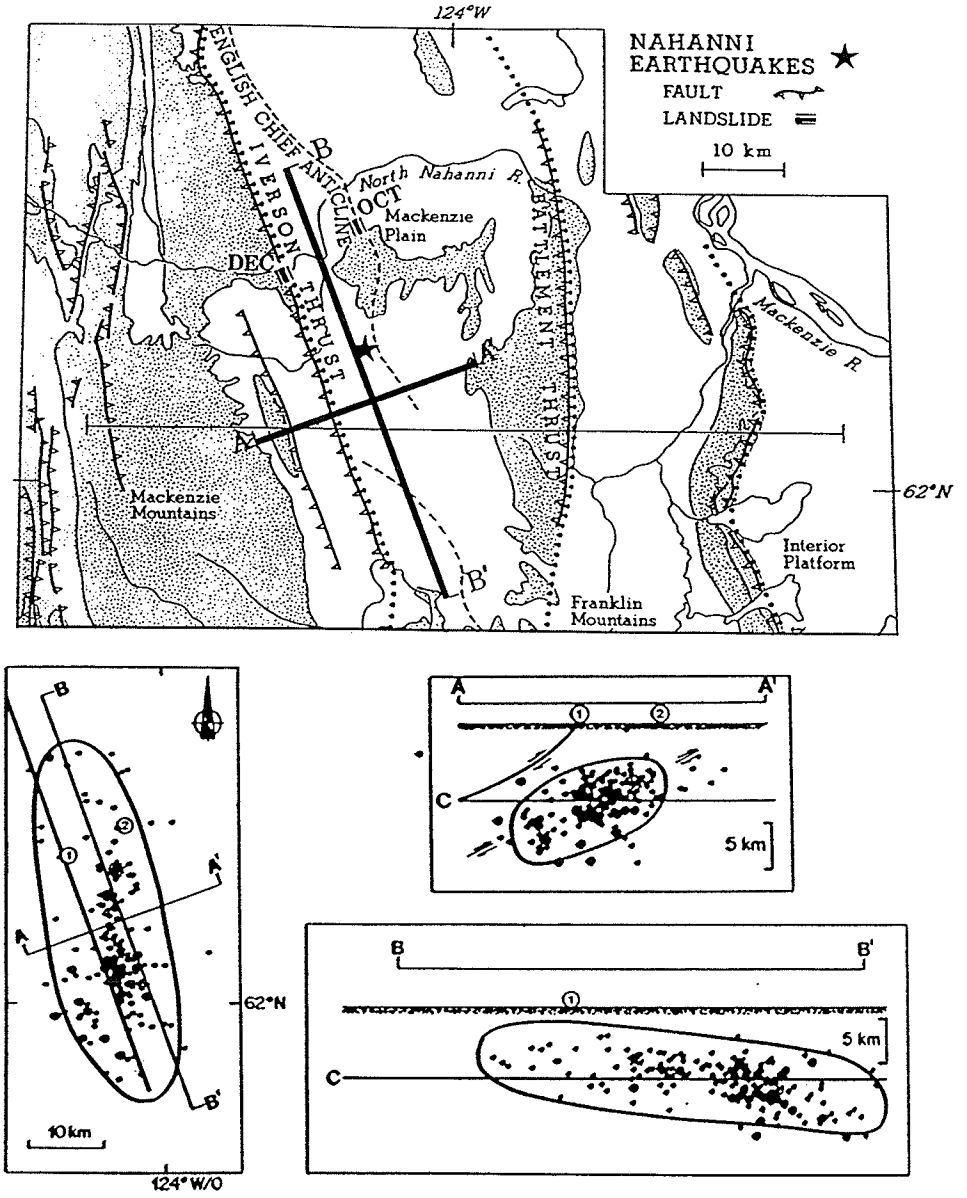

Figure 4.12: Section views of hypocenter distribution. A-A′ crosses the regional geological strike (N160°E), B-B′ goes along with the regional geological strike.

Chapter 5

Remote Sensing Data and Corrections

5.1 Introduction

Remote sensing is the acquisition of information about an object without actual physical contact, specially refers to gathering and processing of information about the earth's environment, its natural and cultural resources through the use of sources installed on aircraft or satellite platform (Simonett, 1983).

The first space image of the earth was transmitted by Explorer-6 in August of 1959. In 1960 the first orbital photography also became available. A series of color photographs were taken by an automatic camera in the unmanned MA-4 (Mercury-Atlas) spacecraft, the pictures demonstrated the value of orbital photographs for viewing the earth's surface. McDivitt and White II conducted the first formal geological photography experiment on the GT-4 (Gemini-Titan)

mission on June 3-7, 1965 (Lowman, 1967). The mission demonstrated that useful data could be acquired for earth-resource analysis.

During the past 20 years geological remote sensing technology has evolved from the simple airphoto interpretation to the integrated digital processing and interpretation stage, from the local level to the regional and global scale, and from the black-and-white aerial photograph to a wide variety and choice of single or sequential color aerial and/or satellite images.

5.2 Geological Remote Sensing

Geological remote sensing refers to processing and analysis of information remotely acquired by various sensors which record signal energy in one or more wavebands of the electromagnetic spectrum. This field mainly deals with the measuring or monitoring various physical and/or chemical characteristics, static or dynamic, of the geological environment of the earth and other planets and their moons of the solar system. Geological remote sensing embraces both optical and digital analysis of images from a vast array of remote sensing devices, mostly passive but some active, from the ultraviolet through the visible, near infrared, thermal infrared, and into microwave wavelengths. Remote sensing technology, as applied to the geological sciences , is a multifaceted tool that, when properly applied to certain types of geological studies, enables geologists to more effectively and accurately carry out various aspects

of scientific and applied investigation.

5.3 Electromagnetic Spectrum and Geology

Figure 5.1 shows various spectral regions which remote sensing systems use to record signal energy, either passive or active, from geological target objects. It can be seen from Figure 5.1 that most regions of the EM spectrum for geological research interests can be recorded by available sensors. In practice, the interested range of EM spectrum varies with each geological investigation. The potential of remote sensing techniques for geological application has been continuously improved as the understanding of the interaction of geological matters and the EM energy increases. Numerous detailed studies of the spectral signatures of minerals, rocks, soils and vegetation in the visible and infrared range have guided the development of geological remote sensing techniques from the panchromatic film cameras of decades ago to the current by new narrow band spectral scanners. Since the main objective of remote sensing application in this study is to extract structural geological information concerning the earthquakes, the focus of this chapter is on spectral response and spatial resolution of the selected remote sensing data sets.

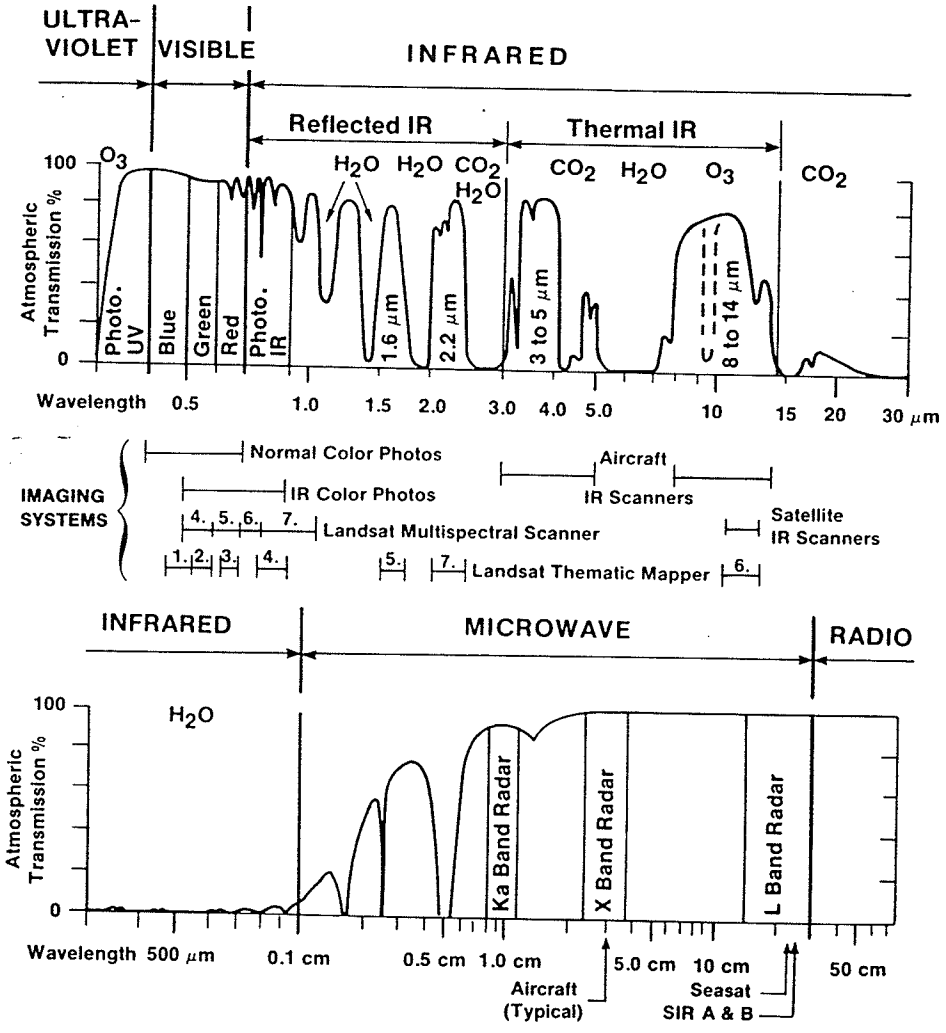

Figure 5.1: The EM spectrum used by remote sensing systems. The upper Figure shows expanded diagrams of the visible and infrared regions and the lower Figure shows the microwave region showing atmospheric windows. (From Sabins, 1987)

5.4 Remote Sensing Techniques for Mapping Structural Geological Features

As discussed in 2.2 and 4.6, the earthquakes in the Nahanni area are likely caused by a certain faulting process occurring at or in the vicinity of epicenters. The possible active faults in the area are certain to be direct or indirect cause. On the other hand, an earthquake represents a sudden release of elastic energy stored in the geological system which has taken a long time to build up. During the geological time, there are many complex tectonic processes which contribute to the accumulation of the elastic energy. Both the short term and the long term geological processes lead to various structural geological phenomena which can be studied by using multi-spectral remote sensing techniques.

From Table 2.1 in Chapter 2, one can see that the types of phenomena which can be dealt with in the earthquake seismology include: structural provinces, mountain belts, basin rift valleys, and small scale faults, folds and lineaments. The corresponding sensor platforms suitable to each of these geological parameters consist of various satellites and aerial images and multi-spectral scanner data.

In this research, three types of remote sensing data sources are used. Each of them is characterized by its spatial resolution and EM spectral window. In

the following, a brief introduction will be given to each type of data sources. Figure 5.2 shows the spatial coverage of each remote sensing mission's data set and epicenter data set over the study area.

5.5 Landsat Data

The Landsat satellite is the first satellite designed specifically to collect images of the earth's surface. The first three of the Landsat series (Landsats 1, 2 and 3) were launched into near-polar circular orbits at an altitude varying between 897 and 918 km. Each of the Landsat series carried a four channel Multispectral Scanner (MSS). The Landsat MSS operated in the spectral range from 0.5 $\mu m \sim 1.1 \mu m$. After 10 years of successful operation, the Landsat-4 and Landsat-5 were launched as a bridge between the old and the new in Earth resources satellite system (Figure 5.3).

Start with the Landsat-4, a new sensor, the thematic mapper (TM) was added as a payload besides the Landsat MSS. The TM is a more advanced scanner, having higher spectral, radiometric, and geometric sensitivity. Because of large increase in data transmission due to improvement in spatial resolution, the Tracking and Data Relay Satellite System (TDRSS) is used to receive sensor data from the Landsat and retransmit them to the ground receiving sites. The platform for Landsat-4 and Landsat-5 is shown in Figure 5.4.

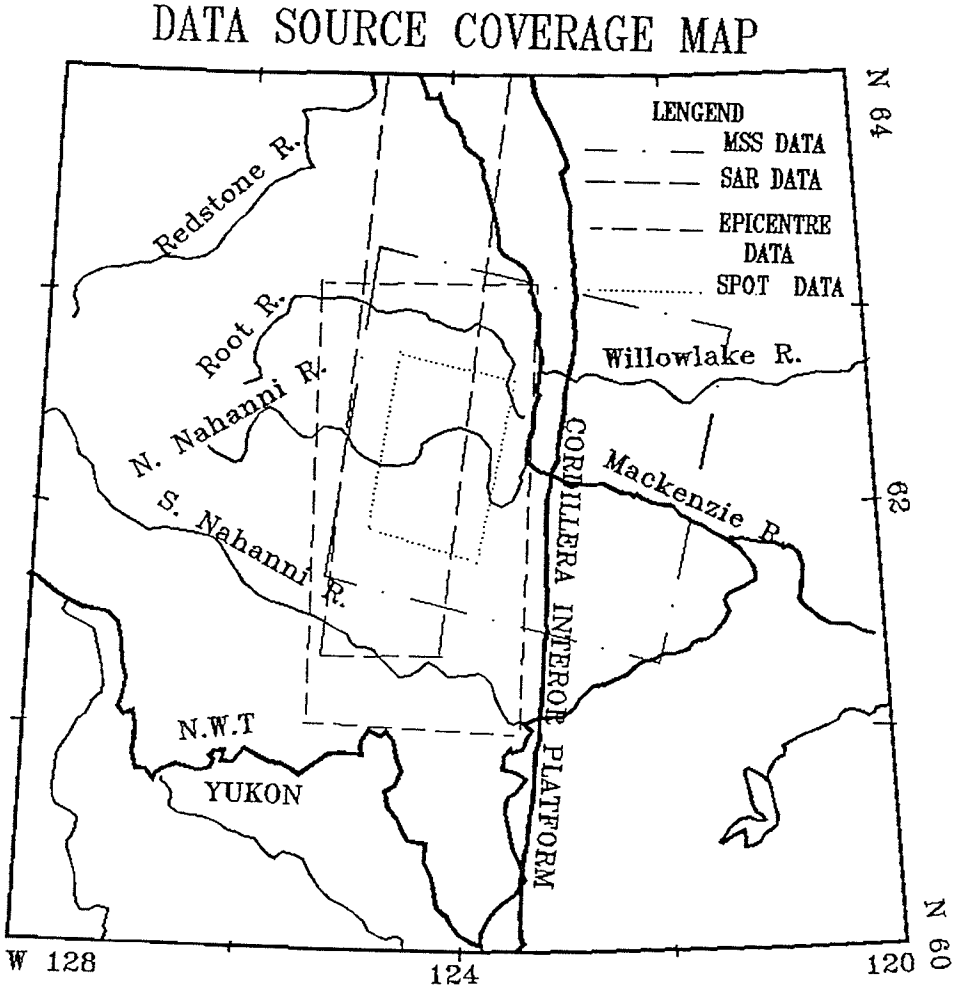

Figure 5.2: Spatial coverage of the data sets over the study area.

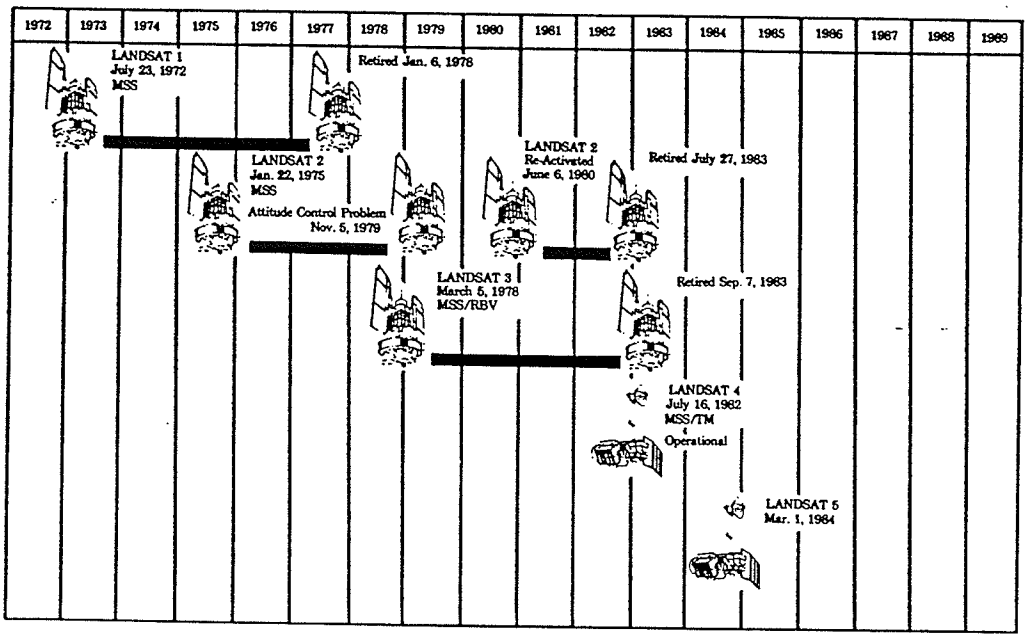

Figure 5.3: Chronological launch and retirement history of the Landsat satellite remote sensing system. (From Jensen, 1986)

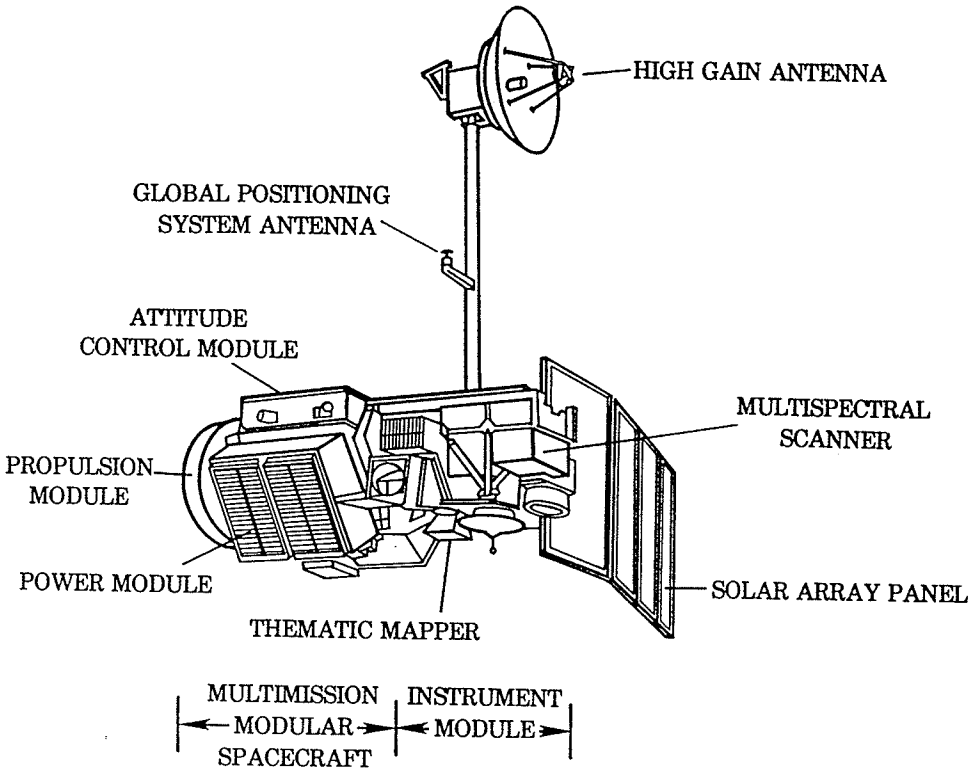

Figure 5.4: Landsat-4 / Landsat-5 satellite platform with associated sensor and telecommunication systems. (From Jensen, 1986)

There were also some changes in orbit parameters. The orbit altitude of Landsat-4/5 decreased from 918 km to 705 km and caused the period between repetitive coverage to change from 18 days to 16 days (Freden and Gordon, Jr., 1983).

Landsat-5 MSS Image Characteristics

Band No.	Wavelength (μm)	Radiometric Sensitivity	Spatial Resolution	Quantization Level
4	0.5~0.6	0.57	82x57(m)	64
5	0.6~0.7	0.57		
6	0.7~0.8	0.65		
7	0.8~1.1	0.70		

Table 5.1: Spatial and pixel parameters of Landsat-5 MSS image data.

To obtain the latest remote sensing information concerning the structural geology in the Nahanni area, MSS data from Landsat-5 were acquired from Canadian Center for Remote Sensing (CCRS). Table 5.2 lists the acquisition parameters.

MSS Data Acquisition Parameters

Satellite	Path/Row	Sun Elevation	Scene Center Time
LANDSAT-5	52/16	32.5441°	1986-09-05::18:49:22
Band No.	**Sun Azimuth**	**Center Lat.**	**Center Lon.**
4,5,6,7	155.3903°	62.264°	-123.367°

Table 5.2: Landsat-5 MSS image data acquisition parameters.

The scene center is close to the epicenter of main shocks ($62.2°N, 124.3°W$), and the whole image consists of 2298 (row) $\times$ 3228 (column) pixels, covering approximately 185 $\times$ 185 km^2 area. The large aerial coverage makes the Landsat-5 data set an ideal image for regional tectonic interpretation. The acquisition time was set in the early autumn, to avoid the both heavy vegetation coverage of summer and extensive snow coverage of winter. The sun elevation angle of 32.54° is fairly low and can enhance the topographic relief of the study area. The sun azimuth angle of 155.39° maximizes the relief effect on the features in the north-east direction.

5.6 SPOT Data

Although the Landsat data provided important regional tectonic information concerning the earthquakes under investigation, the 82 m $\times$ 57 m spatial resolution is too low to allow further investigation on many local structural details such as small folds, faults and fracture zones. On the other hand, the SPOT image has considerably improved spatial resolution. The SPOT (Systéme Pour l'Observation de la Terre) is an earth observation satellite, launched by the France in February, 1986. The SPOT satellite consists of two parts: the SPOT "bus", which contains instruments to maintain orbit control, receive commands, and supply electrical power; and the "payload" which includes earth observation instruments and mission telemetry package (Figure

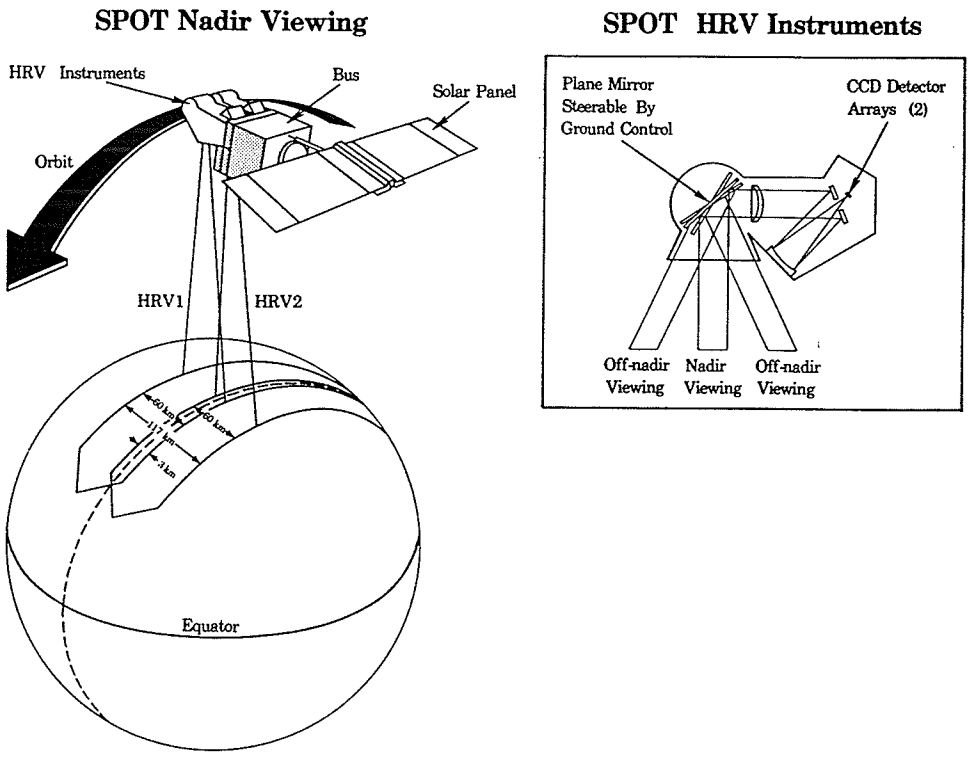

Figure 5.5: Bus and payload of the SPOT satellite.

5.5).

The SPOT-1 space craft carries two nominally identical High Resolution Visible (HRV) optical sensors, which can be operated independently or in various coupled configurations. The HRV instrument works in either of two modes, in the visible and infrared portion of the EM spectrum:

- A panchromatic (black-white) mode corresponding to observation over a broad spectral band, and

- A multispectral (color) mode corresponding to observation in three narrower spectral bands.

SPOT-1 HRV Sensor Characteristics

Band No.	Wavelength (μm)	IFOV	Spatial Resolution	Quantization Level
1	0.50–0.59	4.13°	20x20 (m)	256
2	0.61–0.68			
3	0.79–0.89			

Table 5.3: The SPOT HRV sensor system characteristics and IFOV.

In contrast to the oscillating mirror design used in the Landsat imaging system, the SPOT HRV imaging system obtains image by using Charge-Coupled-Detector (CCD) arrays. This configuration results in straight and continuous sensing lines of 6000 basic sensing elements per line and no geometric distortion due to the movement of an oscillating mirror.

The SPOT maintains a near-polar sun-synchronous orbit at an altitude of about 813 km with an inclination of 98.6°. The orbital cycle is 26 days.

Based on the same reasoning as with the Landsat data, the data acquisition for SPOT was timed to coincide with summer. The Multispectral Mode was chosen based on the following considerations:

- It was reported in the previous study (Wetmilller et al., 1988) that no surface trace of faulting has been found in Nahanni epicentral area.

SPOT Data Acquisition Parameters

Satellite	Path/Row	Sun Elevation	Scene Center Time
SPOT-1	502/22	50.271°	1989-06-11::19:46:58
Band No.	**Sun Azimuth**	**Center Lat.**	**Center Lon.**
1,2,3	169.8009°	62.722°	-123.891°

Table 5.4: The SPOT image data acquisition parameters.

Direct detection of the faulting planes is usually difficult. On the other hand, the recent earthquakes could have altered, in sequence, local geological structure subsurface, ground water table, soil moisture and vegetation distribution of the epicentral area in a subtle manner. The near infrared band ($0.79\mu m \sim 0.89\mu m$) in Multispectral Mode is very sensitive to such changes.

- The near infrared band has high atmospheric transmission qualities, and provides an image with less noise. The Multispectral mode is complimentary with Landsat MSS data, thus effectiveness evaluation can be made on two data sets in a reasonable manner.

The SPOT image is again centered on the two main shocks, covering an approximately 60×60 km^2 area. The sun elevation angle of the SPOT image is considerably higher than that of the Landsat-5 image, which means smaller relief effects on topography. The sun azimuth is nearly north-south. The spatial resolution is much higher than that of Landsat-5 (Table 5.3) at $20 \times$

20 m^2.

There are considerable similarities in the product characteristics between the Landsat and SPOT remote sensing systems. They are both spacecraft based and passive systems. In the following, an aircraft based active remote sensing system – the Synthetic Aperture Radar (SAR) system will be discussed.

5.7 Synthetic Aperture Radar (SAR) Data

SAR is an active microwave or radar imaging system which is fundamentally different from other remote sensing systems discussed so far. One of the advantage of using radar imaging system is that microwave attenuation is negligible as it travels through gases and clouds, and can penetrate into several meters of solids in favorable conditions (Drury, 1987).

The original radar imaging system "illuminates" the earth's surface and it records the backscattered wavefield. In the case of geological application, the look direction is usually downwards, and to a side of the platform. Consequently, the technique is sometimes referred to as Sideways Looking Radar (SLAR) (Moore, 1983). In imaging mode, the antenna illuminates a long, narrow strip perpendicular to the flight direction of the platform (Figure 5.6).

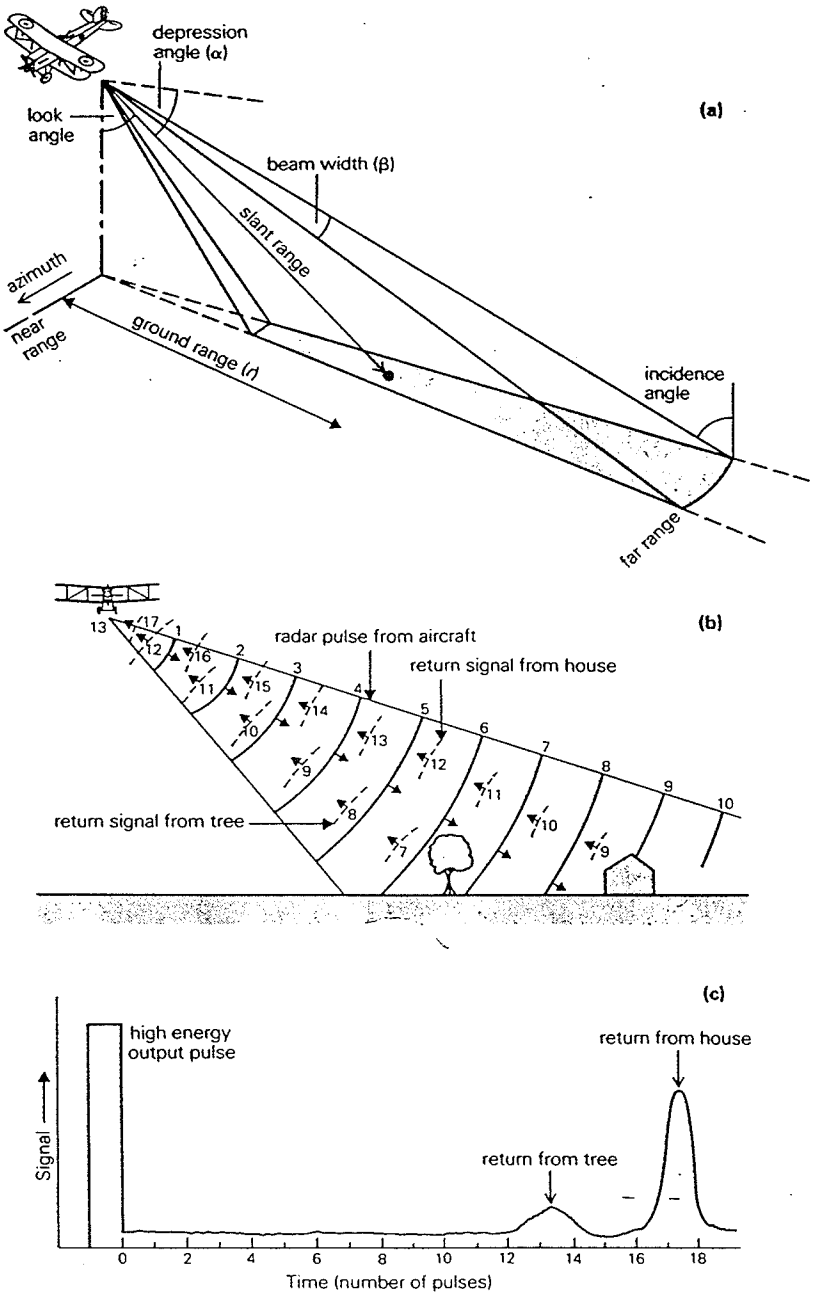

Figure 5.6: Geometry of an airborne Sideways-Looking Radar (SLAR) and schematic plotting of the return signal.

In the Figure 5.6 (a), the schematic geometry of a SLAR governs many of the intrinsic properties of radar imaging. The depression angle α is the angle between the horizontal and a radar path. The look angle is simply the angle between vertical and a ray path $90° - \alpha$. The incidence angle is the angle between an incident radar ray and a line at right angle to the scattering surface. For a horizontal surface, it is the same as the look angle, but varies with the slope of the surface. The beam width (angle β) determines how the illumination of the surface spreads out from near range to far range. The slant range is the direct distance from the antenna to the object; and is related to the true or ground range by the following equation:

$$r = ct \cos \alpha/2 \tag{5.1}$$

where, r is ground range; c is the speed of light and t is the two way travel time of radar signal from the antenna to the object.

In the Figure 5.6 (b), the solid curves are spherical wavefronts emitted by the antenna, and their numbers indicate the time mark since they were emitted. The broken curves are radar wavefronts back-scattered from surface scatters such as the house and the tree. The graph in Figure 5.6(c) shows how radar energy returned from two targets; the house and tree, is recorded at the antenna.

The ground-range resolution R_r and azimuth resolution R_a are controlled

by several factors described as following:

$$\begin{aligned} R_r &= \frac{c\tau_r}{2}\cos\alpha \\ R_a &= \frac{c\tau_r\beta}{2}\cos\alpha \end{aligned} \tag{5.2}$$

where τ_r is the time interval for each radar signal pulse, β is the width of the radar beam expressed by an angle (Figure 5.6). β is directly proportional to the radar wavelength and inversely proportional to the length of the antenna. By shortening τ_r, the ground-range resolution can be increased. But for a chosen radar wavelength, the improvement of azimuth resolution by increasing the length of the antenna is limited for practical reason. This problem has been solved by using Synthetic Aperture Radar (SAR) system. The scheme of a SAR system is shown in Figure 5.7.

In a SAR system interference occurs between a reference signal and the increased or decreased frequencies of radar waves returning from illumination area ahead of and behind the platform. Waves returning from a narrow strip at right angle to the flight path do not undergo a Doppler shift, and no interference occurs. This allows returning signal at any instant from the in-line strip to be discriminated from those from the rest of the illuminated surface, thus high azimuth resolution can be achieved without increasing the antenna length (Drury, 1987).

SAR data for this research were acquired by Canadian Center for Remote

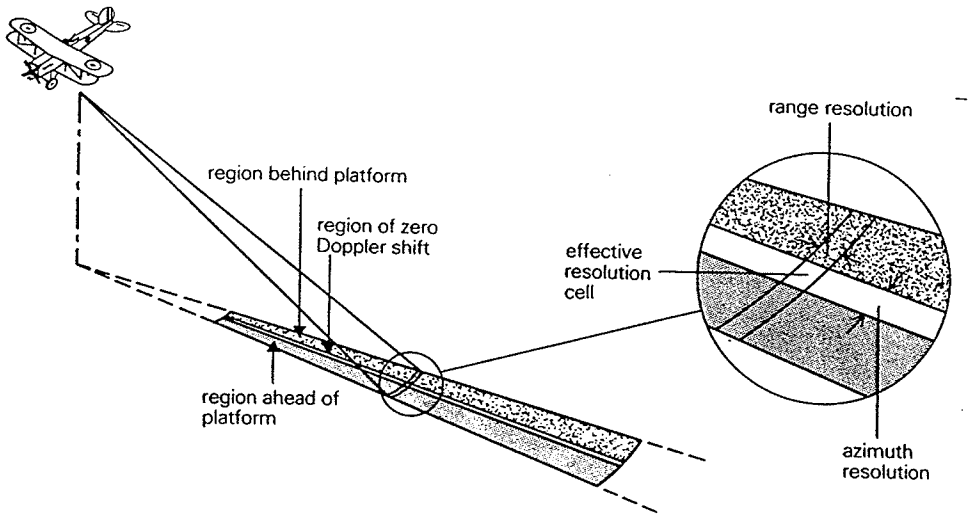

Figure 5.7: The airborne SAR scan geometry.

Sensing (CCRS) as a part of RDDP program. Table 5.5 lists some of the acquisition parameters for this data set. The most important characteristics of the SAR acquisition parameters is its flight direction of 355°, nearly in the north-south direction. On a SAR survey configuration, the radar look direction is perpendicular to the platform flight direction and thus equals to 85°. In an

SAR Data Acquisition Parameters

Flight Date	Initial Lat.	Initial Lon.	Initial Speed	Initial Alti.	Craft Heading
1989-05-09 17:23:19~18:00:05	N61°28.1'	W125°8.2'	509 km	6766 m	355°
Antenna Depress	**Band**	**Polarization**	**Mode**	**Range Resolution**	**Azimuth Resolution**
8.85	C	HH	Wide	20 m	10 m

Table 5.5: CCRS's C-Band SAR data acquisition parameters.

active radar imaging system such as SAR, back-scattered energy returning to the antenna is emitted by the antenna, therefore in a sense, the azimuth angle is 85° for this SAR data set. Usually the surface features perpendicular to the azimuth will be highlighted by illumination effects and the features in the azimuth direction will be suppressed (Simonett and Davis, 1983). This type of azimuth effect phenomena is often ignored when remote sensing images are interpreted. Compared with the azimuth for Landsat and SPOT data (Table 5.2 and 5.4), it can be noticed that the "azimuth" for SAR is almost perpendicular to the that of SPOT data and has an angle of about 65° with that of Landsat data. Such a geometric arrangement allows us an opportunity to study the remote sensing images with varying azimuth angles and to carry out comprehensive analysis of the direction dependent surface structural features. The SAR acquisition time was close to that of the SPOT data acquisition (Table 5.4), and the surface condition in the study area should be comparable. The Horizontal-Horizontal (HH) polarization mode provides maximum energy transfer for the imaging system and is reported to be very effective for routine geological applications.

5.8 Geometric Correction and Registration of Remote Sensing Data

A wide variety of geometric distortions can be introduced into an image by

both the sensor and the nature of the scene which the sensor is viewing. The sensor system consists of the actual radiation or EM-energy sensing mechanism, recording system, transmission, plus the platform on which the system in mounted. In many cases the platform such as a spacecraft and an aircraft, introduces greater geometrical error than the sensor itself (Billingsley, 1983).

5.8.1 Geometric Distortion of Landsat and SPOT Images

In the case of the Landsat MSS system operating on a satellite platform, geometric distortions introduced by the sensor include mirror-sweep irregularities and sampling irregularities. The scanning mirror-sweep irregularities may produce a few hundred meters of geometric distortion. Other sensor related error has more or less the same magnitude. The satellite platform, on the other hand, has position uncertainties (Figure 5.8), mainly in roll, pitch and yaw which produce many hundreds and even thousands of meters of positional distortion in the image.

The CCD (Charge-Coupled-Detector) configuration in SPOT system minimizes the geometric distortion due to sensor by eliminating scanning mirror mechanism, but the distortion caused by the satellite platform still exists and has to be corrected.

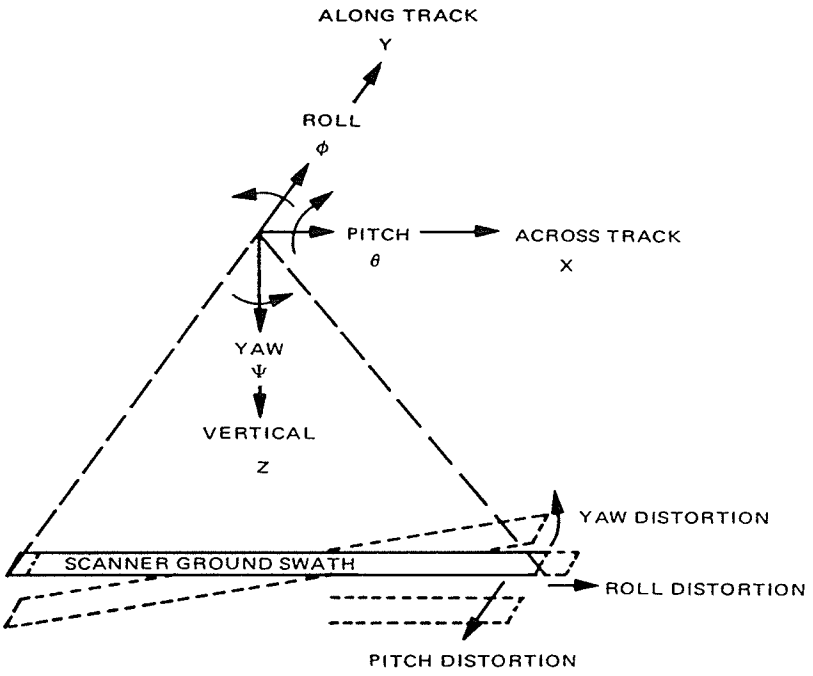

Figure 5.8: Geometric depiction of error source due to platform attitude.

5.8.2 General Procedure for Geometric Correction

In this study, the geological structural interpretation of the remote sensing images will be focused on detection of possible faulting related features, and accurate location and orientation of the geological structural features are essential for this detection. Therefore, geometric correction is very important for all subsequent image processing and interpretation.

In general, the approach of correcting geometric distortion in remote sensing data consists of:

1. Control point determination,
2. Distortion modelling, and
3. Correction processing.

Each of these steps is briefly discussed in the following sub-section.

5.8.3 Control Point Determination

The first basic step of geometric correction processing is determination of control points in the image data to be corrected. The control points in this context, refer to those points which are located both in the distorted image and the reference image/map. Their corresponding geometric relationship determines the spatial mapping relationship between the distorted and the

reference image. The coordinates of control points in the both images are the input to the distortion modelling process by which an image ultimately is corrected. Two categories of reference exist;

- An image reference; and
- A geographic reference.

In the first case, the image is to be corrected to match another image which could be of any shape; and in the second case, precise correspondence is required between the corrected image and the geographic reference system, usually a map.

5.8.4 Geometric Distortion Modelling

Two approaches generally are used to correct geometric distortions in remote sensing data. The first one is to describe the distortion with a general polynomial or other functions not directly related to the causes of the specific distortion. The other approach is to develop mathematical models that characterize the distortion sources and then remove them. The second approach requires a good understanding of the sensor and its platform, and the detailed physical nature of the target scene. These requirements cannot easily be met, especially when a remote sensing system, such as an airborne SAR, involves

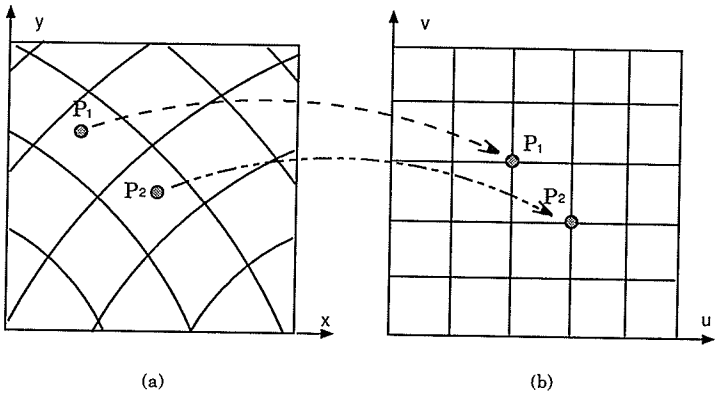

Figure 5.9: The spatial relationship between a distorted image and the reference image. (a). The distorted image. (b). The reference image or the base map.

various sources of uncertainties. In contrast, the first approach is more suitable in many applications because prior information on the remote sensing system itself is not required.

In the polynomial modelling approach, specific distortions contained in an image is unknown and mapping polynomials are fit to control points' coordinates using least square method. This allows us to proceed with the correction directly in the image domain without explicitly questioning the distortion source.

Figure 5.9 shows a schematic relationship between a geometrically distorted and the reference image. Control point P_1 and P_2 are selected and annotated in the both images. Geometric distortion modelling defines the mapping function which maps points such as P_1 and P_2 in the coordinate system (u, v) to

the coordinate system (x, y). In general, this spatial transform is represented by the following simple formula:

$$\begin{aligned} x &= f(u, v) \\ y &= g(u, v) \end{aligned} \tag{5.3}$$

where, $f(u, v)$ and $g(u, v)$ are unknown functions. We assume that $f(u, v)$ and $g(u, v)$ can be approximated by polynomials in u and v of the form:

$$\begin{aligned} f(u, v) &\approx \sum_{j=0}^{p} \sum_{i=0}^{p-j} c_{ij} u^i v^j \\ g(u, v) &\approx \sum_{j=0}^{p} \sum_{i=0}^{p-j} d_{ij} u^i v^j \end{aligned} \tag{5.4}$$

where c_{ij} and d_{ij} are the polynomial coefficients for the term $u^i v^j$ in $f(u, v)$ and $g(u, v)$ respectively. p is the highest order in the polynomials. For the control point pair $\{(x_k, y_k);(u_k, v_k)\}$, Eq(5.4) becomes:

$$\begin{aligned} x_k &\approx \sum_{j=0}^{p} \sum_{i=0}^{p-j} c_{ij} u_k^i v_k^j \\ y_k &\approx \sum_{j=0}^{p} \sum_{i=0}^{p-j} d_{ij} u_k^i v_k^j \quad . \end{aligned} \tag{5.5}$$

The errors between the reference coordinate and those approximated values, E_x and E_y are represented using polynomials, and E_x and E_y can be minimized by a least square method:

$$\begin{aligned} E_x &= \sum_{k=1}^{N} (x_k - \sum_{j=0}^{p} \sum_{i=0}^{p-j} c_{ij} u_k^i v_k^j)^2 \\ E_y &= \sum_{k=1}^{N} (y_k - \sum_{j=0}^{p} \sum_{i=0}^{p-j} d_{ij} u_k^i v_k^j)^2 \end{aligned} \tag{5.6}$$

where, N is the total number of control point pairs. Then, according to the least square theory, the coefficients c_{ij} and d_{ij} satisfy the following conditions:

$$\begin{aligned} \partial E_x/\partial c_{ml} &= 0, \quad 0 \le m \le p, \quad 0 \le l \le p \\ \partial E_y/\partial d_{ml} &= 0, \quad 0 \le m \le p, \quad 0 \le l \le p \quad . \end{aligned} \tag{5.7}$$

We then obtain the following equations:

$$\begin{aligned} \sum_{k=1}^{N} \sum_{j=0}^{p} \sum_{i=0}^{p-j} c_{ij} u_k^{i+m} v_k^{j+l} &= \sum_{k=1}^{N} x_k u_k^m v_k^l \\ \sum_{k=1}^{N} \sum_{j=0}^{p} \sum_{i=0}^{p-j} d_{ij} u_k^{i+m} v_k^{j+l} &= \sum_{k=1}^{N} y_k u_k^m v_k^l \\ 0 \le m \le p; \quad 0 \le \quad l \quad \le p; \qquad m + l \le p \quad . \end{aligned} \tag{5.8}$$

By solving Eq(5.8), the mapping $f(u, v)$ and $g(u, v)$ in Eq(5.4) can be estimated by determining c_{ij} and d_{ij}. For a pixel with a coordinate (u, v) in Figure 5.9 (b), $f(u, v)$ and $g(u, v)$ relate its coordinates in Figure 5.9 (a). Thus, the correct location (u_0, v_0) in the reference image corresponds to (x_0, y_0) in distorted image. However, the coordinates (x_0, y_0) calculated using Eq(5.3) and Eq(5.4) may be not integral. By transferring pixels from each (x, y) to the corrected coordinate (u, v), the geometric distortion is eliminated from the image.

5.8.5 Pixel Value Interpolation

There are three popular approaches for pixel value transfer and they are

briefly explained below.

a. Nearest Neighbor Interpolation

The nearest neighbor interpolation or zero order interpolation is the simplest scheme. In this case, the output pixel value is taken to be that value of the input pixel nearest to the position to which it maps. This method is computationally simple but the resampling can be fairly "coarse" and details in the image are often lost.

b. Bilinear Interpolation

Bilinear interpolation or first-order interpolation is computationally complex. Let $I(x, y)$ be an image function known at the vertices of a unit square (0,0), (0,1), (1,0) and (1,1). Suppose we wish to evaluate the value of $I(x, y)$ at an arbitrary point inside the unit square (Figure 5.10) by using interpolation.

$I(x, y)$ can be interpolated with a bilinear function as follow:

$$\begin{aligned} I(x,y) &= [I(1,0) - I(0,0)]x + [I(0,1) - I(0,0)]y \\ &\quad [I(1,1) + I(0,0) - I(0,1) - I(0,0)]xy + I(0,0) \quad . \end{aligned} \tag{5.9}$$

As shown in Figure 5.10, when the adjacent neighborhood four-pixels are interpolated with the bilinear equation, the resulting surface matches in amplitude at the neighborhood boundaries but the slopes do not necessarily match. Thus a surface generated using a piecewise bilinear interpolation is continuous,

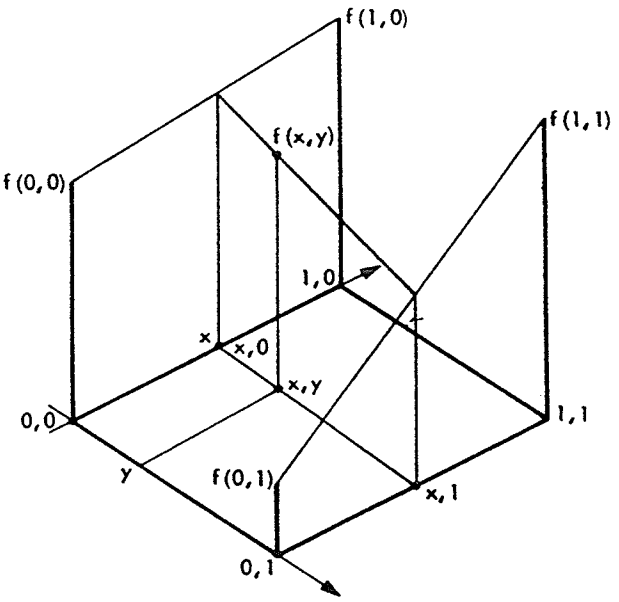

Figure 5.10: A bilinear interpolation scheme for geometric correction.

but its derivatives are not constrained to be continuous at the neighborhood boundaries.

c. Cubic Splines Interpolation

The low-pass effect of the bilinear interpolation may degrade fine details in an image, particularly if magnification is applied. In this case, the extra computational effort of higher order interpolation may be justified. The cubic splines interpolation is often used, in which polynomials up to the third order are used to approximate the image function in each pixel neighborhood. This scheme forces continuity of the derivatives as well as the function values at the neighborhood boundaries.

5.8.6 Geometric Correction

A 1:250,000 topography map with Universal Transverse Mercator (UTM) projection is used as a base map for the geometric correction processing. All the remote sensing images are geometrically corrected and transformed to match the base map. The processing is carried out on the ARIES-II image processing system. The following describes the outline.

Control points were chosen on the base map and also on the Landsat MSS Band 7 image which was judged to be most suitable in term of spatial resolution among the four Landsat MSS bands. To obtain a spatially balanced mapping function, control points were selected over the whole image. Originally, 31 pairs of control points were selected. A third order polynomial was used to approximate the mapping function as described Section 5.8.4. The approximation errors were used as criteria for elimination of "bad" control point pairs. Sixteen control point pairs were eliminated based on this criteria. The statistics of control point pair are listed in Table 5.6.

Although a much smaller average approximation error could have been reached by eliminating more control points, it was judged that a certain number of control points had to be maintained to achieve reasonably balanced mapping.

After the mapping function was determined, image pixels in every Landsat

Control Point Coordinates and Residuals

Point No.	Input Row	Input Column	UTM North Reference	UTM East Reference	Row Residual	Column Residual
1	389	642	6981050	435200	23.0	-270.9
2	643	1456	6946900	473500	-8.0	61.8
3	434	1685	6959250	491200	16.5	68.9
4	95	2602	6969700	549650	-14.0	77.6
5	1028	427	6934850	408100	-40.5	231.5
6	1132	1682	6904750	473500	-12.0	53.5
7	832	1984	6922900	497500	6.5	87.6
8	1029	1765	6911350	480550	3.5	0.3
9	1031	3041	6888850	549600	0.5	-241.9
10	1992	306	6861900	377150	0.0	3.6
11	1818	1336	6857400	437200	47.5	-156.4
12	1624	2360	6854500	497750	-9.0	-54.7
13	2147	1975	6820550	463550	22.0	-79.4
14	2088	2653	6813150	502000	-80.5	140.8
15	1910	3323	6815400	542800	45.5	77.8
Polynomial order= 1		**Standard Error of Row Estimate=** 50.72		**Standard Error of Col. Estimate=** 153.36		
Polynomial order= 2		**Standard Error of Row Estimate=** 28.72		**Standard Error of Col. Estimate=** 124.97		
Polynomial order= 3		**Standard Error of Row Estimate=** 14.34		**Standard Error of Col. Estimate=** 16.16		

Table 5.6: The control point coordinates and residuals for geometric correction of the Landsat MSS image data.

MSS band were resampled by using the cubic splines interpolation. The SPOT and airborne C-SAR images were geometrically corrected using the same base map and the similar approach. The corrected Landsat MSS images have a pixel resolution of 100×100 m^2, meanwhile the corrected SPOT and airborne C-SAR images both have a pixel resolution of 20×20 m^2. The uncorrected, distorted Landsat MSS image is given as an example in Figure 5.11. The same geometrically corrected Landsat MSS image is shown in Figure 7.1 in Chapter

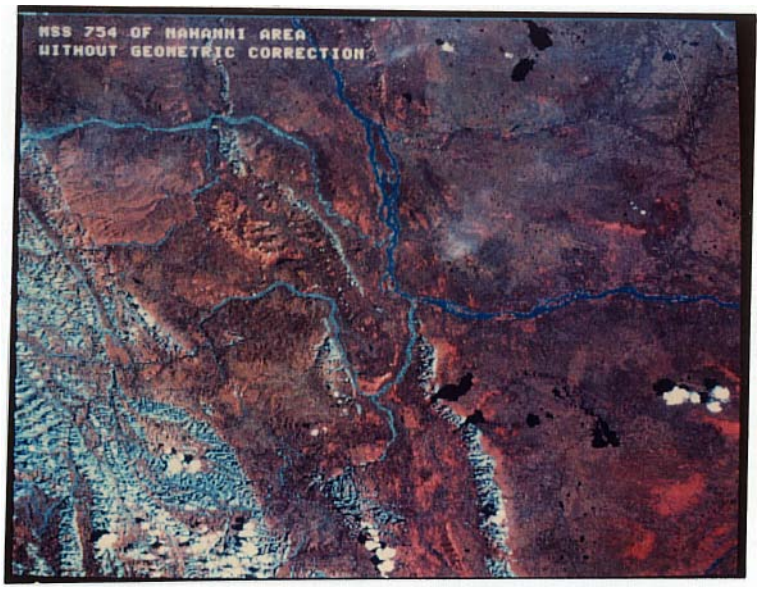

Figure 5.11: The MSS (Bands 7, 5 and 4) composite image before the geometric correction.

7. It can be seen that the corrected image has been rotated approximately 15° which is caused by the inclination of the Landsat orbit. It also can be noticed that there is a considerable amount of geometric correction made by comparing several major features in both images.

Chapter 6

Digital Processing of Remote Sensing Image Data

6.1 Introduction

Digital image processing is a relatively recent development. In its short history, remote sensing has been a major impetus to its rapid development. Because various spacecrafts such as Skylab and Landsat produced a huge volume of digital image data, digital image processing has consequently become the only proper technique to utilize this kind of image. Digital image processing has now become a multidisciplinary field which covers diverse aspects. It is, however, not the intention of this study to review and discuss all of them here. Nevertheless it is necessary to briefly introduce the elements of digital image processing before we discuss image process for this research.

6.2 Elements of Digital Image Processing

Digital image processing first requires a host computer platform upon which major tasks of image processing will be performed. In addition, the system must have specific input/output devices, for example, a tape drive and a display monitor. Since computers work with digital numbers rather than analog pictorial data, image data must first be converted to a digital form before any processing. For this research, all the remote sensing data were received in digital form and delivered on tapes or diskettes.

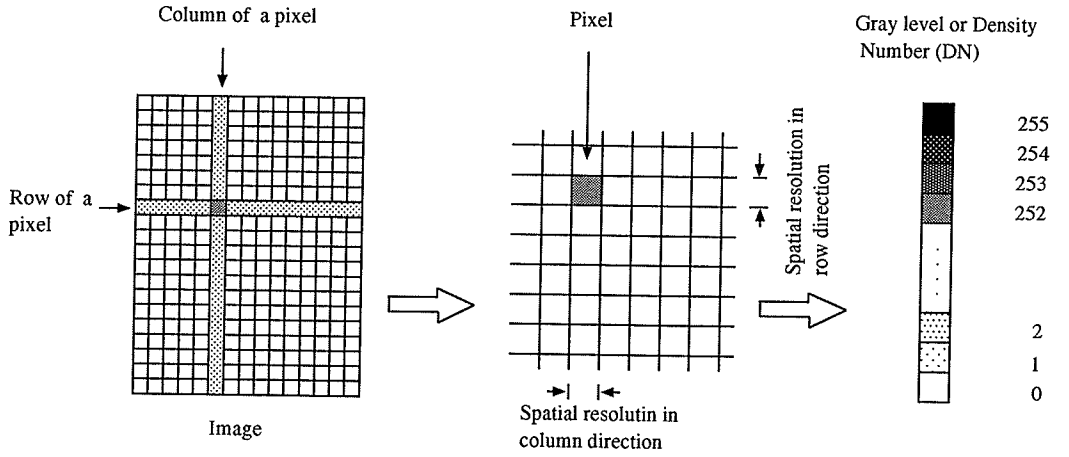

Figure 6.1: An illustration of row, column, pixel and pixel value of image data.

An image in a digital form is illustrated in Figure 6.1. In a digital image, the minimum unit is called picture element, or pixel for short. The location of a pixel is defined by its row number and column number in a rectangular

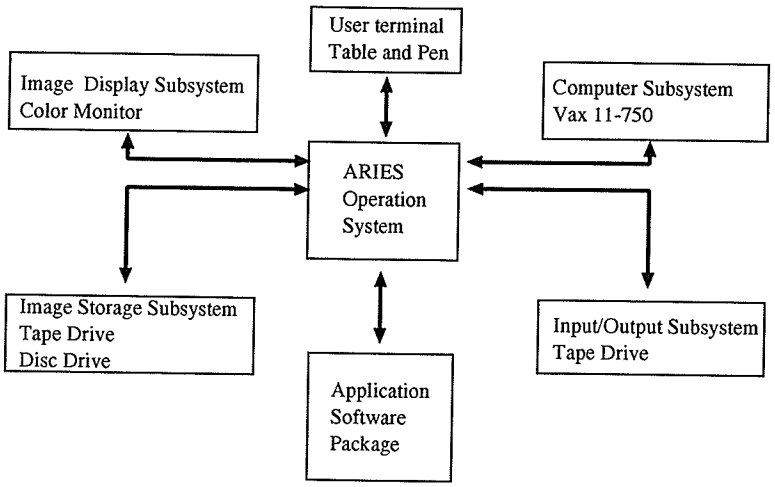

Figure 6.2: A schematic diagram of ARIES image processing system.

subdivision scheme as shown in Figure 6.1. At each of pixel location, a numerical value represents the brightness of the image at that location. This value is called pixel value or DN (density number) which is an integer between $2^0 \sim 2^8 - 1$ in most cases. In optical remote sensing data, a DN corresponds to the EM energy response as measured by a sensor for the given spectral band. Mathematically, it is convenient to consider a digital image as a matrix for digital manipulation.

Figure 6.2 shows a block diagram of the ARIES system which was used in this study. Remote sensing image data sets provided by CCRS are received on 6250 bpi Computer Compatible Tapes (CCTs). The image data were read

in from the tapes through the ARIES system. After image data were read into an image disk, a series of commands was called up and image processing programs were executed. The processed image data were then stored on the image disks or on tapes for later processing or data transfer. Image data are displayed on a color monitor and are manipulated by using a special look-up table and an active pointing pen.

6.3 Image Enhancement

In this thesis, image enhancement refers to those digital image processing procedures which are applied to remote sensing images to improve the appearance of an image for human visual interpretation or for subsequent computer analysis. Usually, not all the original information in a set of original data is maintained after enhancement. Instead some portion or specific features of it will be emphasized while others may be suppressed or eliminated. There is obviously no universal standard approach for an ideal or the best image enhancement because the results are ultimately evaluated by human interpreters who make subjective judgements. Image enhancement is an objective-oriented technique, and only the ones which are considered to be important for this study are discussed below. Let $I(x, y)$ denote an input image and $G(x, y)$ denote the output image. The index numbers (x, y) are the row and column coordinates of the image data. The subscripts of the I and G denote a specific

image spectral band in the case of a multiband image. The image feature enhancement techniques that we used can be divided into three categories:

1. Point operation, which modifies each pixel value independently; i.e.,

$$G(x_0, y_0) = f(I(x_0, y_0)) \quad .$$

2. Local operation, which modifies each pixel value in the context of pixel values of its neighborhood; i.e.,

$$G(x_0, y_0) = f(I(x, y))$$

$$(x, y) \in neighborhood\ of\ (x_0, y_0).$$

3. Multiband operation, which modifies each pixel value in the context of pixel values of corresponding pixel in several image bands; i.e.,

$$G_l(x, y) = f(I_k(x, y))$$

$$k \in [b1, b2]$$

where $[b_1, b_2]$ is the spectral bands and $f(\cdot)$ represents the transform function.

Among the three operations, the point operation is simplest and easy to implement. These three operations are performed on basis of certain statistical attributes of image data. Before we discuss these operations, it is beneficial to briefly review related statistical parameters of digital image data.

6.3.1 Statistics of Digital Image Processing

In the following we assume that all images involved have m rows and n columns. As discussed in the above section, a digital image can be considered as matrix, and we define the following basic parameters:

$$
\begin{aligned}
min_k &= min\{I_k(x,y)\}, \quad 1 \le x \le m, \quad 1 \le y \le n; \\
max_k &= max\{I_k(x,y)\}, \quad 1 \le x \le m, \quad 1 \le y \le n; \\
\mu_k &= \frac{1}{m \times n} \sum_{x=1,m;y=1,n} I_k(x,y); \\
var_k &= \frac{1}{m \times n} \sum_{x=1,m;y=1,n} (I_k(x,y) - \mu_k)^2; \\
std_k &= \sqrt{\frac{1}{m \times n} \sum_{x=1,m;y=1,n} (I_k(x,y) - \mu_k)^2}; \\
cov_{k,j} &= \frac{1}{m \times n} \sum_{x=1,m;y=1,n} (I_k(x,y) - \mu_k)(I_j(x,y) - \mu_j); \\
cof_{k,j} &= \frac{cov_{k,j}}{std_k \times std_j} \quad . \qquad (6.1)
\end{aligned}
$$

The meaning of min_k and max_k are straightforward, μ_k represents the average "brightness" of an image. The std_j and var_k represent the standard deviation and variance of the DN of an digital image. The $cov_{k,j}$ and $cof_{k,j}$ are the cross product and the correlation coefficient between image band $I_k(x,y)$ and $I_j(x,y)$ respectively.

Some statistical parameters for the image data (SPOT Bands 1,2 and 3)

of Nahanni Area are listed in Table 6.1.

Statistics of SPOT Data

Band No.	Correlation Matrix			Mean	Std. Devi.
	1	2	3		
1	1			40.80	6.34
2	0.964	1		25.98	6.17
3	0.121	0.105	1	43.52	7.16

Table 6.1: Mean, standard deviation and correlation statistics of SPOT image (Bands 1,2 and 3) data used in the Nahanni study area.

Table 6.1 shows that three image band have similar standard deviation, but the average DN of Band 2 is much lower than that of the other two bands. Notice the extremely high correlation coefficient value between Band 1 and Band 2 whereas the correlation coefficient value between Band 2 and Band 3 is very low. This is due to the continuation between Band 1 and Band 2, and a gap between Band 2 and Band 3 in wavelength (Table 5.3). Another useful tool in digital image enhancement is the histogram. For a single band image, the tabulating of occurrence frequencies of each DN within the image provides statistical information which may be displayed graphically in a histogram(Castleman, 1979). If one considers DN as a random variable, then the histogram can also be taken as a probability density distribution. Similar conclusion holds when a multiband image is involved. A histogram for the SPOT image (Bands 1,2 and 3) is displayed in Figure 6.3.

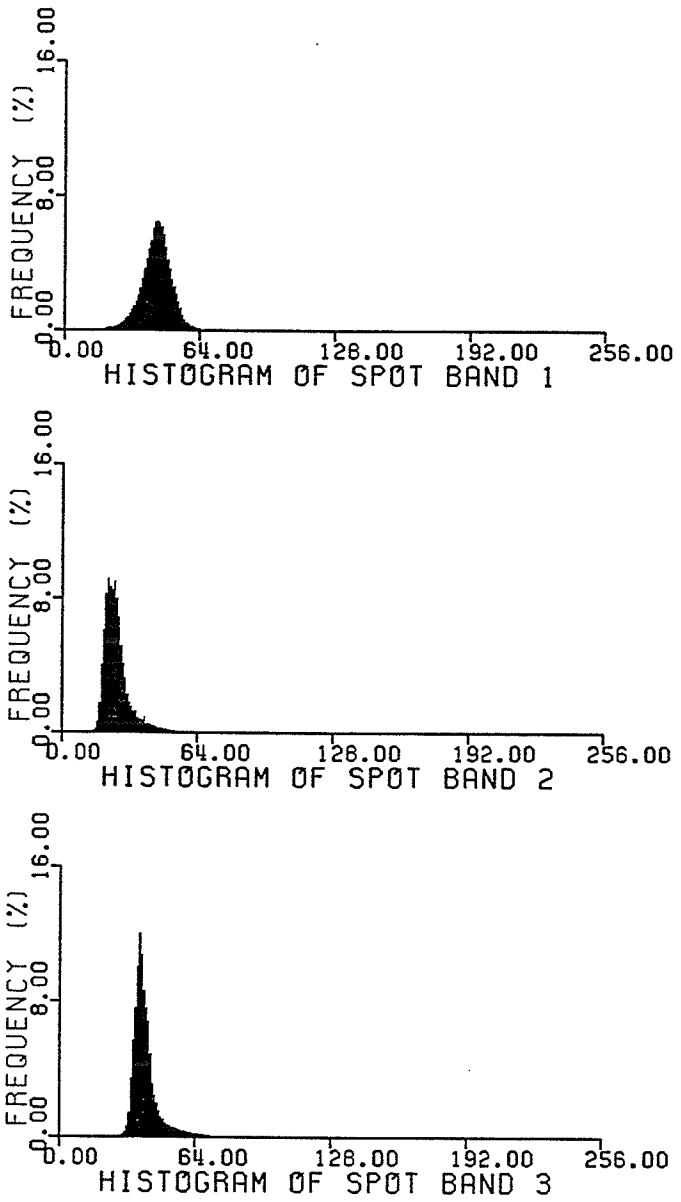

Figure 6.3: The histogram of SPOT image of Bands 1, 2 and 3 in the study area.

6.3.2 Point Operation

In this section, the point operations will be discussed, which change the contrast of an image for better visual interpretation. One can alter each pixel value in an image and thus change the contrast of the concerned information by using a linear or nonlinear transformation:

$$G_k(x,y) = f(I_k(x,y)) \quad .$$

Let us first consider the case that the transform function is linear or piecewise-linear (Hall, 1979).

a. Linear Scaling Transform

A simple but useful model is the linear scaling transform. For most remote sensing images, the dynamic range of DN does not fully fill the available contrast range of the display device. That is, suppose the input image covers a range of $[min, max]$, but the available range for the display device is $[r_1, r_2]$. Then the linear scaling:

$$G(x,y) = \frac{(I(x,y) - min)}{max - min}(r_2 - r_1) + r_1$$
$$[min, max] \subset [r_1, r_2] \tag{6.2}$$

expands the pixel value over the complete available range. Let us assume that the DN of the input image $I(x,y)$ and the output image $G(x,y)$ are continuous random variables represented by w and z with a probability density functions

$p_w(w)$ and $p_z(z)$ respectively. Then, if p_w is known and is zero outside the range $[min, max]$, it is easy to determine the output probability distribution. Since

$$\begin{aligned} P_G(z) &= Prob(G \leq z) \\ &= Prob\{I \leq [\frac{(z - r_1)}{(r_2 - r_1)}](max - min) + min\} \\ &= \begin{cases} 0, & w < min \\ P_I(w), & min < w < max \\ 1, & w > max \end{cases} \end{aligned} \tag{6.3}$$

where P_G is the probability distribution for $G(x, y)$ and P_I is the probability distribution for $I(x, y)$, and the output distribution is of exactly the same form as in the input distribution. This means that distribution will not be changed under a linear scaling (Hall, 1979). It should be pointed out that although Eq(6.2) expands the dynamic range for display, it does not utilize the available contrast efficiently because the pixel value usually have very low occurrence frequencies near the two extreme ends(Figure 6.3). To improve the performance of linear scaling, a clipping procedure is adopted in the processing of this study (Figure 6.4). The clipping procedure can be demonstrated as the following.

Suppose that the transform is linear over a range $[m_1, m_2]$ where m_1 and m_2 are lower and higher bounds for DN transform respectively. If the input distribution is not restricted to this range, and a clipping procedure as shown

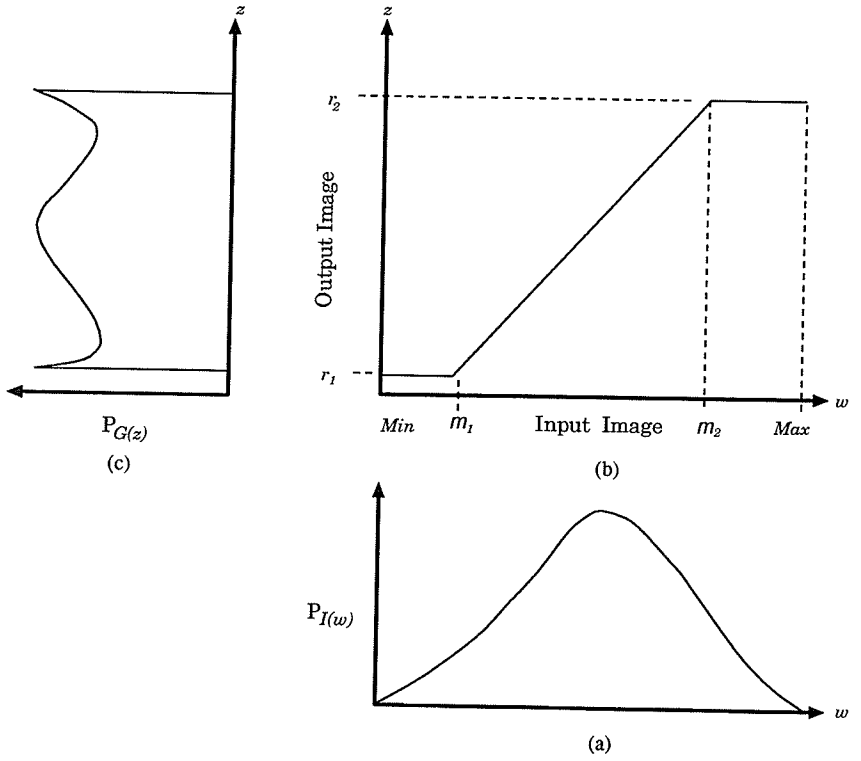

Figure 6.4: (a). The histogram of the input image; (b). The transform function of clipping procedure; (c). The histogram of the output image from clipping procedure.

in Figure 6.4 is used. For this situation, the output distribution is:

$$P_G(z) = \begin{cases} \int_{-\infty}^{m_1} p_w(t)dt, & \text{if } z = r_1; \\ P_I(w), & \text{if } r_1 < z < r_2; \\ \int_{m_2}^{\infty} p_w(t)dt, & \text{if } z = r_2; \end{cases}$$
$$m_1 > Min, \quad m_2 < Max \quad .$$

Thus the output distribution is not identical to the input distribution but has "spikes" at the extreme pixel values.

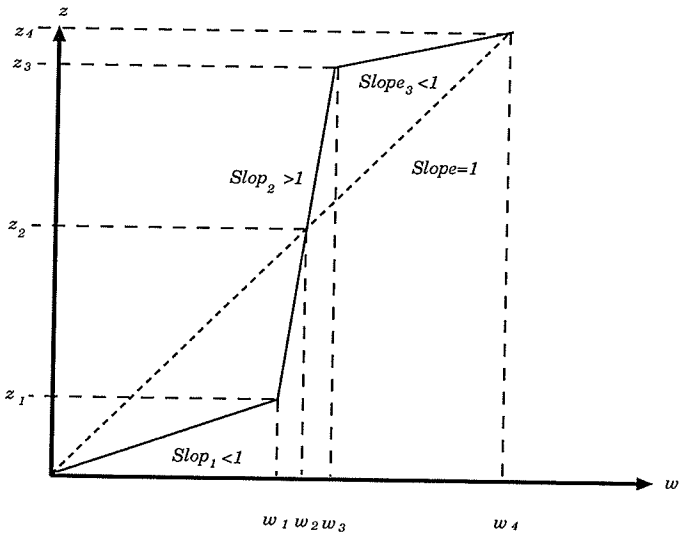

Figure 6.5: Schematic diagram of piecewise linear scaling.

b. Piecewise-Linear Scaling

Piecewise-linear scaling is a variety of linear scaling. Instead of defining one set of parameters for the whole input range, different parameters are defined for different range intervals. An example of a three-interval piecewise linear function is shown in Figure 6.5.

In the each interval, a linear function similar to Eq(6.2) is defined with different values for min, max, r_1 and r_2. In this procedure, if an interval slope is less than unity, the image contrast in the interval is compressed; if the slope is greater than unity, the image contrast is enhanced. In this thesis, the interval division, and interval slopes were determined by observing the histogram of the original image.

c. Logarithmic Transform

Some of the remote sensing data used in this thesis have an approximate log normal distribution, e.g., the SPOT Band 1 (Figure 6.7 (a)). In such cases, a large number of pixels is located in the neighborhood of the lower end of its histogram, and thus the whole image looks dim. One of the improvements that can be made is modification of DN distribution of the original image by using a logarithmic transform. The transform function is given as the following:

$$G(x,y) = gain * \log(I(x,y) + 1) + offset \tag{6.4}$$

where $gain$ and $offset$ are chosen so that $G(x,y)$ utilizes the available dynamic range fully. Plot of this transform is shown in Figure 6.6.

The main advantage of logarithmic transform can be summarized as:

1. It makes the low-contrast details more visible by expanding the low contrast features and suppressing the information in high pixel value,

2. It somewhat matches the response for the human visual system (Hall, 1979), and

3. It transfers a log normal distribution into a normal distribution and multiplicative noise into additive noise.

Figure 6.7 (b) shows the resulting histogram of the SPOT Band 1 after the logarithmic transform.

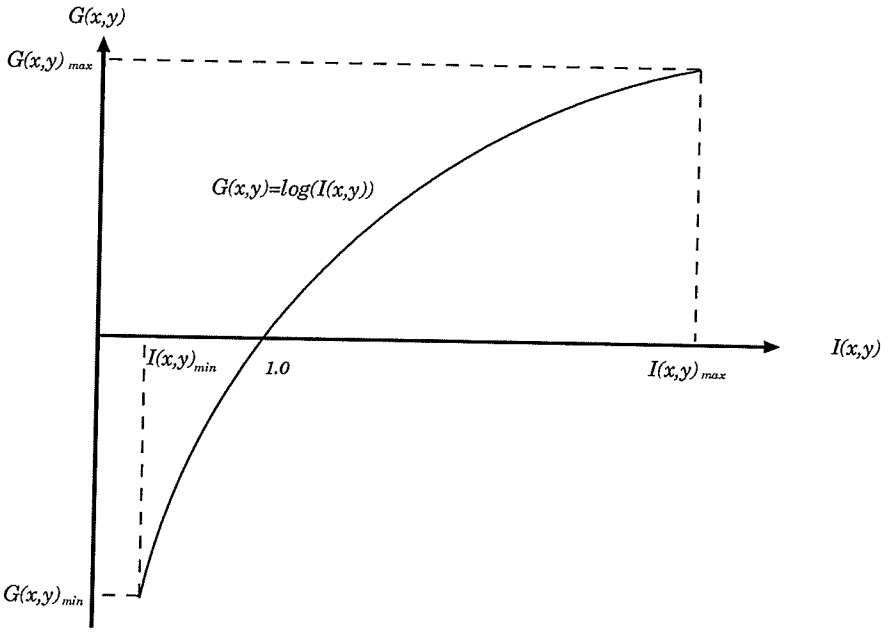

Figure 6.6: Graphic depiction of logarithmic transform.

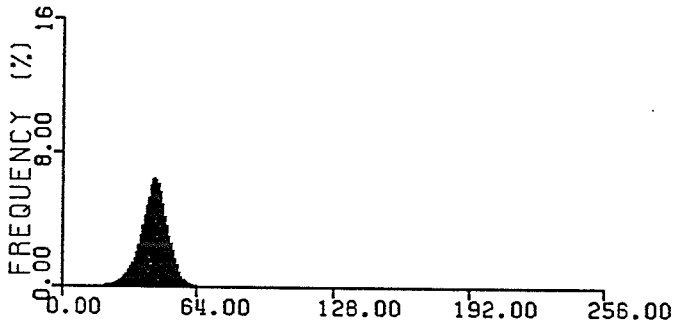

(a)

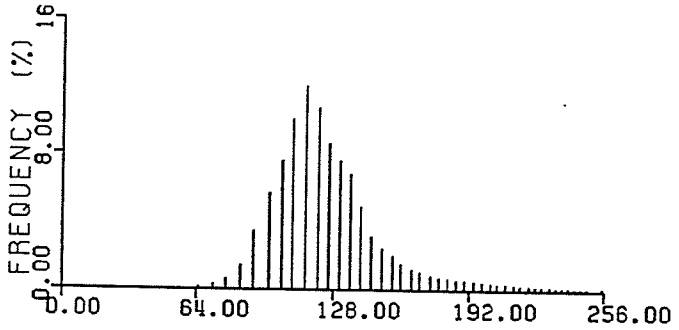

(b)

Figure 6.7: (a). Histogram of the original SPOT Band 1 data; (b). Histogram of the SPOT Band 1 data after the logarithmic transform.

d. Histogram Equalization

Most remote sensing images have a histogram of the DN distribution which is approximately normal distribution (Figure 6.3). If one treats the histogram of image data as a probability density function, then one can see that features with pixel values close to μ have a higher occurrence frequency while features with pixel values near the min and max have much lower occurrence frequencies. In certain cases, however, the features with low occurrence frequency may be of the research interests. These features can be highlighted by increasing their occurrence frequency meanwhile reducing the occurrence frequency of the other features. Histogram equalization is thus a very powerful tool for this type of application (Jensen, 1986).

Based on the above discussion, the desired transform for histogram equalization should have the following properties:

$$\begin{aligned} s &= T(z) \\ p_s(s) &= 1 \end{aligned} \tag{6.5}$$

where T is a unknown monotonic transform with variable of image pixel value z, s is the new variable and is a random variable with a uniform (0,1) distribution. This means that $p_s(s)$ is constant for $s \in (0,1)$. For any point on $T(z)$, say (z_0, s_0), we have:

$$Prob(z \leq z_0) = Prob(s \leq s_0)$$

$$\begin{aligned}
\int_0^{z_0} p_z(z)dz &= \int_0^{s_0} p_s(s)ds|_{s_0=T(z_0)} \\
\frac{d}{dz_0}\{\int_0^{z_0} p_z(z)dz\} &= \frac{d}{ds_0}\{\int_0^{s_0} p_s(s)ds|_{s_0=T(z_0)}\} \\
p_z(z) &= \{\frac{d}{ds_0}\int_0^{s_0} p_s(s)ds\}\frac{ds_0}{dz_0} = p_s(s_0)\frac{dT}{dz_0} \quad . \qquad (6.6)
\end{aligned}$$

Point (z_0, s_0) is arbitrary one, it can be replaced by (z, s):

$$p_z(z) = p_s(s)\frac{dT}{dz} \quad . \qquad (6.7)$$

Substitute $p_s(s)$ with $p_s(s) = 1$ as required in Eq(6.5), one obtains:

$$\begin{aligned}
p_z(z) &= \frac{dT}{dz} \\
T(z) &= \int_0^z p_z(t)dt \quad . \qquad (6.8)
\end{aligned}$$

In Eq(6.8), $p_z(t)$ can be approximated by using the histogram of an image, and the integral is replaced with a summation in numerical calculation (Lehn, 1991). The histograms before and after the histogram equalization of the SPOT Band 3 data are shown in Figure 6.8.

Note that because z is a discrete variable, the resulting histogram is only an approximation of the uniform distribution.

6.3.3 Local Operation

The aim of using local operation is to detect and enhance the features which appear as spatial variation of pixel values. These spatial variations can

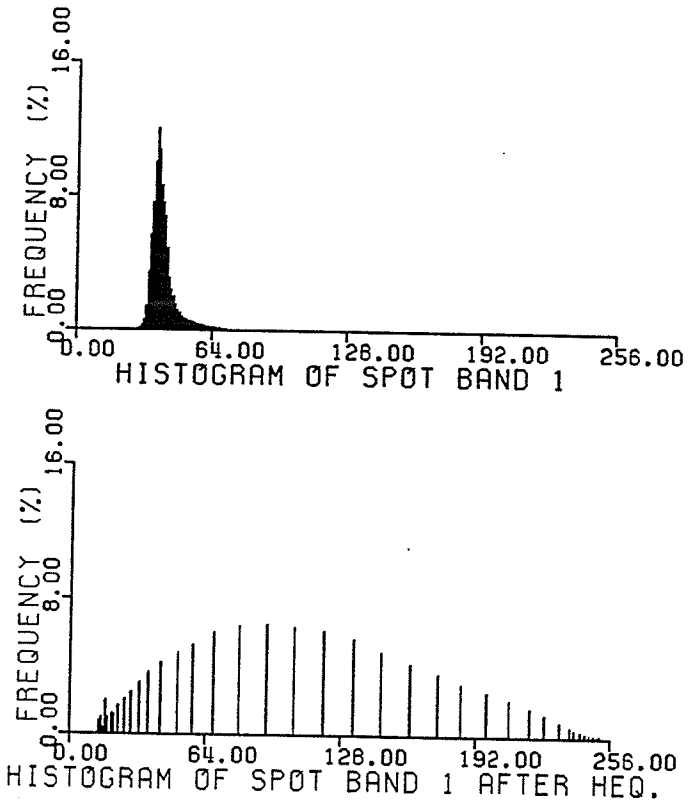

Figure 6.8: Histogram of the SPOT Band 3 data before (top) and after (bottom) the histogram equalization.

be caused by sudden changes in pixel value due to geological structures such as fault lines, rock fractures, soil type change and surface vegetation change, and artificial man-made effects.

In this thesis, the gradient function is the local operation used for detection and enhancement of certain features. We define a gradient function $\nabla I(x,y)$ as:

$$\nabla I(x,y) = \vec{i}\frac{\partial I}{\partial x} + \vec{j}\frac{\partial I}{\partial y} \tag{6.9}$$

where $\vec{i}$ and $\vec{j}$ are unit vectors in the direction of row and column of the image respectively. For a digital image, $\partial I/\partial x$ and $\partial I/\partial y$ are approximated by first differences:

$$\begin{aligned} \frac{\partial I}{\partial x} &\approx \frac{I(x+\Delta x, y) - I(x,y)}{\Delta x} \\ \frac{\partial I}{\partial y} &\approx \frac{I(x, y+\Delta y) - I(x,y)}{\Delta y} \end{aligned} .$$

By setting $\Delta x = \Delta y = 1$, one has:

$$\begin{aligned} \frac{\partial I}{\partial x} &\approx I(x+1,y) - I(x,y) \\ \frac{\partial I}{\partial y} &\approx I(x,y+1) - I(x,y) \end{aligned} . \tag{6.10}$$

In a centered difference formulation, the above equation can be modified as:

$$\begin{aligned} \frac{\partial I}{\partial x} &\approx I(x+1,y) - I(x-1,y) \\ \frac{\partial I}{\partial y} &\approx I(x,y+1) - I(x,y-1) \end{aligned} . \tag{6.11}$$

The partial derivatives $\partial I/\partial x$ and $\partial I/\partial y$ in Eq(6.11) enhance the features along E-W direction and N-S direction respectively because of their responses for the directional image features. In certain cases, where there is no prior information about the direction of the interested features, non-directional spatial enhancement is more useful. In such cases, a second order gradient detector may be used:

$$\nabla^2 I = \frac{\partial^2 I}{\partial x^2} + \frac{\partial^2 I}{\partial y^2} \quad . \tag{6.12}$$

From the mathematical identity:

$$\nabla^2 I = \nabla \cdot \nabla I$$

one has:

$$\begin{aligned} \nabla^2 I(x,y) \approx \quad & I(x+\Delta x, y) + \quad I(x-\Delta x, y) + I(x, y+\Delta y) \\ & + I(x, y-\Delta y) \quad - 4I(x,y) \quad . \end{aligned} \tag{6.13}$$

Local operation of the above Laplacian defined by Eq(6.12) and Eq(6.13) is implemented by convolution operation. In digital image processing, a convolution is defined as:

$$G(x,y) = \sum_{s=-l}^{l} \sum_{t=-m}^{m} K(s,t) \cdot I(x+s, y+t) \tag{6.14}$$

where $K(s,t)$ is matrix called the kernel of the convolution. The corresponding kernels for the above first and second order gradient detectors are listed in Table 6.2.

Convolution Kernels for Gradient Detection

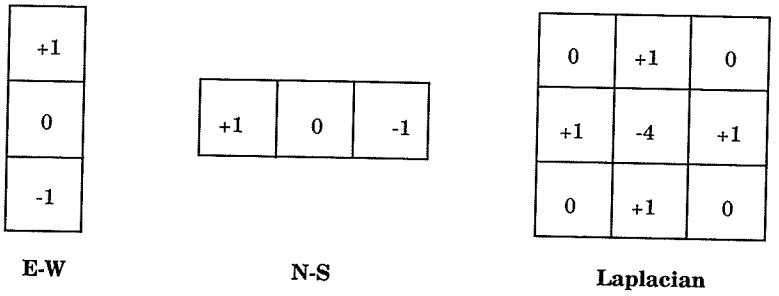

Table 6.2: Convolution kernels for the first and second gradient detectors.

Although the local operation is performed in the spatial domain, corresponding effects in the wave-number domain can easily be shown by:

$$G(x,y) = I(x,y) * K(x,y) \Longleftrightarrow \mathcal{G}(u,v) = \mathcal{I}(u,v) \cdot \mathcal{K}(u,v) \qquad (6.15)$$

where

$$\begin{aligned} \mathcal{G}(x,y) &= \mathcal{F}\{G(x,y)\} \\ \mathcal{K}(x,y) &= \mathcal{F}\{K(x,y)\} \\ \mathcal{I}(x,y) &= \mathcal{F}\{I(x,y)\} \end{aligned}$$

and, $\mathcal{F}\{\cdot\}$ denotes 2-D Fourier Transform. Kernels defined by Eq(6.11) and Eq(6.13) have highpass property in frequency domain, and therefore resulting image $G(x,y)$ will contain enhanced linear and non-linear features or edges.

The spatial enhancement technique discussed above highlights the pixel at whose neighborhood a sudden change in the pixel value takes place. However,

this operation can also lead to a phenomenon where randomly distributed pixels are emphasized even when there are no edges passing by at all. One can use median filtering technique to eliminate such random noise while maintaining enhanced edges. The median filtering operation can be defined as below:

$$\begin{aligned} S &= \{I(x_k, y_k), \cdots / \quad I(x_k, y_k) \leq I(x_{k+1}, y_{k+1}), (x_k, y_k) \in [x_m, y_m]\} \\ G(x, y) &= median\ of\ S \end{aligned} \tag{6.16}$$

where S is a non-descending DN series consisting of k pixels in an image window centered at (x_m, y_m). In a more general case, $G(x, y)$ can take the value of any element in S depending on applications. Such an operation is called the rank filtering (Schalkoff, 1989). The advantage of the median filter used in this thesis is the one that eliminates the isolated non-edge points while keeping the continuous features.

6.3.4 Multiband-image Operation

Some of the remote sensing data sets used in this thesis were obtained in multiple bands. The image signals for the same ground position are separated and stored in separated spectral bands. Each band has its own spectral response range, and is sensitive to certain physical characteristics of ground objects. It can be noticed that there is a considerable information redundancy indicated by the high correlation coefficient value between two adjacent spectral bands (Table 6.1). It is desirable to reduce the information redundancy

meanwhile extracting all useful information from each individual spectral band image. For this study, the useful information includes features such as faults, folds, fractures, rock and soil type changes, vegetation variation and ground water activities. Suppose that a new image can be created using the linear combination of spectral bands of the original image. Then one can write:

$$\mathbf{G} = \mathbf{T}^{\mathrm{T}} \cdot \mathbf{I}$$

where

$$\mathbf{G} = (\mathrm{G_1(x,y)}, \mathrm{G_2(x,y)}, \cdots, \mathrm{G_k(x,y)})^{\mathrm{T}}$$

$$\mathbf{I} = (\mathrm{I_1(x,y)}, \mathrm{I_2(x,y)}, \cdots, \mathrm{I_k(x,y)})^{\mathrm{T}}$$

and,

$$\mathbf{T}^{\mathrm{T}} = \begin{bmatrix} t_{11} & t_{12} & \cdots & t_{1k} \\ t_{21} & t_{22} & \cdots & t_{2k} \\ \cdots & \cdots & \cdots & \cdots \\ t_{k1} & t_{k2} & \cdots & t_{kk} \end{bmatrix} = (\mathrm{T_1}, \mathrm{T_2}, \cdots, \mathrm{T_k}) \quad . \tag{6.17}$$

$\mathbf{T}$ is called transform matrix. Let us treat $\mathbf{G}$ and $\mathbf{I}$ as k dimensional random vectors. To eliminate information redundancy, the new image band $\mathrm{G_l(x,y)}, \mathrm{l} = 1, 2, \cdots, \mathrm{k}$ should be linearly independent to each other. This means that the variance and covariance matrix of $\mathbf{G}$ should be a diagonal one. One can write the variance and covariance matrices of $\mathbf{G}$ in the following form:

$$\begin{aligned} \mathbf{\Sigma} &= \mathrm{E}\{[\mathbf{G} - \mathrm{E}(\mathbf{G})][\mathbf{G} - \mathrm{E}(\mathbf{G})]^{\mathrm{T}}\} \\ &= \mathrm{E}\{[\mathbf{T}^{\mathrm{T}} \cdot \mathbf{I} - \mathrm{E}(\mathbf{T}^{\mathrm{T}} \cdot \mathbf{I})][\mathbf{T}^{\mathrm{T}} \cdot \mathbf{I} - \mathrm{E}(\mathbf{T}^{\mathrm{T}} \cdot \mathbf{I})]^{\mathrm{T}}\} \\ &= \mathrm{E}\{\mathbf{T}^{\mathrm{T}}[\mathbf{I} - \mathrm{E}(\mathbf{I})][\mathbf{I} - \mathrm{E}(\mathbf{I})]^{\mathrm{T}}\mathbf{T}\} \end{aligned}$$

$$
\begin{aligned}
&= \mathbf{T}^{\mathrm{T}}\mathrm{E}\{[\mathbf{I}-\mathrm{E}(\mathbf{I})][\mathbf{I}-\mathrm{E}(\mathbf{I})]^{\mathrm{T}}\}\mathbf{T} \\
&= \mathbf{T}^{\mathrm{T}}\boldsymbol{\Sigma}_{\mathbf{0}}\mathbf{T}
\end{aligned}
\tag{6.18}
$$

where $\boldsymbol{\Sigma}_{\mathbf{0}}$ and $\boldsymbol{\Sigma}$ are the variance and covariance matrices of the random vector $\mathbf{I}$ and $\mathbf{G}$ respectively. E represents mathematical expectation of the random vectors. According to the linear independency criteria, $\boldsymbol{\Sigma}$ should have the the following form:

$$
\boldsymbol{\Sigma} = \begin{bmatrix} \lambda_1 & 0.0 & \cdots & 0.0 \\ 0.0 & \lambda_2 & \cdots & \cdots \\ \cdots & \cdots & \cdots & \cdots \\ 0.0 & 0.0 & \cdots & \lambda_k \end{bmatrix} \quad . \tag{6.19}
$$

The variance and covariance matrices as given in Eq(6.19) then indicates that all the new image bands are linearly independent because the covariances are zeros. The relative significance of each new band in terms of the information content can be evaluated by variance contribution defined by:

$$
\frac{\lambda_i}{\sum_{i=1,k}\lambda_i} \quad . \tag{6.20}
$$

In this thesis the Principal Component Analysis (PCA) was utilized to construct the transform matrix $\mathbf{T}$ under which $\boldsymbol{\Sigma}$ has a form of Eq(6.19). Let $\mathbf{V}_i$ and λ_i denote the ith eigenvector and eigenvalue of $\boldsymbol{\Sigma}_{\mathbf{0}}$, and $|\mathbf{V}_i| = 1$, Then

$$
\boldsymbol{\Sigma}_0\mathbf{V}_i = \lambda_i\mathbf{V}_i \tag{6.21}
$$

and thus

$$
[\quad \mathbf{V}_1, \mathbf{V}_2, \cdots, \mathbf{V}_k]^{\mathrm{T}}\boldsymbol{\Sigma}_0[\mathbf{V}_1, \mathbf{V}_2, \cdots, \mathbf{V}_k]
$$

$$= [\mathbf{V}_1, \mathbf{V}_2, \cdots, \mathbf{V}_k]^{\mathrm{T}}[\lambda_1\mathbf{V}_1, \lambda_2\mathbf{V}_2, \cdots, \lambda_k\mathbf{V}_k]$$
$$= \mathbf{\Sigma} \quad . \tag{6.22}$$

In Eq(6.22) the following property of eigenvectors is used:

$$\mathbf{V}_i \cdot \mathbf{V}_j = \begin{cases} 1 & \text{if i=j} \\ 0 & \text{if i} \neq \text{j} \end{cases} \quad .$$

Now one can construct the transform matrix T as below:

$$\mathbf{T} = [\mathbf{V}_1, \mathbf{V}_2, \cdots, \mathbf{V}_k]$$

thus

$$\mathbf{G} = [\mathbf{V}_1, \mathbf{V}_2, \cdots, \mathbf{V}_k]^{\mathrm{T}}\mathbf{I} \quad . \tag{6.23}$$

A schematic representation of PCA is shown in Figure 6.9.

Consider a 2-D case for simplicity. Suppose that a two-band image (Bands I_1 and I_2) has a joint DN distribution as shown in Figure 6.9 (a) with means, μ_1 and μ_2 respectively. The pattern of the distribution indicates a high linear correlation between the two image bands. A new coordinate system is created by shifting the axes (Figure 6.9 (b)). Then the shifted new coordinate axes are orthogonally rotated about (μ_1, μ_2) by η degree so that the variation of data projection on the new axis PC_1 is maximum while that on PC_2 is minimum. In this case, λ_1 and λ_2 correspond to the axis lengths along PC_1 and PC_2. $\mathbf{V}_1$ and $\mathbf{V}_2$ have the same directions as PC_1 and PC_2 (Jensen, 1986).

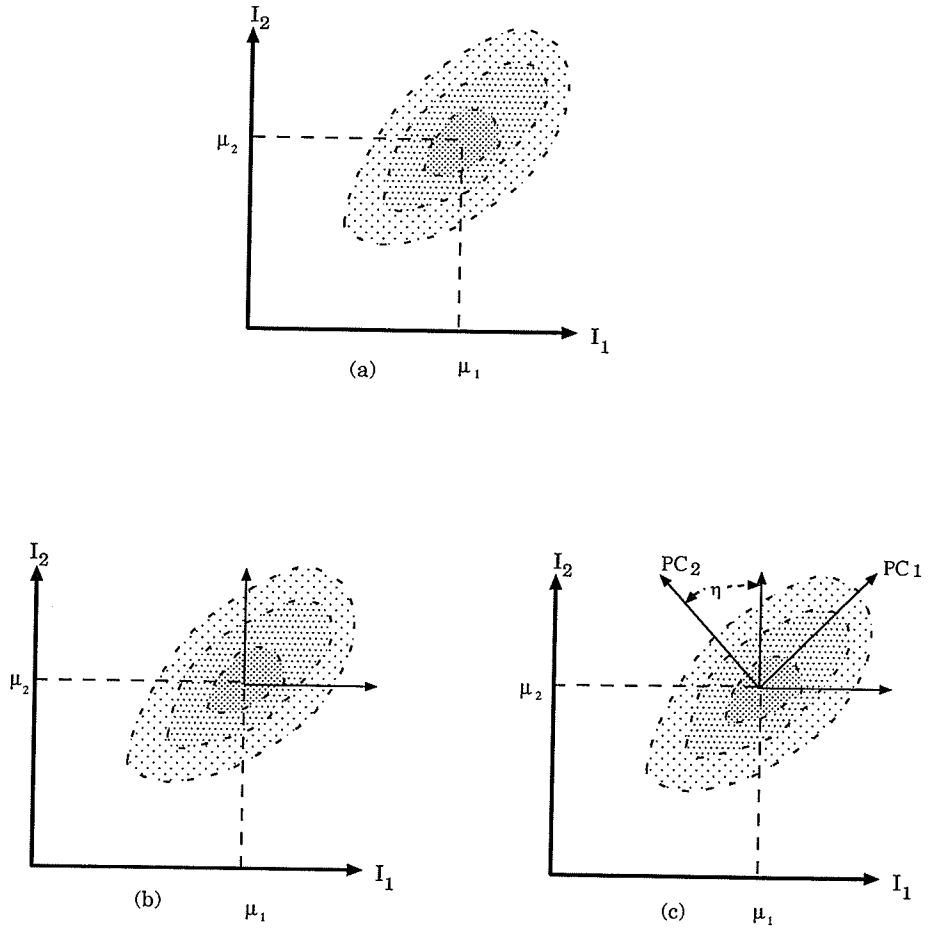

Figure 6.9: Graphic presentation of Principal Component Analysis: (a). A joint distribution of a 2-band image with mean(μ_1, μ_2); (b). A new coordinate system is created by shifting the origin to(μ_1, μ_2); (c). The shifted axes are orthogonally rotated about (μ_1, μ_2) by η degree so that the variation of data projection on axis PC_1 is maximum while on PC_2 is minimum.

Both sets of image data from the Landsat MSS (Bands 7,6,5 and 4) and the SPOT (Bands 1,2 and 3) were processed using PCA. The variance and covariance matrices of these two data sets are listed in Table 6.3.

Variance and Covariance Matrices for MSS and SPOT Data

MSS

Band No.	1	2	3	4
1	211.12			
2	217.31	250.59		
3	230.89	244.43	382.98	
4	207.34	216.43	381.06	397.21

SPOT

Band No.	1	2	3
1	40.220		
2	37.679	38.022	
3	5.507	4.634	51.283

Table 6.3: The variance and covariance matrices for the Landsat MSS image (Bands 7,6,5 and 4) and the SPOT image (Bands 1,2 and 3).

Table 6.4 gives the eigenvalues, eigenvectors and variance contributions of the PCA transform for the Landsat MSS and SPOT data sets. Two new image Bands PC_1 and PC_2 for the Landsat MSS data are shown in Figure 6.10.

An attempt was made to combine both the SPOT and airborne C-SAR data sets using PCA processing. However, the result was not ideal due to the huge difference in illumination conditions in the two data sets.

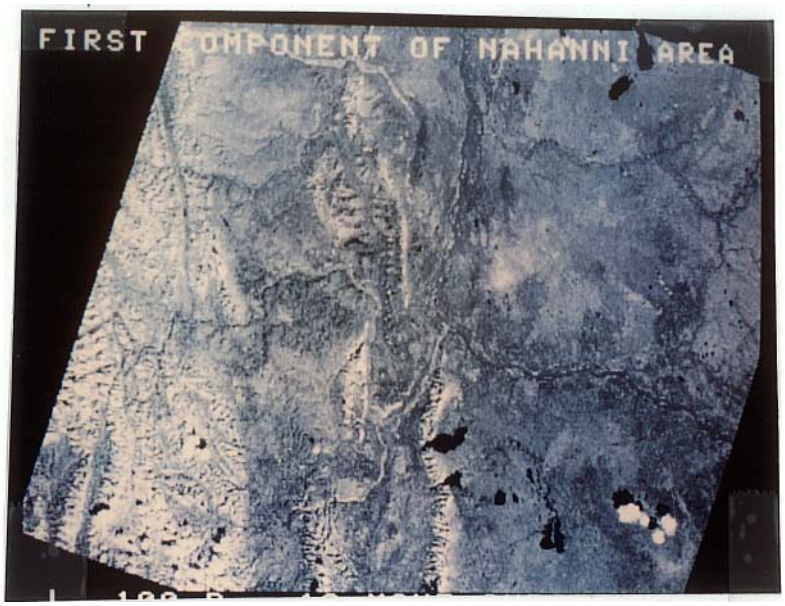

(a)

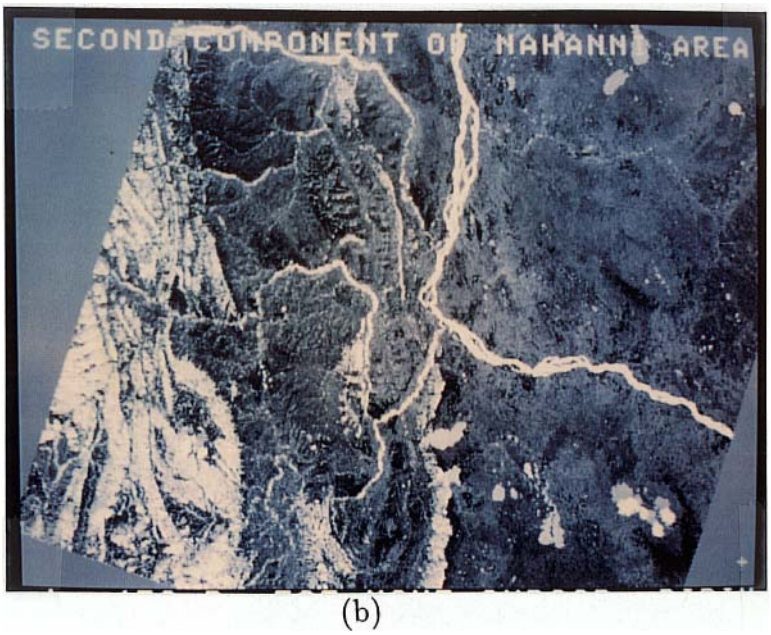

(b)

Figure 6.10: The first two principal components of Landsat MSS image: (a). The first principal component provides the most information in an average sense. There is a high degree of image variations in both mountainous and plain regions. Note that too many detailed small scale features make the significant ones not clear in the mountainous region. The "averaging effect" gives the image a fuzzy appearance. (b). The second principal component shows a more clear picture for the main geological structures in the area. Several groups of NW and NE trending features can be easily seen in the mountainous region. River channels and ranges are highlighted by high contrast. But the overall variation of the image has been reduced.

PCA Results for MSS and SPOT Data

MSS Data

Eigenvector	V_1	V_2	V_3	V_4
	0.393	0.509	0.759	-0.101
	0.421	0.620	-0.650	-0.127
	0.584	-0.264	-0.024	0.767
	0.572	-0.536	-0.02	-0.620
Eigenvalue	1087.8	137.717	12.374	4.004
Variance Contribution	87.592	11.089	0.996	0.332

SPOT Data

Eigenvector	V_1	V_2	V_3
	0.695	0.175	0.697
	0.673	0.184	-0.717
	0.253	-0.907	-0.010
Eigenvalue	78.69	49.40	1.421
Variance Contribution	60.75	38.14	1.097

Table 6.4: The eigenvalues, eigenvectors and variance contributions of PCA transform for the Landsat MSS image (Bands 7,6,5 and 4) and the SPOT image (Bands 1,2 and 3).

6.4 Automatic Linear Feature Detection and Mapping

In the previous section, it was explained how enhancement can be achieved by using image processing techniques and its impact on visual interpretation. So far, most interpretation of the remote sensing data in the geological remote sensing is performed visually by remote sensing experts based on their experiences, knowledge and understanding of specific tasks. The criteria used in visual interpretation are unavoidably subjective and vary from person to person. Image data sets are usually large, detailed visual interpretation of them requires a considerable amount of effort. Results of a visual interpretation are generally in a graphic form and often are not ready for integration with other

digital data.

Automatic linear feature detection and mapping experiments reviewed and carried out in this thesis represent an attempt to overcome or reduce the above problems. In the following, basic concepts of geological remote sensing are introduced and principles and techniques used for automatic linear feature detection and mapping are discussed.

6.4.1 Definition and Significance of Linear Feature

Although there was no easy way of observing the earth surface on a large scale until the very recent space age, William H. Hobbs (1904), an American geologist, recognized existence and significance of linear geomorphic features which might be surface expression of zones of geological weakness or structural displacement in the earth's crust. Hobbs (1912) defined *linear features* as:

> *the significant lines of landscape which reveal the hidden architecture of the rock basement, ···. They are character lines of the earth's physiognomy.*

Clearly the lineament, in his definition, has explicit structural geological meaning. The linear features we refer in this thesis, are probably due to their special contrast differences, appearances and spatial arrangement without necessarily structural geological implications. Instead of using the term

"lineament", a more general term "linear feature" is preferred in this thesis. A *linear feature* on a remote sensing image may be defined as the follow:

> *A linear feature is a mapable simple or composite feature whose parts align in a straight or slightly curving relationship and that differs distinctly from the patterns of adjacent features or background.*

The linear feature may be geomorphic (caused by surface relief) or tonal (caused by contrast differences in brightness or in color). They may represent landforms, the linear boundaries between different types of terrain or breaks within a uniform terrain. Straight stream valleys and aligned segments of valleys are typical geomorphic expressions of linear features. A tonal linear feature may occur as a straight boundary between areas of contrasting color or brightness tone or as a stripe against background of contrasting tone. Differences in vegetation, moisture content, and soil or rock composition account for most tonal contrasts. Linear features may be continuous or discontinuous. An uninterrupted linear fault line is an example of a continuous linear feature. In discontinuous linear features the separated features align in a consistent direction and are relatively closely spaced. Linear features may be simple or composite. A simple linear feature consists of a single type of feature, such as a linear stream valley or a series of aligned depresses. Composite linear features consist of more than one type of feature, such as a combination of

aligned tonal features, stream segments, and ridges (Sabins Jr., 1987).

6.4.2 Preprocessing prior to Automatic Linear Feature Detection and Mapping

Many linear features in remote sensing images are subtle and obscured by background image features. Most image data should be enhanced before any linear feature detection processing. The preprocessing steps applied in this research include the following:

1. Extraction of the useful information from individual original image band data. Then compress it into a new image component using PCA;
2. Enhancement of linear features in the new image component using spatial filtering, i.e., the first order and the second order gradient detection and median filtering; and
3. Conversion of the enhanced image into a binary edge image by thresholding.

In the new image components of PCA, significance of information is in the same order as the component number (Table 6.4) or as the eigenvalue. Therefore, the first component contains most information. When one is interested in the information which is geologically meaningful, the second or the third component can be interpreted with more significance for the study purpose.

In the PC_1 and PC_2 images in Figure 6.10, it can be seen that PC_2 shows a stronger contrast for major linear features such as rivers channels, valleys and ridges. The similar conclusion can be made for the SPOT image data. Thus, only the second component of PCA was used for the further processing in this research. The processing procedures for the Landsat MSS and SPOT data in step 2 are different.

For the Landsat MSS image, the directional gradient detectors were used in linear feature enhancement. If one considers a linear feature as a 2-D vector with an arbitrary direction, it can be decomposed into two vectors in N-S and E-W directions respectively. Thus, they can be detected by N-S and E-W gradient detectors as listed in Table 6.2. As pointed out in the previous section (5.5), the Landsat MSS data set has a sun elevation angle as low as 32.54°, so that the sun azimuth angle has a significant influence on linear features in the images. Linear features perpendicular to the sun azimuth angle will be emphasized while the linear features parallel with the azimuth angle will be suppressed. In this experiment, a compensation for the "sun azimuth effects" was made by using an appropriate kernel during the convolution processing. The final enhanced image was obtained by adding the E-W and N-S enhanced image, and the compensated image together.

For the SPOT image, its sun azimuth effects were considered to be less serious because of its much higher sun elevation angle of 50°. No compensation

processing was carried out in this case. The linear feature enhanced image was obtained by convolution with a Laplacian filter.

To reduce high frequency random noise, a median filtering was applied to both the Landsat MSS and the SPOT images before the linear feature enhancement processing.

The enhanced images were then processed by thresholding and converted to a binary image or an edge image. This procedure is defined as below:

$$G(x,y) = \begin{cases} 1 & \text{if} \quad I(x,y) \leq t_1 \ or \ \ I(x,y) \geq t_2, \ \ \int_{t_1}^{t_2} p_z(z)dz = t_0 \\ 0 & \text{otherwise} \end{cases} \tag{6.24}$$

where t_0 is the percentage of edge pixels in the output image, and t_1 and t_2 are the bounds for thresholding. From the discussion in Section (6.3.3), it is clearly that a linear feature is most likely located where a gradient with large magnitude is yielded. The DN of these locations fall near the extremes in the histogram of the image after a linear scaling. In this thresholding procedure, a combined image viewing and histogram observation method was used to determine the optimum values of the parameters t_0, t_1, and t_2.

On the ARIES image processing system, the thresholding procedure can be carried out by using Piecewise Linear Scaling (PLS). It should be pointed out that although the thresholding makes the further processing much easier, a considerable amount of information is lost during the operation.

6.4.3 Hough Transform and Its Application in Linear Feature Detection

The Hough Transform or HT was first introduced as a method of detecting complex patterns of point in binary image data (Hough, 1962). This is achieved by determining specific parameter values which characterize the patterns we are interested in. In a HT, spatially extended patterns are transformed so that they produce compact features in a space of parameter values. The HT converts a difficult global detection problem in an image space into a local peak detection problem in a parameter space.

The principle of the method can be illustrated by considering a set of collinear points in an image (Illingworth and Kittler, 1988). A set of image points with their coordinates (x, y) that lie on a straight line can be defined by a relation, f, such that:

$$f((\hat{m}, \hat{c}), (x, y)) = y - \hat{m}x - \hat{c} = 0 \tag{6.25}$$

where $\hat{m}$ and $\hat{c}$ are two parameters, the slope and the intercept, which characterize the line. Eq(6.25) maps each value of the parameter combination $(\hat{m}, \hat{c})$ to a set of image points. The hat symbol is used to denote quantities in the domain of the mapping. The mapping is one to many and is from the space of possible parameter values to the space of image points. On the other hand, Eq(6.25) can be viewed as a mutual constraint between image points and pa-

rameter points. Therefore it can be interpreted as definition of a one to many mapping from an image point to a set of possible parameter values. This corresponds to calculating the parameters of all straight lines which belong to the set that passes through a given image point $(\hat{x}, \hat{y})$. This operation is a kind of backprojection of image points. The relationship may be written as:

$$h((\hat{x}, \hat{y}), (m, c)) = \hat{y} - \hat{x}m - c = 0 \quad . \tag{6.26}$$

Figure 6.11 (a) shows a typical point image space. Figure 6.11 (b) shows the parameter lines produced by backprojecting image points into parameter space using Eq(6.26). Figure 6.11 (c) shows a two dimensional accumulation array corresponding to the parameter space (m, c). Points which are collinear in image space all intersect at a common point in parameter space and the coordinates of this parameter point characterizes the straight line connecting the image points. The HT identifies these points of intersection in the parameter space. Determination of the point of intersection in the parameter space is a local procedure. It is considerably easier than detecting extended point patterns in the whole image space.

A more useful form of HT was suggested by Duda and Hart (1972). They proposed that a straight line could be most appropriately parameterized by length, ρ and orientation, θ, of the normal vector to the line from the origin of the image space:

$$\rho = x\cos(\theta) + y\sin(\theta) \quad . \tag{6.27}$$

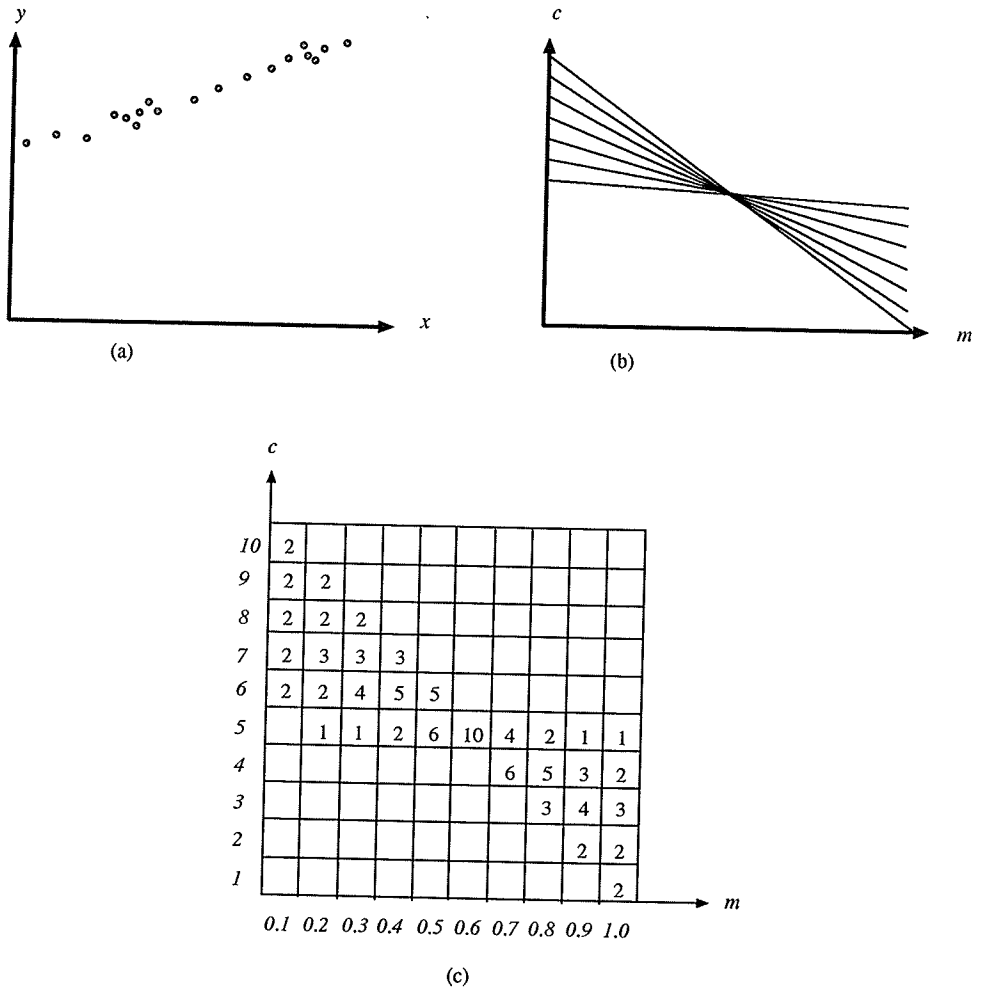

Figure 6.11: Illustration of the Hough Transform process: (a). Point image space (x,y); (b). Parameter space (m,c); (c). Accumulator space corresponding to (b).

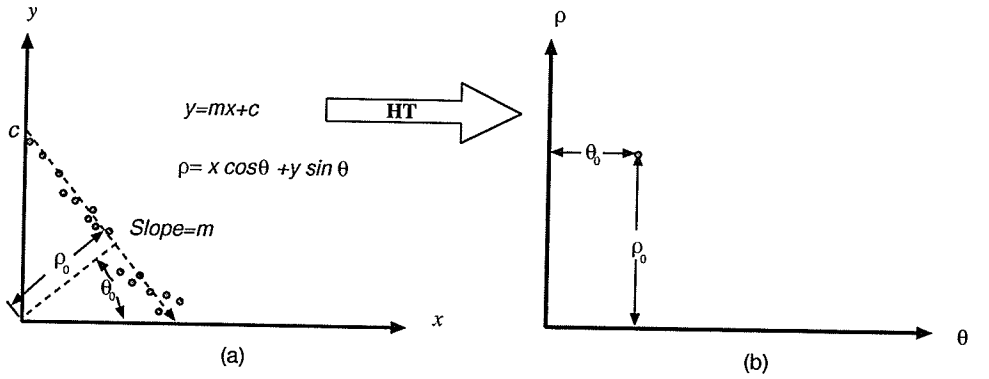

Figure 6.12: The illustration of the modified Hough Transform concept: (a). Defining a straight line using length ρ and orientation θ; (b). A straight line in the parameter space (ρ,θ).

Figure 6.12 shows the modified definition for the Hough Transform. Eq(6.27) has distinct advantage over the (m, c) parameterization which has a singularity for lines with large slopes, i.e., $m \rightarrow \infty$. The length and orientation parameter pair (ρ, θ) represents that image points map into sinusoidal curves in the two-parameter space.

The Hough Transform has been widely used in machine vision research (Illingworth and Kittler, 1988), where the objects to detect are mostly man-made with more or less homogeneous background. In the field of remote sensing image processing, the application of HT is more challenging. Skingley and Rye (1987) have reported an application of the HT for detection of faint lines in SAR images. A more recent example of this kind was conducted by Wang and Howarth (1989). They processed a TM Band 4 image measuring

approximately 15 km× 15 km. Their result has shown that lineaments of up to 70 % depicted on the geological map can be detected by using HT.

6.4.4 Localized HT and Its Implementation

In automatic detection of linear features, the interesting information in an image is first extracted using PCA. A proper image component of PCA is then selected for linear feature enhancement processing. The thresholding procedure is applied to convert the enhanced image component into a binary image. In a binary image, only the pixels which constitute edge features have non-zero value. A binary image is also called edge image due to its appearance.

From the discussion in Section (6.4.3), it is clear now that one can determine existence, orientation and intercept characteristics of linear features by detecting the accumulating peaks in parameter space (ρ, θ). However, for mapping purposes, one still has to determine the starting and ending locations of linear features. A localized HT procedure has been developed to solve this problem.

a. Two level detecting scheme

The linear feature detection processing is carried out at two levels: the local level (window level) and the global level (image level). In this scheme, the target image (m (row) $\times$ n (column)) is divided into several subareas or image windows. The window size is decided experimentally according to the required

accuracy and efficiency. To eliminate any gap between adjacent windows, a limited overlap is allowed along both the row and column directions.

At the window level, the HT based on Eq(6.27) is performed with a minor modification where the origin of the coordinate is shifted to the up-left corner of the window to simplify the calculation. When HT is completed at the window level, all the coordinates of accumulating points in parameter space (ρ, θ) are converted back to global ones. Then, sorting, clustering and merging processing take place in the (ρ, θ) space. Finally, a linear feature table consisting of the orientation, location and other auxiliary information is produced. A digital image containing linear features is then generated by backprojection from parameter space.

b. Localized HT at window level

Within each image window, the row and column coordinates of the edge points are shifted as the follow:

$$\begin{aligned} x^* &= x - x_0 \\ y^* &= y - y_0 \end{aligned} \tag{6.28}$$

where x_0 and y_0 are the up-left corner of the window in the global coordinate. The following algorithm is applied for each edge point:

$$\begin{aligned} Do\ \ 100\ \ \theta &= 0.0, \pi, \Delta\theta \\ \rho &= x^* \cos(\theta) + y^* \sin(\theta) \end{aligned}$$

$$100\ A(\theta,\rho) \;=\; A(\theta,\rho)+1 \quad . \tag{6.29}$$

For each edge point (x,y) which satisfies:

$$\rho_0 = x^* \cos(\theta_0) + y^* \sin(\theta_0) \quad , \tag{6.30}$$

it will have a vote to the accumulator array element $\mathrm{A}(\theta_0,\rho_0)$. On the other hand, for a specific point in parameter space (θ,ρ), all the (x,y) coordinates of edge points which satisfy Eq(6.30) are processed using the following formula:

$$\begin{aligned} x_c &= \sum_{x\in window} x, \\ y_c &= \sum_{y\in window} y, \\ x_d &= \sum_{x\in window} x^2, \\ y_d &= \sum_{y\in window} y^2 \end{aligned} \tag{6.31}$$

where (x_c,y_c) and (x_d,y_d) are set to calculate the mean and standard deviation of a group of points associated with the parameter (θ,ρ). When the procedure described in Eq(6.29) is completed for each edge point in the image, the accumulator array $\mathrm{A}(\theta,\rho)$ is examined to find high peaks in counting. A high accumulated number in location (θ_0,ρ_0) corresponds to a large number of edge point satisfying Eq(6.30). Therefore, it is reasonable to assume that there exists a straight line associated with the parameter (θ_0,ρ_0). Several criteria were established and tested in this study for selection of the peaks in $\mathrm{A}(\theta,\rho)$ by simulating visual interpretation process as follow:

1. Lengths of linear features are significant both in absolute sense and in relative sense. The following condition:

$$(A(\theta,\rho) > n_0) \bigcup (A(\theta,\rho) / \sum_{\theta,\rho \in window} A(\theta,\rho) > r_0) \tag{6.32}$$

was used, where n_0 and r_0 are the thresholding values chosen experimentally. The value of n_0 is the absolute length while the value of r_0 is the relative length. The relative length concept can eliminate certain background noise in the peak selection, and

2. Because the procedure described in Eq(6.29) is carried out with the discrete digital image data, accuracy is limited. This can result in a situation where one linear feature represents several peaks in the parameter space. Only the highest peak is selected as the true one in this case. The following sorting procedure can be used in the selection:

$$\{ \quad A \quad (\theta,\rho) / \quad \theta \in \theta_0 \pm \Delta\theta, \rho \in \rho_0 \pm \Delta\rho \} \stackrel{\text{sorting}}{\Longrightarrow} \tag{6.33}$$

$$\{ \quad A \quad _i(\theta,\rho) / A_i(\theta,\rho) > A_{i+1}(\theta,\rho), i = 1,2,\cdots; \theta \in \theta_0 \pm \Delta\theta, \rho \in \rho_0 \pm \Delta\rho \} \; . \tag{6.34}$$

Thus, for a subset of $A(\theta,\rho)$, all elements are arranged in a sequence according to their counting numbers. The element with the highest counting number is chosen as the representative linear feature for the cluster.

After the orientation θ and the normal distance ρ for linear features are determined, the location of each linear feature has to be determined. The location of a linear feature can be estimated by using the mean and standard deviation of the coordinates of the edge points associated with (θ, ρ):

$$x_m = x_c/A(\theta,\rho) \tag{6.35}$$

$$y_m = y_c/A(\theta,\rho) \quad . \tag{6.36}$$

Under the assumption that edge points corresponding to the same linear feature observe a normal distribution, (x_m, y_m) can be used as the coordinates of the centre of the linear feature, which approximates the location of the linear feature.

With the same reasoning, the standard deviation (x_s, y_s) approximates the extension of the linear feature from (x_m, y_m)

$$x_s = \sqrt{x_m^2 - x_d/A(\theta,\rho)} \tag{6.37}$$

$$y_s = \sqrt{y_m^2 - y_d/A(\theta,\rho)} \quad . \tag{6.38}$$

c. Global linear feature connection

When the localized HT is carried out for all the windows in the image, the parameters estimated are converted into global ones:

$$\tilde{\rho} = \rho + x_0 \cos\theta + y_0 \sin\theta$$

$$\begin{aligned} \tilde{x}_m &= x_m + x_0 \\ \tilde{y}_m &= y_m + y_0 \end{aligned} \tag{6.39}$$

where the ˜ symbol denotes the definitions at the global level. Because the linear feature detection is performed within each window, cross window features are generally separated. Also, certain discontinuous linear features are often connected as a single continuous feature logically in a visual interpretation. Therefore a linear feature connection procedure is used to connect or extend linear features.

Let $l(\theta, \tilde{\rho}, N, \tilde{x}_m, \tilde{y}_m)$ represent the linear feature associated with parameter set $(\theta, \tilde{\rho}, N, \tilde{x}_m, \tilde{y}_m)$, where $N = A(\theta, \tilde{\rho})$. A group of collinear features $\mathrm{L}(\theta, \tilde{\rho})$ is defined as:

$$L(\theta, \tilde{\rho}) = \{l_1, l_2, \cdots, /\theta = \theta_0 \pm \Delta\theta, \tilde{\rho} = \rho_0 \pm \Delta\rho\} \quad . \tag{6.40}$$

For any two adjacent linear features l_i and l_{i+1}, the distance between their centres is defined as:

$$D_{i,i+1} = \sqrt{(\tilde{x}_{m,i} - \tilde{x}_{m,i+1})^2 + (\tilde{y}_{m,i} - \tilde{y}_{m,i+1})^2} \quad . \tag{6.41}$$

If $D_{i,i+1}$ is larger than a certain criterion, then l_i and l_{i+1} remain separated, otherwise they will be connected to form a new linear feature. When a connection takes place, the associated parameter set $(\theta, \tilde{\rho}, N, \tilde{x}_m, \tilde{y}_m)$ is also modified. This procedure continues until no more connection is needed.

The coordinates of the starting and the ending points for a linear feature can be estimated using the centre coordinates $(\tilde{x}_m, \tilde{y}_m)$ and orientation θ as below:

$$
\begin{aligned}
x_b &= \tilde{x}_m + Nh\sin(\theta) \\
y_b &= \tilde{y}_m + Nh\cos(\theta) \\
x_e &= \tilde{x}_m - Nh\sin(\theta) \\
y_e &= \tilde{y}_m + Nh\cos(\theta) \\
h &= \begin{cases} -0.5, & \theta > \pi/2 \\ +0.5, & \theta < \pi/2 \end{cases}
\end{aligned} \tag{6.42}
$$

where (x_b, y_b) is the ending point near the line $y = 0$ and (x_e, y_e) is another ending point of the same linear feature. A HT linear feature image can be generated using the coordinates in Eq(6.42).

Chapter 7

Results and Discussion

In the previous chapters, the data sets, their characteristics, and various techniques used to extract structural geological information from these data sets have been introduced. In this chapter, the interpretation of remote sensing images including the Landsat MSS, SPOT, and airborne C-SAR images will be presented. The results of automatic linear feature mapping and image integration will be discussed.

7.1 General Description

The best overall view of the study area is given by the Landsat MSS Bands 7, 5 and 4 color composite (Figure 7.1).

The color coding is Band 7=red, Band 5=green and Band 4=blue (a standard false color for the Landsat MSS image). The image has been rotated

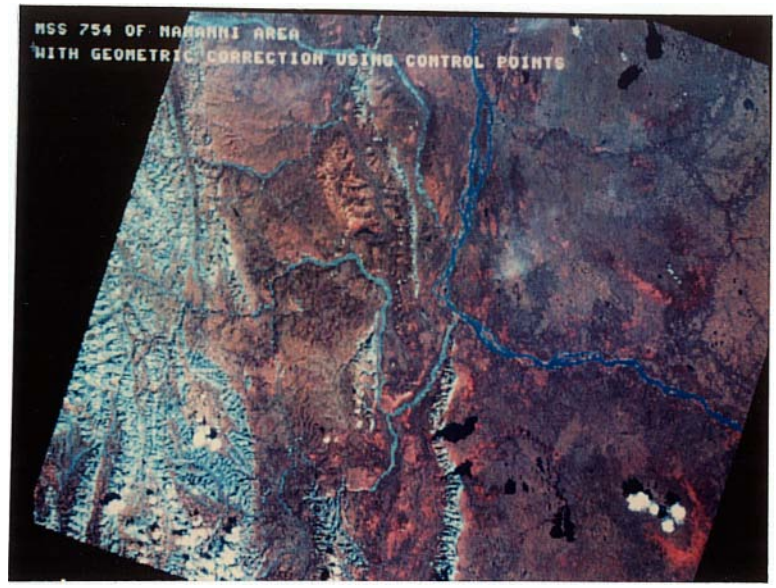

Figure 7.1: Landsat MSS image: Bands 7, 5 a.nd 4 color composite for the study area.

to the true north by using geometric correction. In general, most of the area in the image presents pink color, which may indicate poor vegetation. There are several deep-blue or near-dark areas which are lakes and strongly absorb the infrared band energy. There are also some clouds in the image, which are characterized by the combination of white clouds with their dark shadows. The rivers in the image are blue or gray-blue in color. They run mostly in the north-south or the east-west direction.

The whole image area can be divided into two parts by the north section of the Mackenzie River and the Nahanni Range. The eastern part is a portion of Great Slave Plain, where there is almost no significant topographic feature. In this part, the vegetation becomes more dense in the south than in the north. This reflects the latitude variation due to temperature and moisture gradient. In the western part, there are the Mackenzie Mountains and the Mackenzie Plain. The Mackenzie Mountain Ranges, which were still partially covered by snow at that time, can be seen at the bottom-left corner of the image.

A more detailed image of the epicentral area is given by the color composite of the SPOT Bands 1,2 and 3 (Figure 7.2). More variations in vegetation, soil and rocks can be seen.

Although the SPOT image of the study area was produced in 1989, the site of the rock avalanche triggered by the main shock of October, 1985 (Evans et al.,1987) can be easily identified.

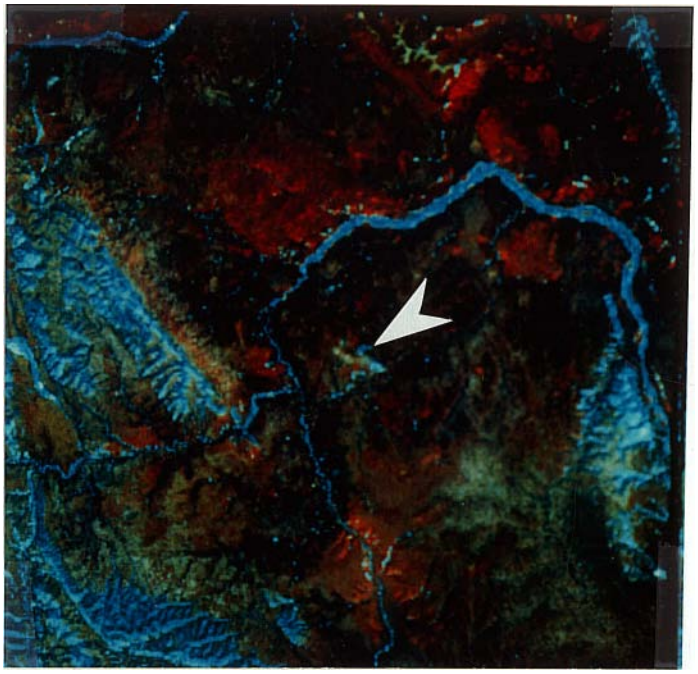

Figure 7.2: Color composite of SPOT images: Bands 1,2 and 3 for the study area. The arrow indicates the site of a rock avalanche triggered by the main shock of October, 1985.



Figure 7.3: PCA (Second component) linear feature image of the Landsat MSS data for the study area.

7.2 Structural Geological Interpretation

As discussed in (6.4.2), the second component of PCA was enhanced using spatial filtering. The filtering procedure includes E-W and N-S linear feature enhancement and sun azimuth effect compensation. The results were then combined to produce a linear feature image (Figure 7.3).

In this image, the tonal variations are suppressed and linear features are highlighted. In general, two major tectonic provinces can be observed: the

sedimentary platform and the fold belt. In the sedimentary platform, the structural expressions are very subtle. Only a few northwest-southeast features can be seen near the Nahanni Range. Some of them are possibly related to the strata dipping in south-west and west directions. While in the fold belt, there are many significant features in north-south or northwest-southeast direction. Some of them are clear indications of the known thrust faults in the area. In the south, the Nahanni Range is a major structure separating Great Slave Plain and Mackenzie Plain. The Range trending north-south is believed to consists of a large west-dipping thrust and expose some Ordovian to Upper Devonian sections (de Wet et al., 1973). The Mackenzie Plain, where the most earthquakes occurred, is relatively smooth and few significant features can be seen from this image. In the Mackenzie Mountains there is the most dense linear feature distribution in the image. The north or northwest trending features and many secondary features in other directions together form very complicated structural patterns. Figure 7.4 is a simplified linear feature interpretation of Figure 7.3.

In contrast with the smoothness of the epicentral area in the Landsat image, there are many linear features in the airborne C-SAR image. This difference is largely due to the very low depression angle α of 8.58° compared with the sun elevation angle of the SPOT or the Landsat MSS images (Table 5.2 and 5.4). Also the almost east-west radar illumination direction enhanced

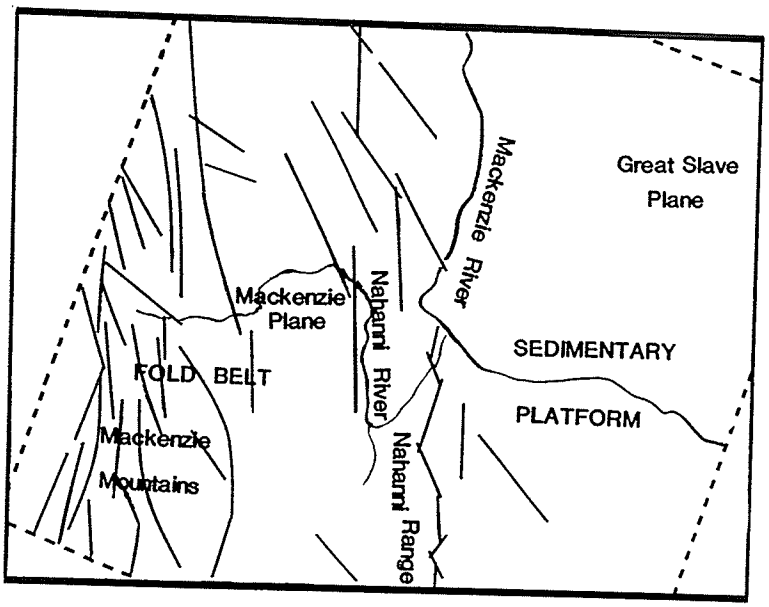

Figure 7.4: Interpreted linear features of the Landsat MSS image data in the study area.

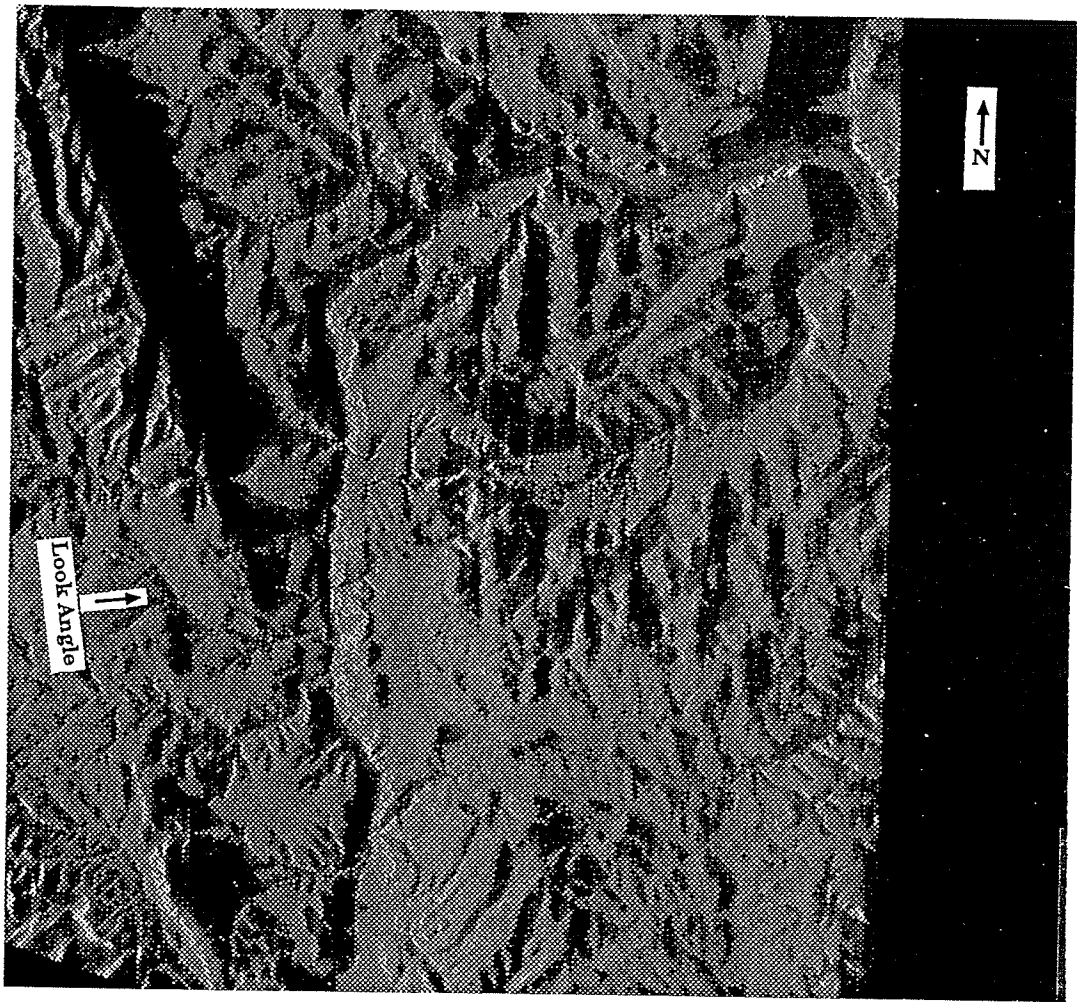

Figure 7.5: CCRS's airborne C-Band SAR image of the study area.

many north-south linear features. The most significant ones are the Iverson Thrust and some possible companion thrusts. Another interesting pattern of linear feature in this area is certain possible shear faults just in the central part of the epicentral area (Figure 7.5).

In one shear structure, one fault strikes N20°E and another strikes N20°W.

These are not likely the result of the compressive stress in this area (Adams, 1985), because the local horizontal compressive stress is N70°E which would make an angle of approximately 30° with each fault (Billings, 1972).

These structures are probably the shears of secondary order (Billings, 1972), which are a subsidiary set of strike-slip fault branches off the main strike-slip fault at an angle of approximately 30°. If this is the case, there should exist first order strike-slip faults in northeast-southwest direction in this area. In fact, Moon et al. (1991) have pointed out such possible first order faults when they interpreted remote sensing images in this area.

7.3 Remote Sensing Image Integration and Automatic Linear Feature Mapping

In this thesis, integration refers to a combination of different data sets or results of different processing methods to provide more interpretable images for analysis.

The Figure 7.6 is an image integration of the epicenter data set, the SPOT and airborne C-SAR image data sets. The color coding is red for the C Band of SAR, green and blue for the SPOT Bands 3 and 1, respectively. The white symbols indicate the earthquake epicenter distribution.

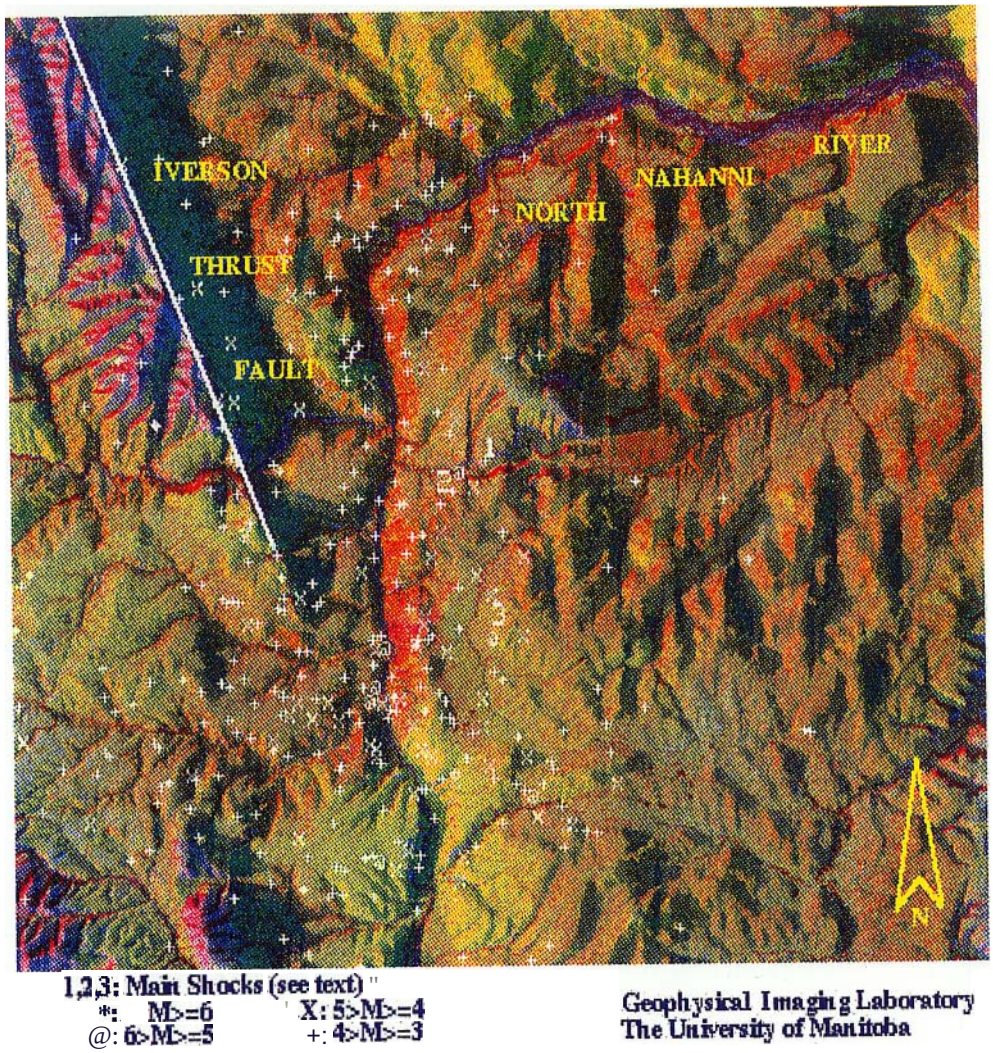

Figure 7.6: Integrated image of SPOT image (Bands 3 and 1), CCRS's C-SAR airborne data and local earthquake epicenter distribution information for the study area.

In the integrated image, the small depression angle of the airborne C-SAR data enhances linear features dramatically, whereas the SPOT image provides information in the shadow areas of airborne C-SAR data. It can be seen that most of the earthquake epicenters are located along the north-south section of the Nahanni River and disappear when the river turns to the east. This surface epicenter distribution pattern suggests that a north-south trending tectonic feature may have been interrupted by a major east-west trending geological structure between the Iverson Mountain Range and the Battlement Thrust Fault to the east of the area. The east-west trending segment of the North Nahanni River west of Iverson Range and the valley near by may represent another fault. This east-west structure extends beyond the image area and appears to continue to the Mackenzie River in the far east. It truncates the Nahanni Range, as well as the small mountain range just east of the Battlement Creek. The east-west trending structure is less predominant than either of the Iverson or Battlement Thrust Faults. It is not clear at this point that these east-west trending structures are the first order shears or not.

Automatic linear feature mapping described in (6.4.2) was applied to the Landsat MSS image. The resulting integrated image (Figure 7.7) consists of the linear features mapped by HT in the red channel, the edge image detected by convolution in the green channel and the second component of PCA from the Landsat MSS data sets in the blue channel.



Figure 7.7: Integrated image of computer picked linear features, edges and PCA second component image of the Landsat MSS data for the study area.

As expected, the most dense linear feature distribution appears at the bottom-left corner, in the Mackenzie Mountains. This linear feature cluster reflects the complex pattern of the fold belt. There are several major north-south or northwest-southeast trending features. One of these features is Iverson Thrust. Some of these features, which extend outside the image area, have a "Z" shape, this may indicate that they are caused by large scale shear forces. In the rest of the image, the linear feature distribution is less dense. However, compared with Figure 7.1, there are still several linear features along the Mackenzie River and on the Mackenzie Plain. These features are not randomly orientated but are mostly northwest-southeast trending. They may represent certain structural characteristics of Precambrian basement underneath.

An integrated image of detailed linear features in the epicentral area is shown in Figure 7.8. In this image, there are two groups of linear features: one trending approximately N40°E, the other trending approximately 0° or slightly northwest. Many of these linear features appear in a shear pattern. This coincides with the interpretation of the airborne C-SAR image. These three main shocks are near one of the intersections of mapped linear features. There is no east-west trending feature in the image.

In an attempt to compare the usefulness of different remote sensing data sets, an automatic linear feature mapping was used for both the SPOT data



Figure 7.8: Detailed integrated image of computer picked linear features, edges and PCA second component image of the Landsat MSS data of the epicentral area.

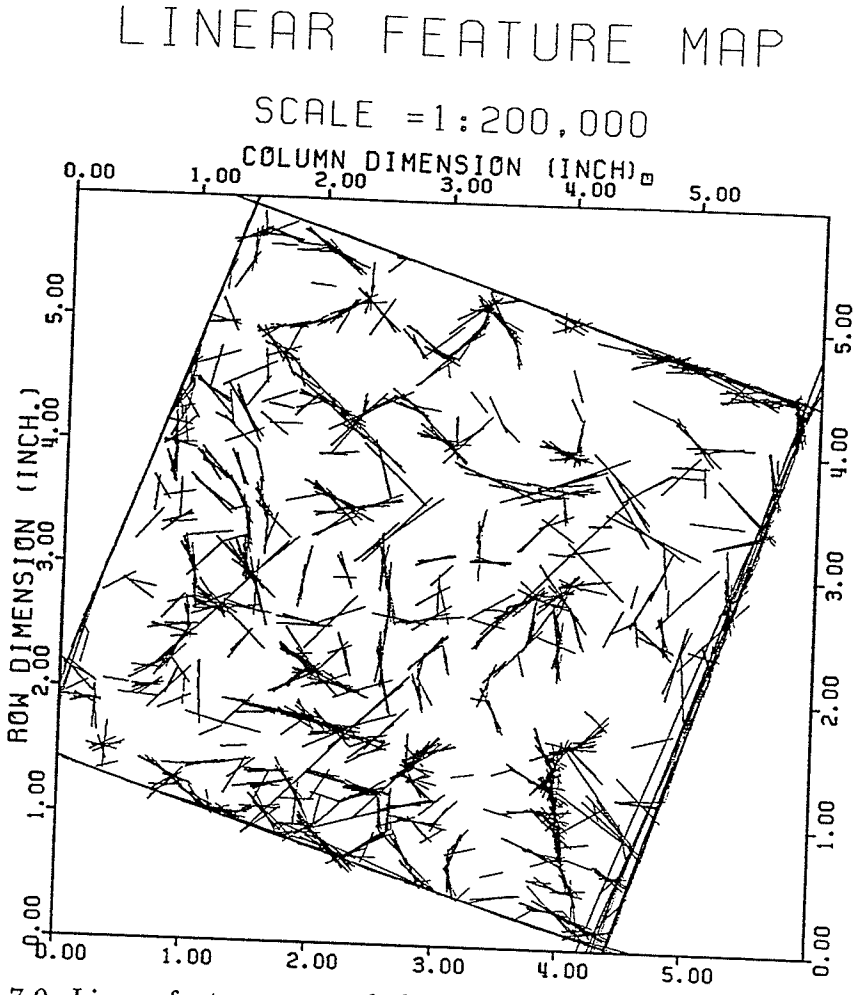

Figure 7.9: Linear features extended from the SPOT image for the epicentral area by using Hough Transform.

and the Landsat MSS data. However, when selecting the processing parameters, special consideration is taken so that new linear features which have not been found on the Landsat MSS image are emphasized. This is achieved by adjusting the kernel of convolution in filtering and changing the thresholds in generating the binary image.

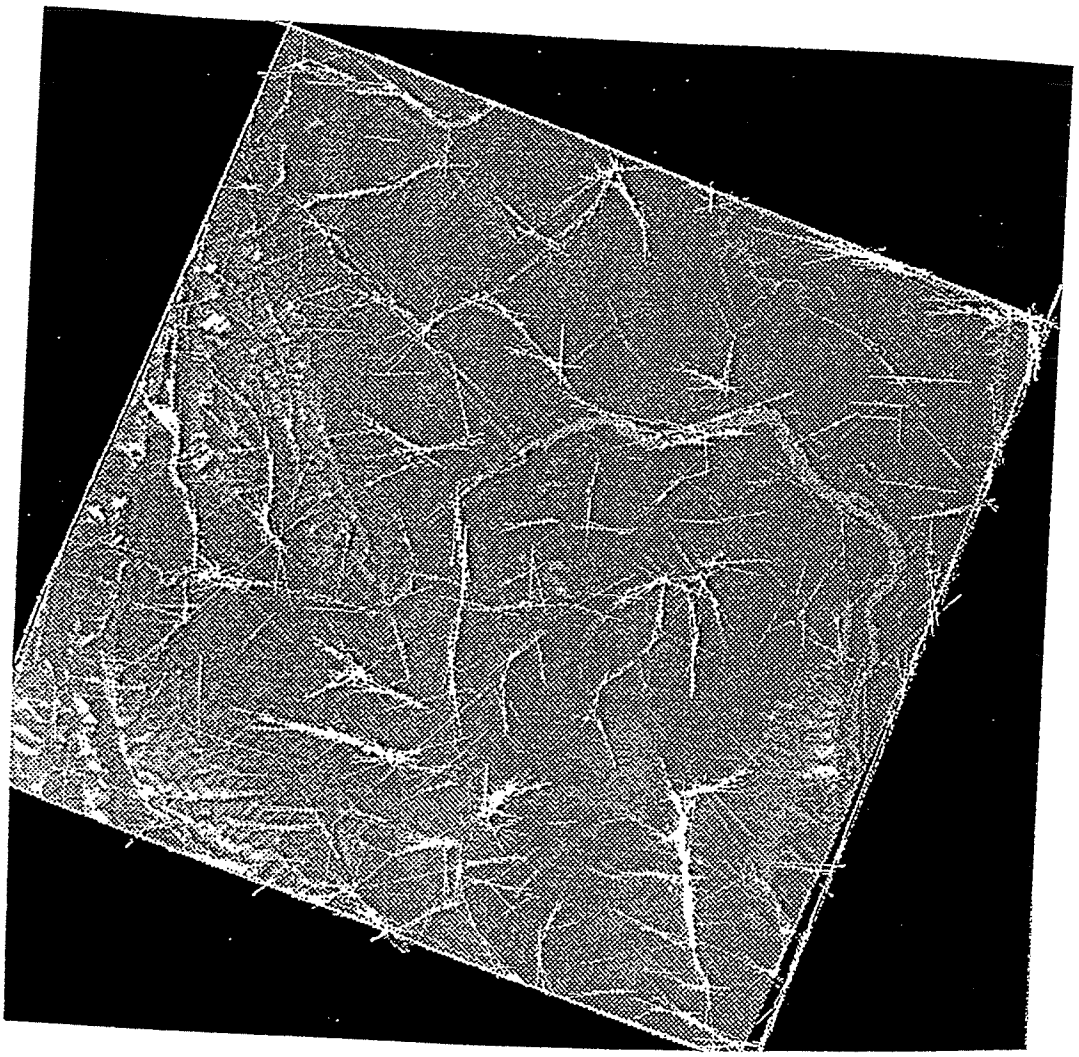

Figure 7.10: Integrated image of linear features and the Band 1 of the SPOT image data for the epicentral area.

In the automatic mapping processing for the SPOT image data, the image area is only approximately a quarter of the Landsat MSS image. Generally, the linear features mapped are less systematic in terms of their orientation. Many of them are also shorter in length. Certain significant features found in Figure 7.7, such as Iverson Thrust or Nahanni River are not seen or only partially seen in Figure 7.10. In the epicentral area, there are several northeast-southwest trending features which do not appear in Figure 7.8 at all. These features are close to the main shocks. The image also shows a curve feature south of the epicentral area. Other interesting features mapped include a few diamond-shaped features in the upper left corner, an ellipsoidal feature at left edge of the image and several curve-shaped features in the image. The differences of the mapping result between the Landsat MSS and SPOT data sets may be due to difference in spatial resolution, sun elevation angle and the range of band response. Because of much higher sun elevation in the SPOT image, many linear features are likely produced by variations in vegetation, soil moisture and rock types while for the Landsat MSS image, topographic relief is closely related to the mapped linear features.

7.4 Discussion

The remote sensing images with image enhancement provide an excellent opportunity to observe and analyze the surface structure in Nahanni earth-

quake area at several different scales. Many subsurface structures can also be detected or inferred using remote sensing techniques.

Generally, the multispectral images of the Landsat MSS and SPOT in the study area present considerable variations in surface geology. These variations are in forms of special structural patterns or in forms of different colors in composite images. One of the most noticeable variations is in Figure (7.1) along the Mackenzie River where the Upper Devonian rocks appear in a dark pink color whereas some of Middle Devonian and older rocks of the north-south trending ranges are in white or grey color. In Figure 7.2, it can be seen that three main shocks are all within a circular feature located to the east of the Nahanni River. Due to insufficient surface geological information, it is not clear whether this circular feature is an expression of some geological structure or variations in soil moisture and vegetation. Because of the large magnitude of these main shocks in Nahanni earthquakes, the local water table might be disturbed and in turn shows a certain pattern in soil moisture and vegetation.

On the enhanced images, the predominant linear features are northwest-southeast trending. Besides, there are several east-west trending features detected by HT and some shear patterns interpreted from the airborne C-SAR image. So far, researchers have pointed out the possible relationship between the northwest-southeast trending features and the faulting process in the Nahanni earthquakes (Wetmiller, 1988; Horner et al., 1990). However, the possi-

ble existence of east-west trending features is largely ignored. Actually, these east-west trending features can be surface expressions of a geological barrier which has affected the distribution pattern of a large number of aftershocks (Horner et al., 1990).

In Chapter 4, the focal plane solutions for the two main shocks and three aftershocks were discussed. According to the focal parameters and structural geological information available for the study area, one of focal planes was selected as the actual rupture plane, which is dipping west, for event 1,2, 4 and 5. However for event 3, one of its focal planes was found striking in the east-west direction. Now in view of several new linear features in east-west direction detected by the interpretation and HT mapping, the east-west striking rupture plane can not be excluded.

On the Figure 7.6, the three main shocks of October and December 1985, and March 1988 occurred in a strip 2 km long in the east-west direction, and 10 km wide in the north-south direction. The main rupture planes can not be clearly identified by surface breaks. However, the epicenter distribution, and the regional and local structural information all suggest that the ruptures most likely involved a series of west-dipping faulting. The rupture planes obtained using GDSN earthquake data are generally similar to those obtained using local seismic network data (Horner et al., 1990). However, there is considerable difference in dipping angle between the two focal solutions. The focal solutions

obtained in this study all have deep dipping angles. This can be one of the true characteristics of listric faulting. It can also be caused by uneven distribution geometry of the epicenters or errors in first movement determination in focal solutions. Both main shocks and aftershocks have a tendency to migrate southward. This implies that a certain north-south structure continues to act as a predominant force in the recent earthquake activities. So far all obtained focal planes of main shocks coincide more or less with the known local geological strike. However, if the southward migration tendency continues, the influence of newly found east-west structure may not be ignored.

If the selected rupture planes are extended until they intersect with the surface, the intersected fault lines will be close to the epicenters. We do find several suspicious linear features near the epicenters of main shocks. However, they are likely to be pre-existing structural features. Further investigation and possible field verification are needed to determine if these structural features have been involved in recent earthquake activities.

The result of this research also shows the potential of earthquake investigation using integrated remote sensing techniques. Each remote sensing data set has its own characteristics in spatial resolution, imaging geometry and spectral response. It is unlikely that one of the data sets alone can meet all the requirements for a specific task. In the remote sensing data sets available for this research, for example, the Landsat MSS data set provides a good view of

the tectonic frame in the study area, while the SPOT data set presents most of the variations on the surface. The airborne C-SAR data set gives us excellent details of surface structural features. For certain detected features, such as secondary shear patterns, there is no reasonable explanation unless more than one data set is analyzed.

Chapter 8

Conclusion

The approach of the earthquake investigation using integrated remote sensing techniques has proved to be very effective. Particularly, in the case of a remote area where access is restricted by logistical difficulty or a large study area is required.

With different spatial resolution, imaging geometry and spectral response, the Landsat MSS, SPOT and airborne C-SAR data sets provide comprehensive information sources, which allow us to extract and analyze structural features related to the Nahanni earthquake activities in various aspects.

The Landsat MSS image with its large coverage reveals the tectonic frame in the whole study area. This allows interpreters analyze the earthquake activities in a global manner. The SPOT image features higher spatial resolution, and stronger illumination due to a higher sun elevation angle, therefore more

surface variations are presented. This offers a possible way to detect any subtle tonal change which may be related to earthquake activities. The unique imaging geometry of the airborne C-SAR data set largely enhances topographic features. For this reason, it becomes probably the best data set for detailed structural interpretation in the epicentral area.

GDSN seismogram processing for the Nahanni earthquakes and focal plane solution are standard procedures in an earthquake investigation. However, use of Earth Model 1066B and WKBJ algorithm is very helpful to construct focal plane solutions when a global seismic network data set is utilized.

The combination of structural information from remote sensing data sets, focal plane parameters from GDSN data set, and other structural geological information suggests that the present earthquake activities in the Nahanni area are caused by a series of west dipping thrust faults. In the remote sensing images used in this thesis, several detected linear features coincide with the obtained rupture planes. There are certain east-west trending linear features and shear patterns detected using HT and by the interpretation of the airborne C-SAR image. These features present additional structural information for the earthquake area. By combining remote sensing data sets and earthquake seismic data set in this investigation, the uncertainty in the analysis has been reduced. However, many results of this study, such as the newly postulated faults and the related structural patterns, must be checked in the field, and

then verified through further analysis of the local geological and seismic data.

The image processing techniques applied in this study including geometric correction, enhancement and automatic linear feature mapping are successful. Proper geometric correction and co-registration allow us to use remote sensing data sets with different spatial resolution and imaging geometry in integration. Linear and non-linear enhancement and convolution filtering emphasize the target structural features, and PCA provides an approach to compress information in a multispectral image. HT application in remote sensing techniques is very helpful in an analysis where large data sets are involved. Furthermore, HT can simplify the complicated structural patterns in an image into a combination of some basic structural units such as linear, curve, circular and polygon features. Instead of being dependent upon the interpreter, the mapping criteria are defined logically and systematically in HT. Because such an automatic mapping mechanism works on its own logical inference, its mapping results are not limited by interpreters' thinking.

Appendix: The Computer Program for the Hough Transform

```
                    PROGRAM UMHT
C THIS PROGRAM IS WRITTEN FOR PICKING-UP LINEAMENTS FROM A
C SATELLITE GENERAL 2-D IMAGE  DATA FILE.
C
C ARRAY DESCRIPTION:
C IEG:CONTAINING THE X-Y COORDINATES OF NON-ZERO PIXELS IN
C     THE BINARY IMAGE;
C
C IPK:CONTAINING THE RESULTS OF HT TRANSFORM WITHIN A
C     SPECIFIC WINDOW;
C IPK(1): ANGLE THETA ASSOCIATED WITH THE LINEAMENT;
C IPK(2): GLOBE P     ASSOCIATED WITH THE LINEAMENT;
C IPK(3): TOTAL NUMBER OF PIXELS ASSOCIATED WITH THE
C         LINEAMENT;
```

```
C IPK(4): AVR. X COORDIANTE OF PIXELS ASSOCIATED WITH THE
C         LINEAMENT;
C IPK(5): AVR. Y COORDINATE OF PIXELS ASSOCIATED WITH THE
C         LINEAMENT;
C IPK(6): LINEAMENT LENGTH BASED ON IPK(3),IPK(1) AND STDV.
C         OF IPK(4) AND (5);
C WHICH TAKES ACCOUNT OF RASTER GRID EFFECT AND
C DISTRIBUTION OF PIXELS.
C
C LINTB : CONTAINING THE SAME CONTENTS AS IPK DOES
C         BUT FOR THE WHOLE IMAGE.
C
C GLINTB: CONTAINING THE FINAL RESULTS FOR LINEAMENT
C         MAPPING AFTER  MERGING  AND ELIMINATING
C         PROCESSING BASED LINTB.
C
C RS    : RS(I) INDICATES THE FIRST NON-ZERO PIXEL IN THE
C         Ith ROW IS THE
C         RS(I)th PIXEL IN IEG. THIS INFORMATION HELPS TO
C         LOCATE PIXELS
C         COORDINATES WITHIN A SPECIFIC WINDOW EASIER.
```

```
C
C IMGROW: BUFFER CONTAINS ONE ROW IMAGE DATA.
C

      INTEGER*4 RS(4000)
C
      INTEGER*2 IEG(358171,2),IPK(9000,6)
      INTEGER*2 LINTB(90000,7),GLINTB(90000,8)
C
      REAL SCF(180,2),PARAM(20)
C
      CHARACTER*70 PARINF(20)
C
C     IN THIS PROGRAM, AN IMAGE DATA WHICH WERE FIRST
C     CONVERTED IN TO BINARY
C     FORM ACCORDING TO THE INTERESTED INTERVAL CHOSED
C     WILL BE READ IN AS AN
C     INPUT. THIS INPUT IS DEFINED AS EDGE IMGAE. THE
C     EDGE IMAGE WILL  USED FOR HOUGH TRANSFORM.
C     >>>>>>>>>>>>>>>>>>>>>>>>>>>>>>>>>>>>>>>>>>>>>>>>
C     DEFINE PARAMETERS FOR INPUT IMAGE.
```

```
C
C ENTER ROWS,COLUMNE,EDGE POINT VALUE FOR THE IMAGE
      N=3808
      M=3802
C
      OPEN(UNIT=66,FILE='RUN.RCD',STATUS='UNKNOWN',
     +FORM='FORMATTED',RECL=80)
C
      WRITE(66,802) M,N
802   FORMAT(1X,' INPUT IMAGE = ',I5,' ROWS ',I5,' COLUMNS')
C ENTER X AND Y DIRECTION WINDOW SIZES AND OVERLAYS
      NSL=200
      MSL=200
      NVL=40
      MVL=40
C
C     MN: THE TOTAL IMAGE PIXELS
      MN=M*N
C
      PARINF(1)='MIN # OF PIXELS TO BE CONSIDERED IN WINDOW
     + HT SEARCH'
```

```
      PARINF(2)='RATIO OF PRACTICAL LINEAMENT LENGTH AND
     +CALCULATED ONE'
      PARINF(3)='% OF EDGE POINTS IN A WINDOW TO BE
     +CONSIDERED AS LINEA
     +MENT'
      PARINF(4)='LINEAMENT LENGTH MULTIFACTOR CONTROL BY
     +COORD. STDV'
      PARINF(5)='THETA DISTANCE IN LINEAMENT CONNECTION'
      PARINF(6)='P DISTANCE IN LINEAMENT CONNECTION'
      PARINF(7)='GAP BETWEEN END POINTS TO BE CONNECTED'
      PARINF(8)='THETA DISTANCE IN CLUSTERING'
      PARINF(9)='LINEAMENT CENTER X DISTANCE IN CLUSTERING'
      PARINF(10)='LINEAMENT CENTER Y DISTANCE IN CLUSTERING'
C
      PARAM(1)=20
      PARAM(2)=0.01
      PARAM(3)=0.02
      PARAM(4)=0.1
      PARAM(5)=3
      PARAM(6)=3
      PARAM(7)=3
```

```
      PARAM(8)=7
      PARAM(9)=15
      PARAM(10)=15
1     CONTINUE
C
C     READ IN THE EDGE IMAGE IN ROWS, THE IMAGE COORDINATES
C     WILL BE LIKE:
C
C           0--------------->X
C           |
C           |
C           |
C           |
C           |
C         Y V
C
C     READ EDGE PIXEL COORDINATES IEG AND AUX INFROMATION
C     ARRAY RS FROM DISK
C
      IEGWRT=22383
      IEGLFT=3
```

```
      IEGXY=16
C
      L1=1
      L2=IEGXY
      LDT=IEGXY
C
      OPEN(UNIT=30,FILE='IEGDATA',STATUS='OLD',
     +FORM='FORMATTED')
C
      OPEN(UNIT=40,FILE='RSDATA',STATUS='OLD',
     +FORM='FORMATTED')
C

C
      DO 100 I =1,IEGWRT
      READ(30,902) (IEG(I1,1),IEG(I1,2),I1=L1,L2)
C     WRITE(6,888) I
888   FORMAT(1X,'THE ',I9,' READ')
902   FORMAT(16(2I5))
      L1=L1+LDT
100   L2=L2+LDT
```

```
C
      READ(30,902)  (IEG(I1,1),IEG(I1,2),I1=L1,L1+IEGLFT-1)
C
      WRITE(6,889)
889   FORMAT(1X,' FINISH IEGDATA READ')
      READ(40,903) (RS(L3),L3=1,4000)
903   FORMAT(20I7)
      WRITE(6,890)
890   FORMAT(1X,' FINISH RSDATA READ')
C     NOW, BE PREPARED TO CONSTRUCTE HF 2D-HISTOGRAM
C
      CLOSE(30)
      CLOSE(40)
C
      DT=0.01745329
      IDRGL=180
      NNC=0
C
C     TO SAVE CALCULATION TIME, SET UP A SIN-COS FUNCTION
C     TABLE FOR
C     LOOK-UP
```

```
C
      DO 101 IS=1,IDRGL
      SCF(IS,1)=SIN(DT*IS)
101   SCF(IS,2)=COS(DT*IS)
C
C     DIVIDE THE WHOLE IMAGE INTO SMALL RECTANGULAR SUBIMAGES,
C     THEN WITHIN
C     EACH OF THEM, DO THE HT AND PICK UP THE PEAKS IN
C     HISTOGRAM(THETA,P),
C     GETHER THE PIXELS WITH EACH PEAKS AND SEND THEM FOR
C     SEGMENTATION AND'
C     SO ON THRU ALL THE SUBIMAGES ........
C
C
C
C     NSL=X-DIRECTION WINDOW SIZE
C     MSL=Y-DIRECTION WINDOW SIZE
C     NVL=X-DIRECTION WINDOW OVERLAY
C     MVL=Y-DIRECTION WINDOW OVERLAY
C
C      NSL=80
```

```
C       MSL=80
C       NVL=20
C       MVL=20
C
C      NGL=# OF X-DIRECTION SUBIMAGE DIVISION
C      MGL=# OF Y-DIRECTION SUBIMAGE DIVISION
C
       IF(((N-NSL)/(NSL-NVL))*(NSL-NVL).EQ.(N-NSL)) THEN
       NGL=(N-NSL)/(NSL-NVL)+1
       ELSE
       NGL=(N-NSL)/(NSL-NVL)+2
       ENDIF
C
       IF(((M-MSL)/(MSL-MVL))*(MSL-MVL).EQ.(M-MSL)) THEN
       MGL=(M-MSL)/(MSL-MVL)+1
       ELSE
       MGL=(M-MSL)/(MSL-MVL)+2
       ENDIF
C
C      IXUL,IYUL: THE UPPER-LEFT CORNER COORDINATES OF
C     THE SUBIMAGE
```

```
C     IXDR,IYDR: THE DOWN-RIGHT CORNER COORDINATES OF
C     THE SUBIMAGE
C
C      WRITE(6,441) NGL,MGL
441   FORMAT(1X,'TEST 441, NGL MGL= ',2I10)
C
      IYUL=1
      IYDR=MSL
C
C     LOOP THRU ALL THE SUBIMAGES
C
      NSD=NSL-NVL
      MSD=MSL-MVL
C
      DO 300 I=1,MGL
C
      IXUL=1
      IXDR=NSL
C
      DO 310 J=1,NGL
C
```

```
C     DO HT WITH THIS SUBIMAGE
C
C
C      WRITE(6,442)
442   FORMAT(1X', TEST 442')
      CALL ACU(IXUL,IYUL,IXDR,IYDR,IEG,RS,IPK,JD,
     +SCF,N,PARAM)
C
      IF(JD.EQ.0)GOTO 309
C
C     IF NO SIGNIFICANT LINEAMENT HAS BEEN FOUND IN THIS
C     WINDOW, JUMP TO
C     NEXT ONE....., OTHERWISE GETHER PIXELS WITH PEAKS
C     IN HT(THETA,P),
C     STORE THE RESULTS INTO LINTB
C
859   FORMAT(1X,' BEFOR ENTER WDSG, NNC,JD= ',I8,2X,I8)
      CALL WDSG(IPK,JD,LINTB,NNC)
212   CONTINUE
C
309   WRITE(66,851) I,J,NNC
```

```
 851   FORMAT(1X,'WINDOW(',I5,I5,') HAS BEEN FINISHED ',
      +'NNC=    ',I5/)
 308   IXUL=IXUL+NSD
       IXDR=IXDR+NSD
       IF(IXDR.GT.N) IXDR=N
 310   CONTINUE
 C
       IYUL=IYUL+MSD
       IYDR=IYDR+MSD
       IF(IYDR.GT.M) IYDR=M
 300   CONTINUE
 C
 C     LINK THE  LINEAMENTS THRU THE  WHOLE IMAGE
 C
       CALL GLK  (LINTB,JD,NNC,GLINTB,N,M,IGLN,PARAM)
 CC      CALL HBI(GLINTB,IGLN,SCF,M,N,LHEAD,HEAD,FORMA)
 C
 9998  WRITE(66,8888)
 8888  FORMAT(1X,' MAIN PROGAM ENDS')
       STOP
       END
```

```
C
C
C
CCCCCCCCCCCCCCCCCCCCCCCCCCCCCCCCCCCCCCCCCCCCCCCCCCCCCCCCCCCCCCCC
C
C
      SUBROUTINE ACU(IXUL,IYUL,IXDR,IYDR,IEG,RS,IPK,JD,
     +SCF,N,PARAM)
C
C PERMPRM HT WITHIN A SUBIMAGE
C
      INTEGER IXUL,IYUL,IXDR,IYDR,N
      REAL THIP(180,500,6)
      INTEGER*2 IEG(358171,2),XYD(4,2)
      INTEGER*2 IPK(9000,6)
      INTEGER*4 RS(4000)
      REAL SCF(180,2),PARAM(20)
C
C
C THIP(I,J,K)=
C K=1: # OF PIXELS FOUND
```

```
C K=2: SUM OF Y COORDINATE OF PIXELS
C K=3: SUM OF X COORDINATE OF PIXELS
C K=4: SUM OF SQUARE OF Y COORDINATE OF PIXELS
C K=5: SUM OF SQUARE OF X COORDINATE OF PIXELS
C K=6: THE LENGTH OF DETECTED LINEAMENT OBTAINING BY
C      MODIFYING
C THIP(I,J,1) USING THIP(I,J,2~5)
C
CC
C C     WRITE(6,443)
443   FORMAT(1X,' TEST 443')
      DO 500 I=1,180
      DO 501 J=1,500
      DO 499 K=1,6
499   THIP(I,J,K)=0
501   CONTINUE
500   CONTINUE
C
C
      DO 502 I=1,1000
      DO 503 J=1,6
```

```
503    IPK(I,J)=0
502    CONTINUE
C
       WRITE(66,801) IXUL,IYUL,IXDR,IYDR
801    FORMAT(1X,' XUL, YUL, XDR, YDR = ',4(I6,2X))
C
       XL=1
       XR=IXDR-IXUL+1
       YU=1
       YD=IYDR-IYUL+1
       IDRG=180
       IPRG=XR+SQRT(XR*XR+YD*YD)+2
       IC=0
       JD=0
       LMIN=PARAM(1)
C
C      LMIN=10
C
      TS1=PARAM(2)
      TS2=PARAM(3)
      TS3=PARAM(4)
```

```
C       TS1=0.2
C       TS2=0.1
C       TS3=0.0
C
C ADDING A CONSTANT TO AVOID NEGATIVE SUBSCRIPTS
C
C       WRITE(6,444)
444   FORMAT(1X,' TEST 444')
      IPAJ=IXDR-IXUL+10
C
C SEARCH EDGE PIXELS WITHIN THE SUBIMAGE BY ROWS
C TO FIND FIRST NON-ZERO RS(*) WITHIN Y-RANGE
C
C     IF  THERE IS NO EDGE PIXEL ON THE PRESENT LINE, JUMP
C     TO THE NEXT ONE
C
      IZ1=0
      IZ2=0
C
      DO 110 IY=IYUL,IYDR
      IF(RS(IY).EQ.0) GOTO 110
```

```
C      SEARCH FOR THE NEXT NON-ZERO EDFE POINT LINE
C
       IZ1=RS(IY)
       IY1=IY
       GOTO 100
110    CONTINUE
C
C IF ALL THE LINES HAVE NO EDGE POINT, THEN GET OUT THIS
C WINDOW
C
C
       GOTO 598
100    CONTINUE
C
C      WRITE(6,445)
445    FORMAT(1X,' TEST 445')
C      SEARCH FOR LAST NON-ZERO RS(*) BACKWARDS
C
       DO 111 IY=IYDR,IYUL,-1
       IF(RS(IY).EQ.0) GOTO 111
       IZ2=RS(IY)
```

```
        IY2=IY
        GOTO 99
 111    CONTINUE
 C
 99     CONTINUE
 C
 C MAKE SURE NOT LOSE ANY EDGE POINTS
 C
        IZ2=IZ2+N
 C
 C
 C   SEARCH FOR EDGE PIXELS ALONG THE LINE
 C   WITHIN X-DIRECTION BOUNDS
 C
 C
       DO 120 IZ=IZ1,IZ2
       IF(IEG(IZ,2).GE.IXUL.AND.IEG(IZ,2).LE.IXDR.AND.IEG(IZ,1)
      + .GE.IYUL.AND.IEG(IZ,1).LE.IYDR) GOTO 116
       GOTO 120
C
C   IC: THE COUNTS OF TOTAL NUMBER OF EDGE PIXELS WITHIN THE
```

```
C   SUBIMAGE
C
116       IC=IC+1
C
C   CALCULATE THETA-P HISTOGRAM FOR HT
C
       DO 130 IDG=1,IDRG
C
C MOVE THE ORIGIN TO THE (1,1) POSITION WITHIN EACH SUBIMAGE
C
844    FORMAT(1X,'IZ,IY1,IY2,ORIG. X, Y,IDG= ',6(I7,2X))
       X=IEG(IZ,2)-IXUL+1
       Y=IEG(IZ,1)-IYUL+1
842    FORMAT(1X,'IEG(IZ,2),IZ, IXUL= ',I10,2X,I10,I10)
C
       IP=Y*SCF(IDG,1)+X*SCF(IDG,2)+IPAJ+0.5
C       IF(IY.EQ.2.AND.IZ.EQ.71)
841    FORMAT(' P841, X,Y,SIN,COS,IDG,IP='/4(G9.3,2X),2(I8,2X)/)
       IF(IDG.GT.180.OR.IDG.LT.1.OR.IP.GT.620.OR.IP.LT.1) THEN
       WRITE(66,844) IZ,IY1,IY2,IEG(IZ,2),IEG(IZ,1),IDG
       WRITE(66,840) IDG,IP,SCF(IDG,1),SCF(IDG,2),X,Y
```

```
        ENDIF
        THIP(IDG,IP,1)=THIP(IDG,IP,1)+1
        THIP(IDG,IP,2)=THIP(IDG,IP,2)+IEG(IZ,1)
        THIP(IDG,IP,3)=THIP(IDG,IP,3)+IEG(IZ,2)
C
C IF THE IMAGE IS TOO LARGE (THOUSANDS BY THOUSANDS,SAY) THE
C FOLLOWING MAY OVERFLOW, THEN THIP CAN CHANGED INTO REAL TYPE.
C
        RIEG1=IEG(IZ,1)
        RIEG2=IEG(IZ,2)
C
        THIP(IDG,IP,4)=THIP(IDG,IP,4)+RIEG1**2
        THIP(IDG,IP,5)=THIP(IDG,IP,5)+RIEG2**2
C
130     CONTINUE
C
840     FORMAT(1X,' IDG=',I5,' IP= ',I5,' SIN,COS,X,Y=',4(G12.3,2X))
C
120     CONTINUE
C
C
```

```
C       WRITE(6,446)
446   FORMAT(1X,' TEST 446')
C     PICK UP THE PEAKS IN THETA-P HISTOGRAM
C     CRITERIA ARE THE RATIO OF ACTUAL LENGTH/THEORITICAL
C     LENGTH AND THE
C     NUMBER OF ACTUAL EDGE POINTS/THE TOTAL NUMBER OF EDGE
C     POINTS WITHIN
C     THE SUBIMAGE.
C
      XL=1
      YU=1
C
      DO 200 I=1,IDRG
      DO 210 J=1,IPRG
C
      ID=0
      IF(THIP(I,J,1).LE.LMIN.OR.THIP(I,J,1).LT.TS2*IC) GOTO 210
C       WRITE(6,843) I,J,THIP(I,J,1)
843   FORMAT(1X,' THIP(',I5,',',I5,')=',G12.4/)
C
C     CALCULATE THE COORDINATES OF INTERCEPTS WITH THE IMAGE
```

```
C     FRAME
C
C
C                  XU
C     |------------*------------|
C     |              *          |
C     |               *         |
C     |                *        |
C     |                 *       |
C     |                  *      |
C     |                   *     |
C     |                    *    |
C     |                     *   |
C     |                      *  |
C     |----------------------*-|
C                              XD
C

      IF(ABS(SCF(I,1)).LT.0.1) THEN
      THEOL=YD
      GOTO 209
```

```
      ENDIF
C
      IF(ABS(SCF(I,2)).LE.0.1) THEN
      THEOL=XR
      GOTO 209
      ENDIF
C
      YL=(J-IPAJ-XL*SCF(I,2))/SCF(I,1)
      YR=(J-IPAJ-XR*SCF(I,2))/SCF(I,1)
      XU=(J-IPAJ-YU*SCF(I,1))/SCF(I,2)
      XD=(J-IPAJ-YD*SCF(I,1))/SCF(I,2)
C
      IF(YL.GE.YU.AND.YL.LE.YD) THEN
      ID=ID+1
      XYD(ID,1)=XL
      XYD(ID,2)=YL
      ENDIF
C
      IF (YR.GE.YU.AND.YR.LE.YD) THEN
      ID=ID+1
      XYD(ID,1)=XR
```

```
      XYD(ID,2)=YR
      ENDIF
C
      IF(XU.GE.XL.AND.XU.LE.XR) THEN
      ID=ID+1
      XYD(ID,1)=XU
      XYD(ID,2)=YU
      ENDIF
C
      IF(XD.GE.XL.AND.XD.LE.XR) THEN
      ID=ID+1
      XYD(ID,1)=XD
      XYD(ID,2)=YD
      ENDIF
C
      THEOL=(XYD(1,1)-XYD(2,1))**2+(XYD(1,2)-XYD(2,2))**2
      THEOL=SQRT(THEOL)+0.1
C
209   CONTINUE
C
C     PICK UP PEAKS BY TWO CRITERIA
```

```
C
C OBTAIN TRUE LENGTH OF LINEAMENT BY CONSIDERING THE THETA
C BECAUSE THE SAME NUMBER OF POINTS REPRESENTS DIFFERENT LENGTH
C DEPENDING ON THE ANGLE THETA
C
      STDVX=THIP(I,J,5)/THIP(I,J,1)-(THIP(I,J,3)/THIP(I,J,1))**2
      STDVY=THIP(I,J,4)/THIP(I,J,1)-(THIP(I,J,2)/THIP(I,J,1))**2
      IF(STDVX.LE.0) THEN
      STDVX=0
      GOTO 269
      ENDIF
C
      IF(STDVY.LE.0) THEN
      STDVY=0
      GOTO 269
      ENDIF
C
269   STDVY=SQRT(STDVY)
      STDVX=SQRT(STDVX)
C
      IF(STDVX-STDVY) 211,211,212
```

```
C
211   LTRUE=THIP(I,J,1)/MAX(0.1,ABS(SCF(I,2)))
      FCL=STDVY
      GOTO 213
212   LTRUE=THIP(I,J,1)/MAX(0.1,SCF(I,1))
      FCL=STDVX
213   THIP(I,J,6)=LTRUE*(1+FCL*TS3)
C
      IF(THIP(I,J,6)/THEOL.GT.TS1) THEN
      JD=JD+1
      IPK(JD,1)=I
C
C TO CONVERT THE LOCAL P COORDINATE INTO GLOBE ONE
C
      IPK(JD,2)=(J-IPAJ)+(IXUL-1)*SCF(I,2)+(IYUL-1)*SCF(I,1)
C
C     NUMBER OF PIXEL COUNTS IN ONE PEAK
C
      IPK(JD,3)=THIP(I,J,1)
C      IPK(JD,4)=(XYD(1,1)+XYD(2,1))/2+IXUL
C      IPK(JD,5)=(XYD(1,2)+XYD(2,2))/2+IYUL
```

```
        IPK(JD,4)=THIP(I,J,3)/THIP(I,J,1)
        IPK(JD,5)=THIP(I,J,2)/THIP(I,J,1)
        IPK(JD,6)=THIP(I,J,6)
        ENDIF
C
210     CONTINUE
200     CONTINUE
C
598     WRITE(66,599) JD,IC
C       WRITE(6,810) ((IPK(I,J),J=1,6),I=1,JD)
810     FORMAT(1X,'IPK='/,6(I7,2X))
599     FORMAT(1X,'LEAVING ACU,# OF LINEAMENTS AND # OF EDGE
     +PIXELS',
     +I5,2X,I5)
852     FORMAT(1X,' I,IPK(I,*)= ',4(I5,2X))
853     FORMAT('  ACU RETURN')
        RETURN
        END
C
C
CCCCCCCCCCCCCCCCCCCCCCCCCCCCCCCCCCCCCCCCCCCCCCCCCCCCCCCCCCCCCCCCCCCCCCCCCCCCCCC
```

```
C
C
      SUBROUTINE WDSG(IPK,JD,LINTB,NNC)
C
C TO ADD THE RESULT OF SEGMENTATION OF ONE SPECIFIC STRIP WITHIN
C A WINDOW
C ONTO GLOBE SEGMENTATION TABLE FOR GLOBE LINKAGE LATER ON.
C
      INTEGER*2 IPK(9000,6)
      INTEGER*2 LINTB(90000,7)
C
C      WRITE(6,799) JD,NNC
799   FORMAT(' ENTER WDSG WITH JD,NNC=',I7,2X,I7)
      DO 100 I=1,JD
      DO 200 J=1,6
200   LINTB(NNC+I,J)=IPK(I,J)
C     WRITE(6,810) (IPK(I,J),J=1,6)
810   FORMAT(1X,'IPK='/,6(I7,2X))
100   CONTINUE
      NNC=NNC+JD
C
```

```
 800   FORMAT(1X,' FINISH WDSG WITH NNC=',I8/)
       RETURN
       END
C
CCCCCC
CCCCC
```

```
C     SEQUENCE
C
      DO 10 I=1,NNC-1
      DO 20 J=I+1,NNC
      IF(LINTB(I,6).LT.LINTB(J,6)) THEN
      DO 22 K=1,7
      ISAVE(K)=LINTB(I,K)
      LINTB(I,K)=LINTB(J,K)
      LINTB(J,K)=ISAVE(K)
22    CONTINUE
      ENDIF
20    CONTINUE
10    CONTINUE
C
C     PICK UP ONLY ONE PEAK IN ONE CLUSER IN THETA-P DOMAIN
C
      DD=PARAM(8)
      DX=PARAM(9)
      DY=PARAM(10)
C       DD=5
C       DX=10
```

```
C       DY=10
C
C PUT THE FIRST CLUSTER SEED
C
      DO 25 L=1,7
25    CLUST(1,L)=LINTB(1,L)
C
      L=1
C
      DO 30 I=2,NNC
      DO 40 J=1,L
      LINTB1=LINTB(I,1)
      LINTB4=LINTB(I,4)
      LINTB5=LINTB(I,5)
      IF(IABS(LINTB1-CLUST(J,1)).LT.DD.AND.
     +   IABS(LINTB4-CLUST(J,4)).LT.DX.AND.
     +   IABS(LINTB5-CLUST(J,5)).LT.DY)GOTO 30
40    CONTINUE
C
C IF LINEAR FEATURE IS DISTINGUISH FROM THE SEEDS EXISTING
C IT IS ADDED TO THE SEED LIST.
```

```
C
      L=L+1
      DO 42 K=1,7
42    CLUST(L,K)=LINTB(I,K)
C
30    CONTINUE
C
C REARRANGE THE THE CONTENTS IN LINTB, IT BECOMES SEEDS
C TABLE NOW.
C
      DO 50 I=1,L
      DO 52 J=1,7
52    LINTB(I,J)=CLUST(I,J)
50    CONTINUE
C
C      OPEN(UNIT=21,FILE='LINTB.DAT',STATUS='UNKNOWN',
C     +FORM='FORMATTED',ACCESS='SEQUENTIAL',
C     +RECORDTYPE='FIXED',RECL=80)
C
Crm GLINTB.VET     WRITE(21,800) ((LINTB(I,J),J=1,6),I=1,L)
800   FORMAT(1X,' DG= ',I4,' P= ',I5,' #= ',I4,' XC=',I5,'
```

```
     +YC=',I5,' LE=',I5/)
      WRITE(66,860) L
860   FORMAT(1X,' TOTAL NUMBER OF SEED = ',I8)
C
      NNC=L
C
      TD=PARAM(5)
      TP=PARAM(6)
      GAP=PARAM(7)
C       TD=2
C       TP=2
C       GAP=0
      IGLN=0
      TEST=0
C
C
      DO 100 II=1,NNC-1
      ID=0
C
C     DEPEND ON THE SLOPE OF THE STRIP, TO DETERMINE THE END
C     COORDINATES OF LINEAMENTS
```

```
      IF(LINTB(II,7).EQ.-1) GOTO 100
      ID=ID+1
      DO 201 K=1,6
201   DPLTB(ID,K)=LINTB(II,K)
C
      LINTB(II,7)=-1
C DEPEND ON THE SLOPE OF THE STRIP, DETERMINE THE END
C COORDINATES OF THE LINEAMANTS
C

810   FORMAT(1X,' II=',I8,'  JJ=',I8)
      DO 200 JJ=II+1,NNC
      LTBDS1=LINTB(II,1)-LINTB(JJ,1)
      LTBDS2=LINTB(II,2)-LINTB(JJ,2)
C
      IF(IABS(LTBDS1).LT.TD.AND.
     +IABS(LTBDS2).LT.TP) THEN
      ID=ID+1
      DO 202 K=1,7
202   DPLTB(ID,K)=LINTB(JJ,K)
      LINTB(JJ,7)=-1
```

```
        TEST=TEST+1
        ENDIF
 200    CONTINUE
 C
        IF(ID.EQ.0) GOTO 99
        IDU=DPLTB(1,1)
 C
        DT=0.01745392
        TSF=SIN(IDU*DT)*0.5
        TSF1=COS(IDU*DT)*0.5
 C
        IF(IDU.GT.90) THEN
        TSF=-TSF
        TSF1=-TSF1
        ENDIF
 C
 C
        IF(ID.EQ.1) THEN
        IGLN=IGLN+1
 C
       DO 300 L1=1,3
```

```
300   GLINTB(IGLN,L1)=DPLTB(1,L1)
C
      ID34=DPLTB(1,4)+TSF*DPLTB(1,6)
      GLINTB(IGLN,4)=MIN(MAX(1,ID34),N)
      ID35=DPLTB(1,5)-TSF1*DPLTB(1,6)
      GLINTB(IGLN,5)=MIN(MAX(1,ID35),M)
      ID36=DPLTB(1,4)-TSF*DPLTB(1,6)
      GLINTB(IGLN,6)=MIN(MAX(1,ID36),N)
      ID37=DPLTB(1,5)+TSF1*DPLTB(1,6)
      GLINTB(IGLN,7)=MIN(MAX(1,ID37),M)
      GOTO 100
      ENDIF
C
C
      DO 400 I=1,ID-1
      DO 410 J=I+1,ID
      XC1=DPLTB(I,4)
      XC2=DPLTB(J,4)
      YC1=DPLTB(I,5)
      YC2=DPLTB(J,5)
C
```

```
      IF(IABS(IDU-90).GT.0.5) GOTO 412
C
C     45 <THETA < 90
C
411   IF(XC1.GT.XC2) GOTO 419
      GOTO 410
C
C     THETA> 45 OR THETA > 135
C
412   IF(YC1.GT.YC2) GOTO 419
      GOTO 410
C
419   CONTINUE
      DO 420 K=1,7
      WORK(K)=DPLTB(I,K)
      DPLTB(I,K)=DPLTB(J,K)
420   DPLTB(J,K)=WORK(K)
C
410   CONTINUE
400   CONTINUE
C
```

```
      ID1=1
      XYE(ID1,1)=1
      XYE(ID1,2)=1
C
      DO 500 I=1,ID-1
      XE1=DPLTB(I,4)
      YE1=DPLTB(I,5)
C
      XE2=DPLTB(I+1,4)
      YE2=DPLTB(I+1,5)
      RUS=(DPLTB(I,6)+DPLTB(I+1,6))/2.0
C
      IF(SQRT((XE1-XE2)**2+(YE1-YE2)**2).LT.GAP*RUS) THEN
      XYE(ID1,2)=I+1
      GOTO 500
      ENDIF
C
      ID1=ID1+1
      XYE(ID1,1)=I+1
      XYE(ID1,2)=I+1
C
```

```
500   CONTINUE
C
      DO 700 I=1,ID1
      NN=0
      GP=0
      GD=0
      K1=XYE(I,1)
      K2=XYE(I,2)
C
      DO 710 J=K1,K2
      NN=NN+DPLTB(J,6)
      GP=GP+DPLTB(J,2)
710   GD=GD+DPLTB(J,1)
C
      IGLN=IGLN+1
      GLINTB(IGLN,3)=NN
      GLINTB(IGLN,1)=GD/(XYE(I,2)-XYE(I,1)+1)
      GLINTB(IGLN,2)=GP/(XYE(I,2)-XYE(I,1)+1)
      ID34=DPLTB(K1,4)+TSF*DPLTB(K1,6)
      GLINTB(IGLN,4)=MIN(MAX(1,ID34),N)
      ID35=DPLTB(K1,5)-TSF1*DPLTB(K1,6)
```

```
      GLINTB(IGLN,5)=MIN(MAX(1,ID35),M)
      ID36=DPLTB(K2,4)-TSF*DPLTB(K2,6)
      GLINTB(IGLN,6)=MIN(MAX(1,ID36),N)
      ID37=DPLTB(K2,5)+TSF1*DPLTB(K2,6)
      GLINTB(IGLN,7)=MIN(MAX(1,ID37),M)
C
700   CONTINUE
110   CONTINUE
100   CONTINUE
99    CONTINUE
C
C
C     OPEN(UNIT=25,FILE='GLINTB.DAT',STATUS='UNKNOWN',
C    +FORM='FORMATTED',ACCESS='SEQUENTIAL',
C    +RECORDTYPE='FIXED',RECL=80)
C     DO 750 I=1,IGLN
C     WRITE(25,890) I,GLINTB(I,1),GLINTB(I,2),GLINTB(I,3),
C    +GLINTB(I,4),GLINTB(I,5),GLINTB(I,6),GLINTB(I,7)
C750  CONTINUE
C
      OPEN(UNIT=26,FILE='GLINTB.VET',STATUS='UNKNOWN',
```

```
      +FORM='FORMATTED',ACCESS='SEQUENTIAL',
      +RECORDTYPE='FIXED',RECL=80)
C
C
C CHANE X-COORDINATES TO USE GRAPHIC PROCESSOR
C
      DO 751 I=1,IGLN
      WRITE(26,890) I,GLINTB(I,1),GLINTB(I,2),GLINTB(I,3),
     +MAX(1,N+1-GLINTB(I,4)),MAX(1,M+1-GLINTB(I,5)),
     + MAX(1,N+1-GLINTB(I,6)),MAX(1,M+1-GLINTB(I,7))
751   CONTINUE
C  MARK THE END OF VECTOR DATA AND
C RECORD PROCESSING PARAMETERS IN THE FILE.
C
      DO 752 I=1,8
752   GLINTB(IGLN+1,I)=-999
      WRITE(26,890) (GLINTB(IGLN+1,I),I=1,8)
C
      WRITE(26,891)
      WRITE(26,892) (PARAM(IP),IP=1,10)
C
```

```
891   FORMAT(1X,' THE PROCESSING PARAMETER USED '/)
892   FORMAT(1X,'I ',F4.0,'II ',F4.2,'III ',F5.3,'IV ',
     +F4.2,'V ',F4.1,'VI ',F4.1,'VII ',F4.1,'VIII ',F4.1,
     +'IX ',F4.1,'X ',F4.1/)
C
890   FORMAT(1X,'No.=',I5,' DG=',I5,' p=',I5,' #=',I5,' Xs=',I4,
     +' Ys=',I4,' Xe=',I4,' Ye=',I4)
C
C     CLOSE(25)
      CLOSE(26)
      WRITE(66,895) TEST,IGLN
895   FORMAT(1X,G12.5,' CONNECTIONS HAPPENDED and ','FINAL
     +LINEAR FEATURE NUMBER IS ',I5)
      RETURN
      END
CCCCCCCCCCCCCCCCCCCCCCCCCCCCCCCCCCCCCCCCCCCCCCCCCCCCCCCCCCCCCCCC
CCCCCCCCCCCCCCCCCCCCCCCCCCCCCCCCCCCCCCCCCCCCCCCCCCCCCCCCCCCCCCCC
      SUBROUTINE HBI(GLINTB,IGLN,SCF,M,N,LHEAD,HEAD,FORMA)
C
C THIS ROUTINE IS USED TO GENERATE A LINEAMENT MAP BASED
C ON HT.
```

```
C
      INTEGER*2 GLINTB(90000,8)
      REAL SCF(180,2)
      CHARACTER*80 HEAD(20)
C
C LOCAL
      INTEGER*2 LMAP(10,10)
      INTEGER*4 LCONEC(1000)
      REAL FORMA(10)
C
C
      DO 100 I=1,M
      DO 200 K=1,IGLN
      YMIN=GLINTB(K,5)
      YMAX=GLINTB(K,7)
      IF(YMIN.LE.I.AND.YMAX.GE.I) THEN
      IDG=GLINTB(K,1)
      DF=SCF(IDG,2)
      IF(ABS(DF).LE.0.07) DF=(DF/ABS(DF))*0.1
      IX=(GLINTB(K,2)-I*SCF(IDG,1))/DF
      IX=MIN0(N,MAX(1,IX))
```

```
      LMAP(I,IX)=1
C
      IF(LCONEC(K).EQ.0)THEN
      LCONEC(K)=IX
      GOTO 200
      ELSE
      IXL=AMIN0(IX,LCONEC(K))
      IXR=AMAX0(IX,LCONEC(K))
C      IXL=MAX0(1,IXL)
C
C
      IF(IXR-IXL.GT.30) WRITE(66,801)IXL,IXR,K
801   FORMAT(1X,' IXL,IXR,K= ',3(I5,3X))
      DO 210 J=IXL+1,IXR-1
210   LMAP(I,J)=1
      LCONEC(K)=IX
      ENDIF
C
      ENDIF
200   CONTINUE
100   CONTINUE
```

```
C
      WRITE(30,877) (HEAD(IA),IA=1,LHEAD)
877   FORMAT(A80)
C
      DO 300 I=1,M
      WRITE(28,FORMA) (255*LMAP(I,J),J=1,N)
300   CONTINUE
C
      CLOSE(30)
C
      RETURN
      END
```

Bibliography

[1] Abdel-Gawad, M., and Tubbesing, L., Analysis of tectonic features in U.S. southwest from SKYLAB photographs, *NASA CR-144464,* 1975.

[2] Adams, J., Canadian crustal stress data: a compilation to 1985, *Earth Phys. Branch Open-File Report 85-31* , 1985.

[3] Allen, C.R., Geological criteria for evaluating seismicity, *Geological Society of America Bulletin, 86,* 1041-1057, 1975.

[4] Billings, M.P., *Structural Geology,* third edition, Pretice-Hall, Inc., Englewood Cliffs, New Jersey, 1972.

[5] Billingsley, F.C., Data processing and reprocessing, Chapter XVII, *Manual of Remote Sensing (I),* American Society of Photogrammetry, Virginia, 1983.

[6] Canadian Oil and Gas Lands Administration, unpublished data, 1969.

[7] Castleman, K.E., *Digital Image Processing,* Prentice-Hall, Englewood Cliffs, N.J., 1979.

[8] Chapman, C.H., A new method for computing synthetic seismograms, *Geophysical Journal of Royal Astronomy Society, 54,* 481-518, 1978.

[9] Choy, C.L. and J. Boatwright, The rupture characteristics of 2 deep earthquakes inferred from broadband GDSN data, *Bulletin of the Seismological society of America, 71,* 691-711, 1981.

[10] Choy, C.L., and J. Boatwright, Teleseismic and near field analysis of the Nahanni earthquakes in Northwest Territories, Canada, *Bulletin of Seismological Society of America, 78,* 1627-1652, 1988.

[11] Cook, D.G., R.J.W. Douglas, H. Gabrielse and J.D. Aitken, Tectonics of the Mackenzie Fold Belt, Canada, *Geological Society of America Abstracts, 3,* 373-374, 1971.

[12] de Wet, R., E.C. Gronberg, W.B. Richards, and W.O. Richmond, Tathlina area, district of Mackenzie, *Future Petroleum Provinces of Canada* (Edited by McCrossan), Canadian Society of Petroleum Geologists, Calgary, 1973.

[13] Dey-Sarkar, S.K., and C.H. Chapman, A Simple method for the computation of body-wave seismograms, *Bulletin of the Seismological society of America, 68,* 1577-1593, 1978.

[14] Drury, S.A., *Image Interpretation in Geology,* Allen & Unwin, London, 1987.

[15] Duda, R.D., and P.E. Hart, Use of the Hough transform to detect lines and curves in pictures, *Communication of the Association of Computing Machinery, 15,* 11-15, 1972.

[16] Engdahl, E.R., J. Peterson and N.A. Orsini, Global Digital Networks current status and future directions, *Bulletin of the Seismological Society of America, 72,* S243-259, 1982.

[17] Evans, S.G., J.D. Aitken, R.J. Wetmiller and R.B. Horner, A rock avalanche triggered by the October 1985 Nahanni earthquake, District of Mackenzie, N.W.T., *Canadian Journal of Earth Science, 24,* 176-184, 1987.

[18] Freden, S.C., and F. Gordon, Jr., Chapter XII, *Manual of Remote Sensing (I),* American Society of Photogrammetry, Virginia, 1983.

[19] Gedney, L., and J. Van Wormer: Earthquakes and tectonic evolution in Alaska, Third ERTS-1 Symposium, *NASA SP-351, 1,* 745-756, 1974.

[20] Glass, C.E., and D.B. Slemmons, State-of-the-art for assessing earthquake hazards in the United States, Report II-Imagery in earthquake analysis, *U.S. Army Corps of Engineers Miscellaneous Paper S-73-1,* 32-41, 1978.

[21] Hall, E.L., *Computer Image Processing and Recognition,* Academic Press, New York, 1979.

[22] Herron, E.M., J.F. Dewey, and W.C. Pitman, Plate tectonic model for the evolution of the Arctic, *Geology, 2,* 377-380, 1974.

[23] Hobbs, W.H., Lineaments of the Atlantic boder region, *Geological Society of America Bulletin, 15,* 483-506, 1904.

[24] Hobbs, W.H., *Earth Features and Their Meaning: An Introduction to Geology for Student and General Reader,* Macmillan Publishing Co., N.Y., 1912.

[25] Hoppin, R.A., D.M. Andenson R.K. Stewart, D.L. Amsbury, Von R. Frierson, A.V. Mazade, and M.L. Miller, Geology and Hydrology, SKYLAB EREP investigations summary, *NASA SP-399,* 1978.

[26] Horner, R.B., R.J. Wetmiller, M. Lamontagne, and M. Ploffe, An fault model for the Nahanni earthquakes from aftershock studies, *Bulletin of Seismological Society of America, 80,* 1553-1570, 1990.

[27] Hough, P.V.C., A method and means for recognizing complex patterns, *U.S. Patent 3069654,* 1962.

[28] Illingworth J. and J. Kittler, A survey of the Hough Transform, *Computer Vision, Graphics and Image Processing, 44,* 87-116, 1988.

[29] Jensen, J.R., *Introductory Digital Image Processing: a remote sensing perspective,* Prentice-Hall, Englewood Cliffs, N.J., 1986.

[30] Kasahara K., *Earthquake mechanism,* Cambridge University Press, Cambridge, 1981.

[31] Leblanc, G., and R.J. Wetmiller, An evaluation of seismological data available for the Yukon Territory and Mackenzie Valley, *Canada Journal of Earth Science, 11,* 1435-1454, 1974.

[32] Lehn W.H., Lectures of the course of "Digital image processing and computer version", unpublished, 1991.

[33] Lowman, P.D. Jr., J.A. McDivitt, and E.H. White II, Terrain photography on the Gemini IV mission, preliminary report, *NASA Technical Note D-3982,* 1967.

[34] Lowman, P.D. Jr, Geological structures in California: three studies with Landsat-1 image, *California Geology, 29,* 75-81, 1976.

[35] McCauley, J.F., G.G. Schaber, G.S. Breed, M.J. Grolier, C.V. Haynes, B. Issawi, C. Elachi, and R. Blom, Subsurface valleys and geoarchaeology of eastern Sahara revealed by shuttle radar, *Science, 218,* 1004-1020, 1982.

[36] Moon, W.M., J.S. Won, B. Li, V. Roy Slaney, Maurice Lamontagne, Application of airborne C-SAR and SPOT image data to the geological setting of the Nahanni earthquake area, *Canadian Journal of Remote Sensing, 17,* 272-278, 1991.

[37] Moore, R.K., Imaging radar systems, Chapter X, *Manual of Remote Sensing (I),* American Society of Photogrammetry, Virginia, 1983.

[38] O'Leary, D.W., and S.L., Simpson, Remote sensor applications to tectonism and seismicity in the Northern part of the Mississippi embayment, *Geophysics, 42,* 542-549, 1977.

[39] Olson, N.K., Application of multispectral photography to mineral and land resources of South California, *NASA CR-144109,* 1975

[40] Peterson, J., H.M. Butler, L.G. Holcomb, and C.R. Hutt, The seismic research observatory, *Bulletin of the Seismological Society of America, 66,* 2049-2068, 1976.

[41] Peterson, J., and N.A. Orsini, Seismic Research Observatories: upgrading the worldwide seismic data network, *EOS, Transaction, AGU, 57,* 1976.

[42] Quade, J.G. and D.T. Trexler, Geological investigation in the basin and range of Nevada using SKYLAB/EREP data, *NASA CR-144497,* 1975.

[43] Reid, H.F., The elastic-rebound theory of earthquakes. University of California Publishing. *Geological Science, 6,* 413-444, 1911.

[44] Rogers, G.C., and R.M. Ellis, The eastern British Columbia earthquake of February 4, 1918, *Canadian Journal of Earth Science, 15,* 1484-1493, 1979.

[45] Sabins, F.F. Jr., *Remote sensing, Principles and Interpretation,* New York, W.H. Freeman and Company, 1987.

[46] Schalkoff, R.J., *Digital Image Processing and Computer vision,* New York, Wiley, 1989.

[47] Shuman, C.A., Remote sensing of fracture indicators near the Moodus, Connecticut seismic area, *IGARSS'89, I,* 108-111, 1989.

[48] Simonett, D.S., The development and principles of remote sensing, Chapter I, *Manual of Remote Sensing (I),* American Society of Photogrammetry, Virginia, 1983.

[49] Simonett, D.S., and R.E. Davis, Image analysis-active microwave, Chapter XXV, *Manual of Remote Sensing (I),* American Society of Photogrammetry, Virginia, 1983.

[50] Skingley, J. and A.J. Rye, The Hough transform applied to SAR image for thin line detection, *Pattern Recognition Letters, 6,* 61-67, 1987.

[51] Wang J. and P.J. Howarth, Edge following as graph searching and Hough transform algorithms for lineament detection, *IGARSS'89, I,* 93-96, 1989.

[52] Wetmiller, R.J., R.B. Horner, H.S. Hasegawa, R.G. North, M. Lamontagne, D.H. Weichert, and S.G. Evans, An analysis of the 1985 Nahanni earthquakes, *Bulletin of the Seismological Society of America, 78,* 590-616, 1988.

[53] Wheeler, J.O., and H. Gabrielse, The Cordillera structural province, Variations in Tectonic Styles in Canada (Edited by Price, R.A. and R.J. Douglas), Geological Association of Canada, *Special Paper 11,* 1972.

[54] Williams, R.S. Jr., Geological applications, Chapter XXXI, *Manual of Remote Sensing (II),* American Society of Photogrammetry, Virginia, 1983.